ISBN 978-82-326-4772-9 (printed version)
ISBN 978-82-326-4773-6 (electronic version)
ISSN 1503-8181

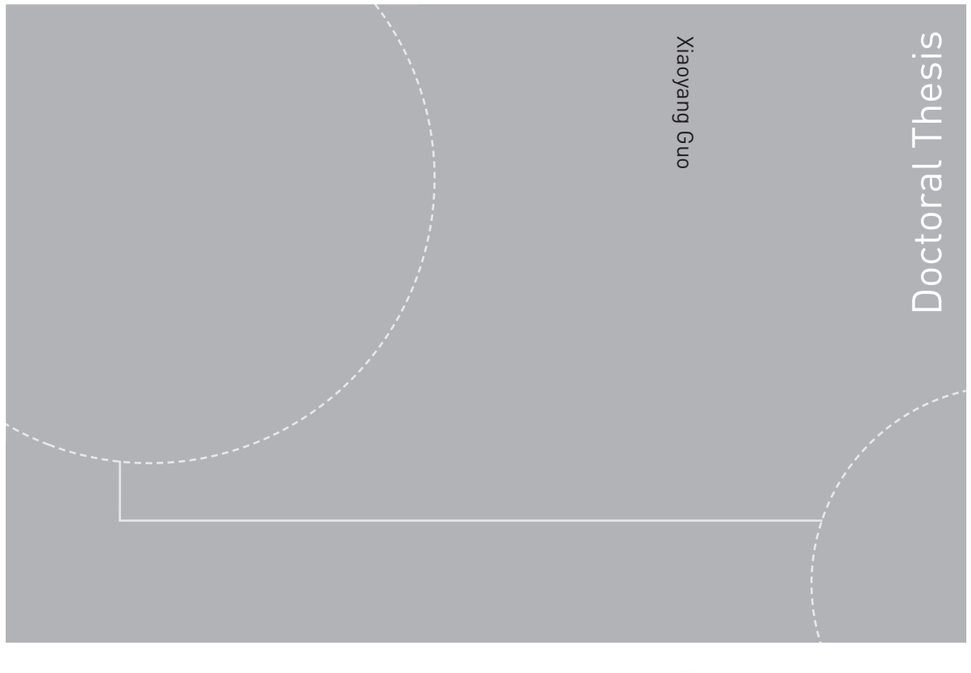

Doctoral theses at NTNU, 2020:212

Xiaoyang Guo

Inhibiting carbon growth at the initial stage of metal dusting corrosion of high temperature alloys

NTNU
Norwegian University of Science and Technology

NTNU
Norwegian University of
Science and Technology
Faculty of Natural Sciences
Department of Chemical Engineering

NTNU
Norwegian University of
Science and Technology

Doctoral theses at NTNU, 2020:212

NTNU

Xiaoyang Guo

Inhibiting carbon growth at the initial stage of metal dusting corrosion of high temperature alloys

Thesis for the degree of Philosophiae Doctor

Trondheim, June 2020

Norwegian University of Science and Technology
Faculty of Natural Sciences
Department of Chemical Engineering

NTNU
Norwegian University of
Science and Technology

NTNU
Norwegian University of Science and Technology

Thesis for the degree of Philosophiae Doctor

Faculty of Natural Sciences
Department of Chemical Engineering

ISBN 978-82-326-4772-9 (printed version)
ISBN 978-82-326-4773-6 (electronic version)
ISSN 1503-8181

Doctoral theses at NTNU, 2020:212

Printed by Skipnes Kommunikasjon as

Abstract

Metal dusting corrosion is a high temperature degradation phenomenon affecting Fe-, Ni- and Co- based alloys when exposed to strongly carburizing gases (carbon activity $a_c > 1$) at elevated temperatures (> 400˚C). The alloy disintegrates into a powdery mixture of metallic, carbidic, and carbonaceous dusts. The industrial process conditions cause transfer of carbon to the alloy surface by one or more of the CO reduction, Boudouard, and alkane thermal cracking reactions. For Fe-based alloys, metal dusting corrosion begins with the formation of Fe_3C or Fe_5C_2 carbides, the volume expansion creates defects on the alloy surface layer. Carbon atoms diffuse through the carbides and then precipitates as carbon at defects. Accumulation of carbonaceous deposits then separates the carbide particles from the metallic matrix that can be transported away from the surface of the alloy to leave a pit on the surface. For Ni-based alloys, metal-dusting corrosion proceeds without the formation of nickel carbides. Nickel carbides are unstable, so do not form under metal-dusting corrosion conditions. During exposure of Ni-based alloys to strongly carburizing conditions, metal-dusting corrosion occurs by direct graphite penetration into the metal phase.

All the Ni-based high temperature alloy (Inconel 601) and Fe-based high temperature alloy (Incoloy 800) samples studied in this thesis were polished down to 1 μm to give a mirror finish, some samples also underwent near surface severe plastic deformation (NS-SPD) followed by oxidation and/or exposure to metal dusting corrosion environment. Alloy coupons were subject to oxidation treatment at 540 ˚C in 10% steam in Ar at 1 bar for 6 hours. Steam oxidized samples were then exposed to different corrosion environments with either finite carbon activity (a_c>1) or infinite carbon activity (a_c>>1). Alloy coupons before and after carburizing gas treatment were unloaded and first analyzed by visual inspection, optical imaging, and light optical microscopy. The surface morphology and composition of the polished, pre-oxidized, and carburizing gas treated alloy coupons were studied by means of scanning electron microscopy (SEM) equipped with energy-dispersive X-ray spectroscopy (EDS) and Auger electron spectroscopy (AES) under ion-sputtering. The bulk composition of the two fresh polished alloy was determined by electron probe micro-analysis (EPMA) via wavelength dispersive X-ray spectroscopy (WDS). Corrosion products formed on the alloy coupon were characterized by transmission electron microscopy (TEM) equipped with EDS and electron energy loss spectroscopy (EELS). Cross-section TEM lamellas were prepared from selected alloy samples

by dual beam Focused ion beam (FIB)- SEM. The corrosion products and the underlying oxide layer on the alloy sample were analyzed by Raman spectroscopy.

In order to capture the initial carbon formation on the Ni-based high temperature alloy samples (Inconel 601), systematically pretreated alloy coupons were subjected to metal dusting conditions as a function of time, composition, and pressure at 750˚C. The carbon deposition on the alloy coupon is clearly a function of the gas composition during exposure, less carbon is formed under 10% CO in Ar with infinite carbon activity than under synthesis gas with finite low carbon activity, which points to the impact of the reaction mechanism and kinetics. The characterization indicates that the metal dusting corrosion rate is lowered when Cr_2O_3 rather than $(Ni, Fe, Cr)_3O_4$ spinel is the major phase of the oxide scale formed on the alloy coupons. Fine-grain structure on the alloy surface is also found beneficial to resistance the metal dusting corrosion.

Formation of carbon on the Incoloy 800 alloy surface of pre-oxidized samples was investigated by exposure to reducing, highly carburizing atmosphere (CO in Ar) at 20 bar and varying temperature (550-750 ˚C). Given that very high carbon activity $a_c >> 1$, the conditions represent an accelerated regime relative to the industrial environment, and significant amounts of carbon are formed. The amount and the type of carbon materials are found to vary strongly with the exposure temperature and the interaction with the metallic matrix. At the highest temperature i.e. 750 ˚C, also the alloy coupons undergo considerable change in the elemental distribution as a function of depth.

Finally, efforts have been devoted to inhibiting of metal dusting corrosion on Incoloy 800. Results show that Incoloy 800 samples treated by combined near surface severe plastic deformation (NS-SPD) and thermochemical treatment at elevated temperature exhibit no carbon formation, compared with the region not treated by NS-SPD on the sample. The good corrosion resistance performance is a result of the mechanical process produced an ultrafine-grained structure with a higher fraction of grain boundaries together with other microstructure defects near the surface. These microstructure defects increase the effective diffusion coefficient for Cr in the alloy, promoting the formation of a thin, protective Cr-rich oxide scale during the thermal treatment, which prevents contact between the carburizing atmosphere and the Ni and Fe contained in the bulk of alloy. The results imply that the metal dusting resistance performance of Incoloy 800 in industrial applications can be improved significantly by NS-SPD followed by thermochemical oxidative treatment.

Acknowledgements

This work could not have been possible without the support and encouragement of many people. First and foremost, I would like to give my deep gratitude to my supervisor, Professor Hilde J. Venvik, for giving me the opportunity to study here and all the supports through this project. Her invaluable guidance, optimistic attitude always encourages me. She gave me all kinds of support she could think of to help me throughout this project.

I also would like to thank my co-supervisors, Professor John Walmsley is sincerely thanked for his ideas, sample characterization assistance, and giving me the necessary training and guidance in Auger spectroscopy. Professor De Chen is greatly acknowledged for patient guidance and offering discussion anytime I needed. I am always inspired and motivated after discussion with him.

Beside my main supervisor and co-supervisors, I wish to thank the head of the Department of Chemical Engineering Professor Jens-Petter Andreassen for the Innovation scholarship as financial support at the late stage of my PhD project. Innovation manager Dr. Li He is greatly thanked for fruitful discussion, patient guidance during the patent application process. Senior Research Scientist and Associate Professor Per Erik Vullum is sincerely thanked for fruitful discussions, TEM sample preparation, and characterization. Dr. Estelle Vanhaecke is greatly acknowledged for fruitful discussions, who always give constructive suggestions about my research and manuscript preparation. Additionally, Dr. P.V. Daham S. Gunawardana is sincerely thanked for taking his time to answer my questions regarding metal dusting corrosion and helping me to start my experimental work, which is especially valuable for me at the beginning of my PhD study. Associate Professor Jia Yang is acknowledged for her kind help and fruitful discussion. Senior Engineer Dr. Yingda Yu is greatly acknowledged for teaching me SEM. I would like to thank senior engineer Trygve Lindahl Schanche and Berit Vinje Kramer for technical assistance at the micrographic laboratory.

I would express my gratitude to my friends working on similar topics in NTNU, Dr. Feng Qian, Shubo Wang, Dr. Di Wan and Dr. Yun Deng for much help on the experiments, and valuable discussion.

I am also thankful to Karin Wiggen Dragsten, Dr. Anne Hoff, Dr. Cristian Ledesma Rodriguez, Harry Trygve Brunn, Gunn Torill Wikdahl, Merethe Vadseth, Jan-Norten Roel and Erland

Strendo for their technical support, and to Department of Chemical Engineering (IKP) executive officer Lisbeth Roel and Tom Helmersen for their patience and efficient daily assistant from the administration office.

Many thanks to all members at Catalysis group for a nice working environment and the wonderful trips after conferences. Sharing an office with Shirley Liland has been a pleasure, a great friend, and a good teacher to Norwegian culture. I also want to say 'Thank you' to my friends Yanying Qi, Yahao Li, Xuehang Wang, Yalan Wang, Xiang Feng, Fengliu Lou, Wenyao Chen, Jianyu Ma, Zhongde Dai, Jing Deng, Bingxu Chen, Yuanwei Zhang, Stine Lervold, Marie Døvre Strømsheim, Mari Helene Farstad, Juntian Niu, Zhenping Cai, Junbo Yu and Hongfei Ma, the time here would not have been the same without you!

I would like to thank Stein, Cheng, Xin, Viggo, Junli, Chunbo, Torgeir, Horst, and Lillian for their great help and encouragement during my PhD study in Trondheim.

Moreover, my sincere appreciation goes to my former supervisor Professor Weilin Dai at Fudan University for teaching me the art of scientific research.

Financial support from the Research Council of Norway (NFR) under the GASSMAKS (Maximising Value Creation in the Natural Gas Chain) program is highly acknowledged.

The TEM work was carried out on NORTEM infrastructure, Grant 197405, TEM Gemini Centre, Norwegian University of Science and Technology (NTNU), Norway.

The Research Council of Norway is acknowledged for the support to the Norwegian Micro- and Nano-Fabrication Facility, NorFab, project number 245963/F50.

Finally, and most importantly, I would like to thank my wife Yinghong and my son Lucas, parents and parents in law for their immense support, understanding, and patience. I could not have come to this far without their love.

List of papers and presentations

Papers

This thesis is based on the following papers

I. **Xiaoyang Guo**; P.V.D.S. Gunawardana; De Chen; Estelle Vanhaecke; Hilde J. Venvik; John C. Walmsley. Investigation of Metal Dusting Corrosion Process over UNS N08800 Alloy *CORROSION 2017* (NACE international) ISBN: 9781510840348

II. **Xiaoyang Guo,** Estelle Vanhaecke, Per Erik Vullum, Jianyu Ma, P. V. D. S. Gunawardana, John C. Walmsley, De Chen, Hilde J. Venvik. Effects of metal dusting relevant exposures of alloy 601 surfaces on carbon formation and oxide development. *Catalysis Today*, Accepted.

III. **Xiaoyang Guo,** Estelle Vanhaecke, Per Erik Vullum, John C. Walmsley, De Chen, Hilde J. Venvik. Inhibition of Metal Dusting corrosion on Fe-based alloy by combined near surface severe plastic deformation and thermal treatment. In preparation

IV. Hilde J. Venvik, **Xiaoyang Guo**. Method for reducing metal-dusting corrosion. Patent application, Intellectual Property Office, United Kingdom, application number:1913256.2

Other contributions (Not a part of the PhD thesis)

I. Strømsheim, Marie Døvre; Knudsen, Jan; Farstad, Mari Helene; Sørvik, Linn Cecilie; **Guo, Xiaoyang**; Venvik, Hilde Johnsen; Borg, Anne. Near Ambient Pressure XPS Investigation of CO Oxidation Over Pd3Au(100). *Topics in catalysis* 2017;Volum 60.(17-18) s. 1439-1448

II. Strømsheim, Marie Døvre; Svenum, Ingeborg-Helene; Farstad, Mari Helene; Li, Zheshen; Gavrilovic, Ljubisa; **Guo, Xiaoyang**; Lervold, Stine; Borg, Anne; Venvik, Hilde Johnsen. Effects of K adsorption on the CO-induced restructuring of Co(11-20). *Catalysis Today* 2018; 299: 37-46.

Presentations of the research included to the thesis

I. **Guo, Xiaoyang**; Gunawardana, Daham; Chen, De; Vanhaecke, Estelle Marie M.; Venvik, Hilde Johnsen; Walmsley, John. Investigation of Metal Dusting Corrosion Process over UNS N08800 Alloy. CORROSION 2017; 2017-03-26 - 2017-03-30

II. **Guo, Xiaoyang**; Vanhaecke, Estelle Marie M.; Ma, Jianyu; Gunawardana, Daham; Walmsley, John; Chen, De; Venvik, Hilde Johnsen. *Investigation of initial stage of Metal Dusting Corrosion Process over Inconel 601.* EUROCORR2017 20th International Corrosion Congress & Process Safety Congress 2017; 2017-09-03 - 2017-09-07

III. **Guo, Xiaoyang**; Gunawardana, Daham; Vanhaecke, Estelle Marie M.; Chen, De; Venvik, Hilde Johnsen; Walmsley, John. *Characterization of metal dusting corrosion on instrumentation used in natural gas conversion technologies.* NNUM 2017 Nordic Nanolab User Meeting 2017; 2017-05-09 - 2017-05-10

IV. **Guo, Xiaoyang**; Gunawardana, Daham; Vanhaecke, Estelle Marie M.; Hwang, Jihye; Walmsley, John Charles; Chen, De; Venvik, Hilde Johnsen. *Material degradation by metal dusting corrosion on instrumentation used in natural gas conversion technologies*. NGCS 11 - 11th Natural Gas Conversion Symposium; 2016-06-05 - 2016-06-09

V. **Guo, Xiaoyang**; Vanhaecke, Estelle Marie M; Vullum, Per Erik; Walmsley, John; Chen, De; Venvik, Hilde Johnsen. *Investigation of initial stage of Metal Dusting Corrosion Process over Suppressed carbon formation on Fe-Ni based high temperature alloys by combined near surface severe plastic deformation and thermal treatment.* Norwegian Catalysis Symposium 2017 06 - 07 November Oslo Norway.

VI. **Guo, Xiaoyang**; Vanhaecke**,** Estelle Marie M; Vullum, Per Erik; Walmsley, John; Chen, De; Venvik, Hilde Johnsen. *Inhibition of Metal Dusting corrosion on Fe-based superalloy* Norwegian NanoSymposium 2019 16 - 17 October Trondheim Norway.

VI. **Venvik, Hilde Johnsen**; Guo**,** Xiaoyang; Vanhaecke**,** Estelle Marie M.; Vullum**,** Per Erik; Ma**,** Jianyu; Gunawardana**,** Daham; Walmsley**,** John. and Chen**,** De *The Initial Stage of Metal Dusting Corrosion of Inconel 601 – Effects of Exposure Conditions and Near-Surface Structure and Composition* NGCS 12 - 12th Natural Gas Conversion Symposium; 2019-06-02 - 2019-06-06

Other presentations with contributions from the candidate.

VII. **Strømsheim, Marie Døvre**; Knudsen, Jan; Guo, Xiaoyang; Sørvik, Linn Cecilie; Fernandes, Vasco Rafael; Venvik, Hilde Johnsen; Borg, Anne. *Near ambient pressure XPS investigation of CO oxidation over Pd3Au(100).* 17th Nordic Symposium on Catalysis (NSC17); 2016-06-14 - 2016-06-16

VI. **Farstad, Mari Helene**; Strømsheim, Marie Døvre; Knudsen, Jan; Guo, Xiaoyang; Gavrilovic, Ljubisa; Fernandes, Vasco Rafael P; Borg, Anne; Venvik, Hilde Johnsen. *CO oxidation over Pd-based alloys.* CMD26; 2016-09-04 - 2016-09-09

VII. **Medvedovski, Eugene**; Ma, Jianyu; Guo, Xiaoyang; Vanhaecke, Estelle Marie M.; Venvik, Hilde Johnsen. *Studies of Corrosion Resistance of Aluminized Coatings in Metal Dusting Environments.* Materials Science & Technology 2017; 2017-10-08 - 2017-10-12

Author's contribution

Paper I

The author carried out all experimental and characterization works except electron probe microanalysis. The article was prepared by the author with input from the supervisor and co-authors.

Paper II

The author has designed the experiments and carried out all characterization works except the FIB-assisted TEM Sample Preparation and TEM analysis of the sample, which was carried out by senior research scientist Per Erik Vullum in discussion with the author. The article was prepared by the author with input from the supervisor and co-authors.

Paper III

The author has designed the experiments and carried out all characterization works except the FIB-assisted TEM Sample Preparation and TEM analysis of the sample, which was carried out by senior research scientist Per Erik Vullum in discussion with the author. The article was prepared by the author with input from the supervisor and co-authors.

Paper IV

The author has designed the experiments and carried out all characterization works except the FIB-assisted TEM Sample Preparation and TEM analysis of the sample, which was carried out by senior research scientist Per Erik Vullum in discussion with the author. The article was prepared by the author with input from the supervisor and innovation manager of the department Dr. Li He.

List of symbols and abbreviations

Abbreviations

a_c	Carbon activity
AES	Anderson-Schulz-Flory
EDS	Energy dispersive X-ray spectroscopy
EELS	electron energy loss spectroscopy
EPMA	Electron probe micro-analysis
fcc	face centered cubic
FE-SEM	field emission gun scanning electron microscope
FIB	focused ion beam
FT	Fischer-Tropsch
FWHM	full width at half maximum
LAADF	Low-angle annular dark-field
NS-SPD	near surface severe plastic deformation
SEM	Scanning electron microscopy
STEM	Scanning transmission electron microscopy
T	Temperature
TEM	Transmission electron microscopy
WGS	Water-gas-shift
WDS	Wavelength dispersive X-ray spectroscopy
XRD	X-ray diffraction

Contents

1 Introduction

A short induction to metal dusting corrosion, the reason why it is important, and the precautions taken in the industry to avoid such corrosion are presented in this chapter, which ends with the scope of the work.

1.1. An introduction to metal dusting corrosion

In many industrial situations, such as petrochemical and refining processing, electric power generation and aerospace, metallurgical and chemical processing, high temperature alloys are used at temperatures ranging from ca. 400 ˚C to higher than 1100 ˚C. High temperature corrosion plays a critical role in alloy utilization in this temperature range. Metal dusting corrosion is one type of high temperature corrosion; degradation phenomenon that proceeds by a gradual breakdown of metals and alloys into a powdery mixture of graphite, carbide, and metal particles. Metal dusting corrosion occurs in carburizing atmospheres, containing CO and/or hydrocarbons with high carbon activities. Unwanted carbon is formed from the atmosphere and penetrates the metal phase leading to the growth of carbon materials which eventually destroys the alloy. Fe and Ni - main constituents of industrial alloys - are excellent catalysts for carbon formation. Alloys based on Fe and Ni are therefore susceptible to metal dusting corrosion. For Fe and Fe-based alloys, [1-3] metal dusting begins with the formation of Fe_3C or Fe_5C_2, and the volume expansion of carbides creates defects on the alloy surface.[4, 5] Carbon atoms diffuse through the carbides and then precipitate as carbon at the surface defects. Accumulation of carbonaceous deposits then separates the carbide particles from the metallic matrix that can be transported away from the alloy surface to leave a pit on the surface. For Ni and Ni-based alloys, [6, 7] they are destroyed by direct graphite penetration into the carbon oversaturated material since Ni carbides are unstable and cannot be identified at metal dusting conditions.

Metal dusting corrosion constitutes a major issue in the petrochemical industries, particularly in reforming units and cracker furnaces where metals and alloys are extensively exposed to carbon-saturated gaseous environments with low partial pressures of oxygen and/or steam in a critical temperature range of 400–900 °C [8-11].

In recent years micro-structured reactors have attracted increasing interest as useful devices for chemical reactions and processes due to radically enhanced heat and mass transfer in

combination with highly active, selective, and stable catalysts. Micro-structured reactors defined as reactors with characteristic dimensions in the micrometer range (1-1000 μm). The metal dusting corrosion issues are enhanced in the case of micro-structured reactors due to increased surface-to-volume ratio and irregularities in the surface structure and composition introduced by the structuring techniques and all the joints created upon sealing structured metallic rods, sheets, blocks *etc*[12].

Metal dusting corrosion carries a significant cost since considerable measures are implemented in order to avoid catastrophic events in the industrial operation characterized by poisonous and/or potentially explosive gases under high temperature and high pressure. Careful monitoring and periodic inspection as well as replacement of critical process units at intervals are required. Eventually, the extent of resistance to metal dusting depends on both process conditions and metallurgical factors. There are various precautionary techniques to control and minimize metal dusting and its consequences, each with their own limitations or involving compromise against other factors.

1.2. Processing of metals to inhibit metal dusting corrosion

Several aspects influence the selection of a metallic material for high temperature applications, including mechanical properties, materials conservation, corrosion resistance, cost effectiveness, and resistance to erosion. Increasingly demands imposed on materials make it more difficult or even impossible to combine the different properties required in one single material. Therefore, a composite system of a base material providing the necessary mechanical strength with a protective surface layer different in structure and/or chemical composition and supplied by a surface treatment can be an optimum choice in combining materials properties.[13] Near surface severe plastic deformation (NS-SPD) processes have been developed to introduce nanograins and grain size gradients into the surface region of metallic materials.[14] Such pre-treatment can form microstructures (including dislocations and grain refinement) in the near-surface region to help Cr to diffuse to the surface. This diffusion of Cr to the surface of the alloy promotes the formation of a Cr-rich spinel oxide film. Similar treatments are known to improve metal-dusting corrosion resistance but do not eliminate it. The continued presence of Fe and/or Ni on the surface results in the formation of an imperfect layer of Cr oxide. Carbon can diffuse through these imperfections into the bulk structure of the metal, resulting in metal dusting

corrosion. A dense and defect free oxide scale with the right composition (i.e. without Fe or Ni) is desired on the high temperature alloys to reduce metal dusting corrosion.

1.3. Scope of the thesis

This PhD project, titled "Metal dusting in micro-structured reactors" is conducted in the KinCat group at Norwegian University of Science and Technology (NTNU). The project has been carried out under close collaboration with SINTEF Industry. The project is a research activity in a national research program Maximizing Value Creation in the Natural Gas Chain (GASSMAKS) awarded by the Research Council of Norway to Department of Chemical Engineering, NTNU with SINTEF Industry as a research partner. The primary objective of the GASSMAKS program is to maximize value creation for society through the industrial processing of natural gas by enhancing knowledge development, promoting commercial development, and strengthening international competitiveness.

An overall motivation for this research has been to gain a better understanding of the initial stages of metal dusting corrosion process and enable prediction of carbon formation phenomena leading to metal dusting. In addition, identification of metal dusting issues that are particularly critical to compact reformers, and the enabling of alloy selection and alloy pretreatment procedures that minimize metal dusting corrosion in microreactors was targeted. With accumulated experience from a successfully completed PhD project of Dr. Daham Gunawardana[15] under the supervision of Professor Hilde J. Venvik and extensive literature investigations, I started to compare the performance of high-temperature alloys (Ni-based Inconel 601 and Fe-based Incoloy 800) under carburizing conditions to investigate the initial stages of metal dusting on these two alloys. Upon exposing Inconel 601 to two carburizing atmospheres the study revealed that the oxide developed during the exposure is crucial: the metal dusting corrosion rate being lowered due to Cr_2O_3 stabilization, while the $(Ni, Fe, Cr)_3O_4$ spinel represents an unstable redox state that yields continuous carbon formation. Also, a fine-grained alloy surface structure was found beneficial to the Cr_2O_3 formation. Incoloy 800 which is used to produce microreactors was also investigated by exposure to carburizing atmosphere. During the investigation, we noticed that the marker area on some alloy samples made by the tweezers (i.e. near surface severe plastic deformation region) had no carbon deposition, and there was also generally less carbon deposition than for the Inconel 601 after the corrosion test. This made us change the focus to more specific inhibition of metal dusting corrosion on the

studied alloy. Detailed investigation showed that the metal dusting corrosion of Incoloy 800 could be inhibited by combined near surface severe plastic deformation and thermochemical oxidative treatment.

In view of this development, the work presented in this thesis addresses the following research questions:

1. How the oxide layer at the interface between the carburizing gas and the high-temperature alloy develops at the initial stage of metal dusting corrosion?

2. How the characteristics of the deposited carbon are affected by the oxide layer during the initial stage of metal dusting corrosion?

3. In what ways can pretreatment methods make the high-temperature alloys inhibit metal dusting corrosion?

2 Theoretical background and literature review

Metal dusting corrosion is a catastrophic degradation phenomenon affecting Fe-, Ni- and Co-based alloys exposed to carburizing atmospheres at elevated temperatures. The deposition of unwanted carbon on and within these alloys is accompanied by the disintegration of the substrate. The carbon deposition impairs heat transfer efficiency and damages the structural materials as well as reduces the lifetime of catalysts used in the processing equipment. It is therefore important to analyze the thermodynamics of the relevant chemical reactions to determine the carbon formation potential. However, in the gas phase, carbon rarely forms even at high carbon formation potential because the reaction is affected by the interface conditions and catalysis. The formation of carbon deposits on the alloy surface is controlled by kinetics. Therefore, it is important to combine the thermodynamics with kinetic investigations to understand and predict the controlling parameters of the corrosion. A brief introduction of high temperature alloys, carbon formation chemistry, and metal dusting corrosion with a short literature review are presented in this chapter. Some of the precautionary techniques in the industry are also discussed.

2.1 High temperature alloys in metal dusting environments

High temperature alloy or superalloy is an alloy that has the following key features: good mechanical strength, good surface stability, resistance to thermal creep deformation, and resistance to corrosion or oxidation.[16] The crystal structure of the alloy is typically face-centered cubic (fcc) austenitic with a base alloying element of Ni, Fe, or Co. Examples of such alloys are Hastelloy, Incoloy, Inconel, Rene alloys, Waspaloy, TMS alloys, and CMSX single crystal alloys. High temperature alloys like Incoloy (~ $ 43000 USD/ton) and Inconel (~ $ 45500 USD/ton) series are much more expensive than stainless steel (~ $ 5000 USD/ton) and regular carbon steels (~ $ 1000 USD/ton).[17]

Inconel alloy 601 is a general-purpose austenitic alloy for applications that require resistance to heat and corrosion.[18] An outstanding characteristic of Inconel 601 is its resistance to progressive high temperature oxidation. Inconel 601 also has good resistance to aqueous corrosion, has high mechanical strength, and is readily formed, welded, and machined. The chemical composition of typical alloy samples determined by electron probe microanalysis (EPMA) via wavelength-dispersive X-ray spectroscopy (WDS) is given in Table 3.1. The

composition is a face centered cubic (fcc) solid solution with high degree of metallurgical stability. The alloy's nickel base, together with substantial chromium content, provides resistance to many high temperature environments and corrosive media. The oxidation resistance of Inconel 601 is further enhanced by the aluminum content.

In recent years, Ni-based Inconel 601 has attracted increased interest due to its resistance against corrosion under oxidizing and reducing conditions at high temperatures [7, 19-30]. Inconel 601 is thus widely used in petrochemical and other chemical process equipment. Klarstrom *et al*. have exposed Inconel 601 to a flowing gas mixture for 10,000 hours to investigate its metal dusting behavior [19]. Walmsley *et al*. have studied the basic features of carburization and carbide oxidation of Inconel 601 alloy in a commercial methanol plant exposed to metal dusting conditions for 2 years [27]. Nishiyama *et al*. have exposed alloy 601 to a synthesis gas together with their NSSMC 696 alloy for more than 10,000 hours to study the metal dusting resistance of the alloys [20]. Many of these studies have been based on the analysis of long-term exposed material (both in the laboratory and in the industrial plant), however, the kinetics of the initial carbon formation on the metal dusting relevant alloy surface is less understood and documented.

Since nickel was designated as a "strategic" metal, Incoloy alloy 800 was introduced to the market in the 1950s to fill the need for heat- and corrosion-resistant alloy with relatively low nickel content.[31] Incoloy alloy 800 is also a general-purpose alloy and is widely used material for the construction of equipment requiring heat resistance, corrosion resistance, strength, and stability. The alloy offers general corrosion resistance to many aqueous media and resists stress corrosion cracking. At elevated temperatures, it resists carburization, extended oxidation, and sulfidation. Fe-based Incoloy 800 containing 30-35% Ni, about 20% Cr and small amounts of Mn, C, Si, Al, Ti, and Cu is characterized as a ductile, fully austenitic structure. The iron in the alloy provides resistance to internal oxidation. The chromium imparts heat resistance and the nickel content maintains a ductile austenitic structure, making alloy 800 readily formed, machined, and welded. Incoloy 800 combines high strength with good resistance to oxidation, corrosion, and carburization in many aggressive industrial environments at elevated temperatures. Typical applications include steam reformer pigtails and headers, furnace components and equipment, petrochemical furnace cracker tubes, sheathing for electrical heating elements, and in nuclear energy technology, such as heat exchangers, pressure vessels and steam generator tubes [32].

It should be noted that Ni-based alloys generally show better metal dusting corrosion resistance compared to Fe-based alloys. There are several reasons for this difference: Cr atoms diffuse relatively fast and the amount of Cr increases with the Ni content of the alloys [33]. The carbon permeability is lower in Ni-based alloys compared to Fe-based alloys [2, 34-36]. Finally, fewer and larger metal particles are formed during the metal dusting process on Ni-based alloys compared to on Fe-based alloys, thereby lowering the total catalytic surface area for carbon formation [35, 37].

2.2 Carbon formation

The phenomenon of metal dusting has been studied for decades [2, 11, 30, 35, 38-41]. Metal dusting corrosion initiates as a result of unwanted carbon formation on the inner surface of equipment which exposed to carburizing atmospheres.

2.2.1 Thermodynamics and carbon activity

In metal dusting corrosion environments, the three main reactions by which carbon transfer from the gas atmosphere can happen, are the CO reduction*(0.1)*, Boudouard reaction*(0.2)*, and dissociation of hydrocarbons (*2.3*):

The CO reduction reaction:

$$CO_{(g)} + H_{2(g)} = C_{(s)} + H_2O_{(g)} \quad \Delta H^{\circ}_{298} = -131.3kJ/mol \qquad (0.1)$$

Boudouard reaction:

$$2CO_{(g)} = C_{(s)} + CO_{2(g)} \qquad \Delta H^{\circ}_{298} = -172.4kJ/mol \qquad (0.2)$$

Hydrocarbon dissociation:

$$C_nH_{2n+2(g)} = nC_{(s)} + (n+1)H_{2(g)} \quad \Delta H > 0 \qquad (0.3)$$

Both CO reduction *(0.1)* and Boudouard *(0.2)* reactions are exothermic reactions and are thermodynamically favored at low temperatures. Hydrocarbon dissociations are endothermic reactions and hence favored by high temperature. Methane or other hydrocarbon dissociation reactions are not studied in the Ph.D. project, and thus not discussed here in detail.

The driving force for metal dusting corrosion is usually evaluated in terms of thermodynamic parameter called carbon activity (a_c). Carbon activities for the above-mentioned CO reduction and Boudouard reaction can be defined as:

$$a_{c_1} = K_1(T) \cdot \left[\frac{P_{CO} P_{H_2}}{P_{H_2O}} \right] \tag{0.4}$$

and

$$a_{c_2} = K_2(T) \cdot \left[\frac{P_{CO}{}^2}{P_{CO_2}} \right] \tag{0.5}$$

Here p is the partial pressure for the given gaseous compounds and $K_i(T)$ is the equilibrium constant of the corresponding reactions. Thus, the potential of carbon formation in equations (0.4) and (0.5), i.e. carbon activity (a_c) is a function of both gas composition and temperature.

2.2.2. Kinetics and catalysis

Ni and Fe are among the important components of high temperature alloys, however, Ni, Fe, and their alloys are simultaneously excellent catalysts for producing carbon nanofibers (CNF) and carbon nanotubes (CNT) due to their ability to activate gaseous carbon-containing molecules to form carbon-carbon bonds. Carbon formation on Ni and Fe-based catalysts has been extensively studied, for example by Rostrup-Nielsen *et al.*[42, 43], Chen, Holmen *et al.*[44, 45] Andrews *et al.* [46]and Hata *et al.* [47]

The structure of the produced CNTs and CNFs was found to be dependent on the growth parameters such as reaction time, reaction gas, temperature, catalyst structure, catalyst size, and promoters. A number of theories have been postulated for CNF and CNT growth from the vapor phase with either root-growth[48, 49] or tip-growth[50, 51]. A schematic illustration of a widely-accepted growth mechanism for CNTs and CNFs is shown in Figure 2.1. When the catalyst particle has strong interaction with the substrate, the initial decomposition of carbon bearing gases takes place on the top surface of the catalyst particle, and as-dissolved carbon diffuses upward. Thus, CNTs and CNFs grow up with the catalyst particles rooted on its base. This is known as root-growth model. In the other case, when the catalyst-substrate interaction is weaker, the hydrocarbon on the top surface of catalyst particles decomposed and carbon diffuses down through/across the catalyst with CNTs or CNFs precipitates out across the bottom of the particle, pushing the whole catalyst particle off the substrate. This is known as tip-growth model. When

the catalyst particle is large, a combined root-tip-growth will result from the splitting of the large particles. The upper portion of the catalyst particle breaks away from the original catalyst and is lifted off along with the growing end of the CNTs or CNFs with the lower portion of the catalyst anchored to the substrate firmly.[46]

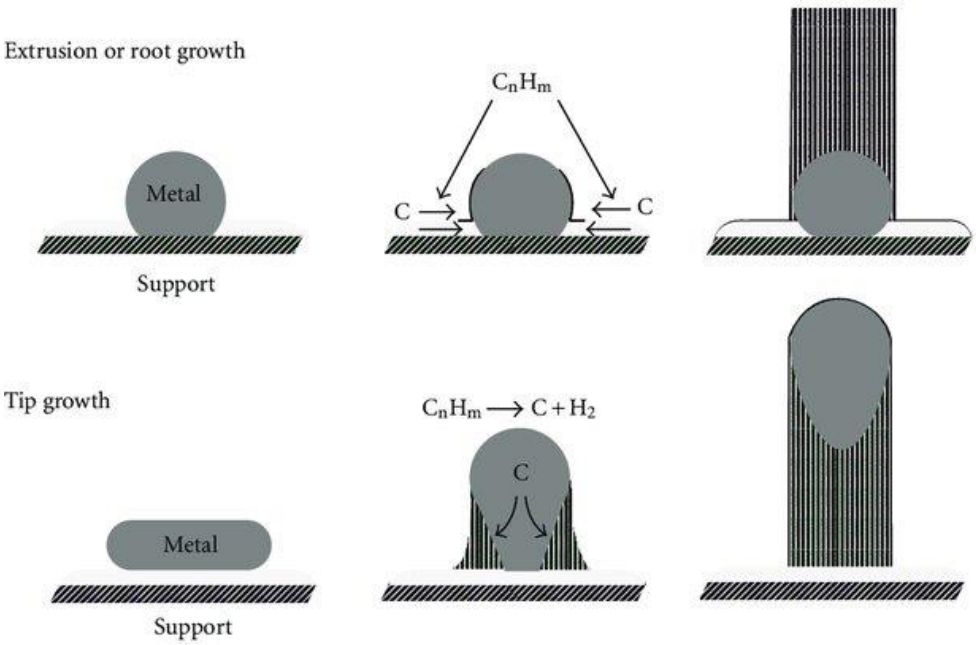

Figure 2.1: Schematic illustration of the widely-accepted growth mechanism for CNTs and CNFs.[52]

2.3 Review on recent advances in metal dusting corrosion

The phenomenon of metal dusting corrosion has been extensively reviewed[3, 6, 53, 54]. A comprehensive review of the thermodynamics, kinetics, and mechanism of metal dusting corrosion of different materials as well as the precautionary techniques used in the industry and their limitations was also presented in the thesis of P. V. Daham S. Gunawardana.[15] Recent experimental and theoretical investigations have widened the understanding of metal dusting corrosion significantly. This section in the thesis is intended as a mini review and summary of recent years' research results on metal dusting corrosion.

Metal dusting is not only commonly encountered in plants for petrochemicals production, natural gas processing [8], heat-treating, coal gasification [55], direct iron ore reduction, power generation, [56] but also exists in the solid oxide fuel cells [23, 57] gas turbines [58] and hydrogen

separation membranes [59]. The degradation mechanism of metal dusting corrosion depends on the material composition, temperature conditions, surface-subsurface microstructure as well as surface finishing. Several degradation mechanisms have been proposed by different researchers. It is generally accepted that Ni and Ni-based alloys are degraded by direct graphite penetration into carbon oversaturated material. [6, 60, 61] Zeng and Natesan proposed a corrosion mechanism of Ni and Ni-based alloys based on catalytic crystallization of carbon.[7, 62] Albertsen *et al.* also proposed a Ni-based alloy corrosion mechanism in their study of Inconel 693 and Nicrofer 602CA.[63-65] Szakalos *et al.*[41, 56, 66, 67], Chun *et al.*[25, 68], Pippel *et al.*[69, 70], and several other researchers also proposed different mechanisms/models for metal dusting corrosion based on their experimental evidences of various characterization techniques. The material degradation of Fe and Fe-based low-alloy steels via surface carbon formation, carbon diffusion, carbide formation, graphite formation, and subsequent carbide decomposition is proposed by Grabke.[6] High-alloy steels which contain high amounts of Cr are normally protected by Cr-oxide layer, however, the metal dusting of such materials are believed to be initiated at certain spots due to lack of uniformity and defects in the oxide layer. [4, 6, 63]

2.3.1 Mechanisms of metal dusting corrosion

Two new mechanisms on metal dusting corrosion were proposed recently. Monceau and co-workers exposed alloy 800HT to a 1 bar 47.25CO-47.25H_2-5.5H_2O atmosphere (a_c = 33) at 570 °C.[71] Pitting corrosion was observed and the pits showed a flattened morphology and a constant pit diameter growth rate. During the pit growth, corrosion rings appeared consecutively at the surface. The proposed pitting mechanism is based on internal oxidation of carbides and localized enhanced graphitization of the Cr-depleted alloy. It can be divided into 4 steps:

1) Pit nucleation and growth due to the breakdown of the oxide scale induced by the large volume expansion resulting from the oxidation of previously formed carbides. The localization of the attack is due to the presence of defects in the protective oxide scale.
2) Graphitization of the Cr-depleted matrix of the internal oxidation zone and the one that stemmed from the external oxide scale formation.
3) Enhanced graphitization due to a local atmosphere with lower oxygen and higher carbon activities at the bottom of a crack induced by tensile stress in the internal oxidation zone during cooling.

4) Lateral growth of pit is controlled by the kinetics of oxidation of the carbides whereas the pit inward growth is controlled by the enhanced graphitization at the bottom of the crack (whose merging results in an inner deep corrosion disk).

Marek Szkodo and Grzegorz Gajowiec have studied the mechanism of metal dusting of 10CrMo9-10 steel after10 years of operation in the semi-regenerative catalytic reformer [72]. Their study showed that the metal dusting mechanism of 10CrMo9-10 steel operated in the industrial environment differs from models developed in laboratories. Significant differences lie in the fact that the models developed in laboratories only assume the formation of metastable carbide M_3C, while studies have shown that the formation of M_3C carbides is associated with the transformation of primary carbides and in the next stage is preceded by the formation of the $M_{23}C_6$ carbides, which nucleate at M_3C carbides/metal matrix interfaces. Also, as a result of an increase of the carbon activity in the steel, $M_xC_{y'}$ alloyed carbides (mostly $M_{23}C_6$) precipitate in the first place which is not taken into account by theoretical models, however, at a later stage these carbides may convert to the metastable M_3C carbides due to prolonged operation of the steel at high temperature, low chromium content in the steel and a further increase of carbon activity in the steel. $M_xC_{y'}$ carbides precipitation process does not significantly affect the corrosion mechanism. However, the significant difference relative to the metal dusting mechanism models developed based on laboratory tests is the creation of a highly carburized layer of substantially greater thickness. It is very important for the operation of the equipment. Strong carburization of steel on large depth will result in a significant deterioration in its plastic properties and as a result, can contribute to a major accident due to brittle fracture of these elements.

2.3.2 Models for metal dusting corrosion

Apart from the models presented by Gunawardana in his thesis, [15] Monceau et. al. [73] also proposed a simple nucleation-growth model for metal dusting corrosion using incubation time t_0, nucleation of a number of circular pits N_0 and a constant lateral growth rate k_d. The main strength of this model resides in the limited information required to predict material degradation, mostly could be obtained via a surface analysis. Also, their modelling is suitable to be applied to the internal attack of industrial tubes.

Sheyla Herminia Camperos Guevara has presented a methodology to develop lifetime prediction models to evaluate materials performance under metal dusting corrosion conditions in her PhD thesis.[74] Two databases were created to integrate experimental results from their

project, as well as results from the literature to enable enough data for modeling. The databases allowed analyzing approximately 4000 corrosion rates by diverse statistical methods over different situations. She has applied the Principal Component Analysis (PCA) methodology to identify the key parameters to create lifetime prediction models using Multiple Linear Regressions (MLR). Two models were obtained to explain the kinetics of Pit Depth Growth and incubation times. The Pit Depth Growth model showed high correlations with the atmosphere composition and total pressure while the incubation times model showed high dependency on the alloy composition.

Yang Xiaobin and Mai Yiu-Wing have also studied the failure of high temperature alloys exposed to a carburizing gas atmosphere due to metal dusting corrosion. They developed a coupled model of the solid subjected to mechano-diffusional stresses. The *J*-integral (the energy release rate) for film spallation was determined for the interface crack between the protective film and the alloy substrate under applied diffusion stress. The effects of interface crack length, film thickness, and film mechanical properties on the *J*-integral for spallation were also investigated. The failure of high temperature alloys exposed to a carburizing gas atmosphere due to metal dusting corrosion was studied[75]. The coupled model of the solid subjected to mechano-diffusional stresses was developed, which coupled the elastic deformation with the diffusion stress of solutes and was used to model the elastic response of carbon diffusion into an alloy substrate in the process of metal dusting corrosion. For an interface crack between the protective film and the alloy substrate under an applied diffusion stress, the *J*-integral for film spallation was determined. The *J* values calculated by the authors were within the range of experimental critical *Jc* values of typical metal oxide coatings on metal alloy substrates. Hence, the methodology developed by the authors for evaluation of the *J*-integral for metal dusting corrosion could be adopted for quality and service integrity assurance of oxide coatings and/or protective films.

2.3.3 First-principles Investigation of metal dusting corrosion

Metal dusting corrosion as a macroscopic phenomenon has not received much attention in theoretical investigations like density functional theory (DFT) and molecular dynamics simulations. However, it has attracted attention from some research groups in recent years. El-Mellouhi et al. [76, 77]have conducted multiscale modeling of different iron system exposed to carbon-rich atmospheres by means of DFT and reactive molecular dynamics to evaluate the effects of gas content, temperature and surface defects such as emerging grain boundaries and

grooves on the CO dissociation rate directly related to metal dusting corrosion. Comparative DFT calculations demonstrate that C adsorption in the groove area is more favorable than on the clean surface. Molecular dynamical simulations of the CO dissociation rate variation in the presence of hydrogen on a Fe (111) surface using a ReaxFF potential shows direct analogy with the experimental observation of metal dusting rate as a function of temperature. The dual role of hydrogen as a reactant with dissociated carbon atoms and a CO dissociation enhancer was demonstrated quantitatively by analyzing of CO dissociation and recombination events on these systems. They provided a linear correspondence between CO dissociation variation as a function of temperature and the experimental measurement of metal dusting corrosion rate by carefully characterizing reaction mechanisms as a function of reactant content. They have demonstrated that stable surface vacancy clusters with large binding energies accelerate the adsorption of CO molecules by decreasing the corresponding dissociation energies. And they have also demonstrated that the appearance of multiple grain boundaries at the surface leads to an enhanced CO dissociation rate and the increase in surface roughness by emerging grain boundaries leads to an increase in CO dissociation rate.

2.3.4 Factors affecting metal dusting corrosion

Corrosion of metals by metal dusting can be affected by several factors, like the presence of steam[21], pressure[78], and alloying elements[79, 80]. A. Rouaix-Vande Put et al. exposed a series of chromia- and alumina-forming Fe- and Ni-base alloys for 500 h under metal dusting corrosion environments with varying temperature, total pressure, and gas composition.[21] They observed that the metal dusting attack was reduced when H_2O was added to a H_2–CO–CO_2 environment at 650 °C. The higher alloyed specimens retained a thin protective oxide, even after 5000 h at a total pressure of 9.1 atm with 20% H_2O. For gas mixtures with high a_c containing little or no H_2O, the Fe-based alloys were less resistant to metal dusting than Ni-based alloys.

Madloch and coworkers studied the effect of pressure on metal dusting initiation by exposing conventional alloys 800H and 600 in CO-rich syngas atmosphere at ambient and 18 bar total system pressure and 620 °C for 250 h.[78] Both alloy samples showed thin oxide scale formation and no sign of metal dusting when they are exposed at ambient pressure. However, samples showed severe mass loss by metal dusting attack when they are exposed to high pressure gases. Fe and Cr rich oxides and carbides were found as corrosion products. The pressure dependent behavior was discussed by considering both kinetic and thermodynamic aspects with respect to the protective oxide formation and pit initiation. It was verified that at constant temperature

both oxygen partial pressure and carbon activity increased simultaneously by increasing the total system pressure.

Hattendorf and coworkers[79] studied the influence of alloying elements on the metal dusting behavior of NiCr alloys and their statistical correlation. They have evaluated 16 high NiCr based alloys up to 5693 h for their metal dusting corrosion resistance. The differences between the samples in terms of incubation time to first pit, pit depth and mass loss were evaluated by statistical analysis and discussed in dependence of alloy composition. Only samples with combined Al plus Ni content of about 30 wt.% or more and a Fe content of 0.6 wt.% or less did not show any pit formation during the exposure time. In contrast, samples with a similar combined Cr plus Al content, but with a higher Fe content, showed pit formation due to metal dusting corrosion.

Fabas and co-workers studied several austenitic alloys at low and high pressure with the effects of Cr, Al, Cu, and Nb to metal dusting corrosion[80]. Alloy 625 showed good resistance to metal dusting corrosion, attributed to its Cr-rich composition resulting in a protective oxide scale formed on the surface. Selective oxidation of Cr resulting Cr depletion and leading to an Nb uphill diffusion and γ"–Ni_3Nb needles formed below the surface, which is beneficial for the resistance to metal dusting. α- Al_2O_3 formation was believed to induce cracks through the oxide scale, resulting in the alloy carburization. Al is thought to be detrimental in their studied conditions. They also studied the FeNiCrCu quaternary alloy, the good resistance to metal dusting corrosion is explained by its high Cu content, as Cu decreases carbon transfer and graphite nucleation rates. The beneficial influence of Cu might be enhanced by its precipitation at the alloy-oxide interface.

2.3.5 Corrosion products from metal dusting

The corrosion products from metal dusting environments have attracted several researchers' attention. Steyer and coworkers[81] investigated the origin of Ni catalytic particles in carbon nanotube formation on a high-carbon 25Cr-35Ni-Nb cast alloy. They employed TEM/EDS to reveal the presence of Fe-containing Ni_3C-based catalytic particles at the tip of the nanotubes, and then investigated the origin of the nickel in the system via cross-sectional observations. A mechanism similar to the so-called "ex-solution" process (ex-solution based on in situ growth of metal nanoparticles from the parent perovskite, the catalytically active transition metals, like Pt, Pd, Ru, Co, and Ni, are incorporated on the B site of perovskite oxide ABO_3 during material synthesis and then the transition metals are exsolved from the perovskite backbone as highly

dispersed nanoparticles under a reducing atmosphere.) was proposed to explain the presence of catalytic particles, while their stability was attested by thermodynamic considerations.

Meunier and coworkers[82] used the metal dusting process as a facile technique for growing carbon nanofiber directly on Ni-foam without any additional catalyst. Etching of the Ni-foam by an acid solution mixture was found to be essential for a good growth of CNF covering entirely the internal surfaces of the foam. They believe that the etching creates more nano growth sites that are uniformly distributed and lead to the formation of a dense and complete coverage of the CNF layer. The diameter of these CNF was about 78 ± 32 nm and could be tuned to a wider diameter up to 376 ± 35 nm by increasing the growth temperature.

2.3.6 Metal dusting corrosion in various applications

Several researchers have investigated metal dusting corrosion in recent years. In the thermal cycling of sodium system, Rajendran Pillai has studied and analyzed the possibility of metal dusting. [83] Under thermal cycling conditions, carbon may precipitate as sodium acetylide with a carbon activity higher than unity as the temperature is lowered. The high carbon activity promotes the formation of Fe_3C in ferrous alloys, metal dusting corrosion happens when this carbide decomposes.

Yang and coworkers have exposed pure Fe, Co-based alloys and Fe-Cr model alloys with different fractions (20-80 wt.%) of Cr to a microwave activated CH_4-H_2 plasma during the chemical vapor deposition (CVD) of diamond film.[84, 85] Pure Fe and Co-10Al alloy were severely carburized and resulting voluminous graphite formed before diamond deposition. Severe internal carburization of pure Fe leads to a metastable Fe_3C layer formed and then decomposed, resulting in the graphite precipitation. Also, graphitization occurs on Co-10Al alloy, the graphite is precipitated from $AlCo_3C$ as substrate carburization occurs. However, such a graphite interlayer is inhibited when the substrate carburization is hindered on high Al alloys (Fe-25Al and Co-30Al), attributed to the protection of an alumina-rich layer on the alloy surface. Severe carburization and metal dusting are observed on the low-Cr alloys (≤50%), and voluminous graphitic carbon deposits are formed on their surfaces, along with low density diamonds nucleating on the graphite layer. Increasing the Cr concentrations in the Fe-Cr alloys to 80% suppresses the carburization of the iron and the formation of graphite interlayer. Consequently, the nucleation and growth of diamond on the Fe–80Cr substrate are greatly enhanced.

Juliusz and co workers[86] have conducted the failure analysis of 501 AISI furnace tubes placed before the distillation column in refinery fractional distillation units. After two years exploitation, the investigated furnace tubes have less than 30% of the material left. The corrosion process had an intense and complex character. The well-adhered shiny black deposits and round, deep pits were present after two years of exploitation. The too high allowable operating temperature was identified as the main cause of such intense corrosion. Their study shows that exceeding temperatures over 450 °C can lead to very high corrosion risk.

L'vov and coworkers[87] have studied the effect of surface topography defects on the formation of carbon nanotube layers on bulk nickel. They found that the locally accelerated deposition of carbon layers with a highly disordered structure, which occurs at the initial stages of the process is the underlying cause of nonuniformity in carbon nanotube layers synthesized directly onto a metal surface. They have observed enhanced deposition rates at surface topography defects, including microcavities with a large surface to volume ratio. The cause of the enhanced growth lies in the specific chemistry of the extended pyrolysis of hydrocarbons trapped in microvoids. Microscopic asperities and micro protrusions formed as a result of mechanical abrasion are sites of intensive hydrocarbon induced dusting of the metal. Numerous microslits originate from these defects due to corrosion scattering, which in turn facilitate the emergence of sites for accelerated formation in limited volumes of carbon with a disordered structure.

2.4 Metal dusting prevention general methods

2.4.1 Precautionary techniques in the industry

The problem with metal dusting corrosion is that unless appropriate protection measures are taken, the process equipment will continue degrading to dust. This will lead to continuous and lengthy downtime, hence great expenses in the industry. Different precautionary methods are applied to mitigate metal dusting corrosion in the modern industry. Such methods include careful selection and adjustment of processing parameters, use of inhibitors (such as H_2S) to poison and/or reduce the catalytic activity on the metal surface, producing a resistant oxide scale or applying coating on the metal surface, as well as developing alloys resistant to metal dusting corrosion. These precautionary techniques and their limitations are reviewed by P. V. Daham S. Gunawardana.[15] Some of these techniques have been further developed in recent years. Thangadurai et. al.[88, 89] investigated the role of H_2S in the minimization of carbon

formation on stainless steel 304L powder samples and 304H coupons used in the ethane cracking industry by exposure to ethane-steam mixtures under convection section conditions. Their results have shown that a few ppm of H_2S can greatly alter the morphology of the carbon formed during 90 h exposures to ethane-steam mixtures. Also, they found that the addition of 10 ppm H_2S under their experimental conditions completely prevents carbon formation. In addition, mass spectrometry studies indicated that the addition of H_2S has no effect on the ethane cracking mechanism in the convection section. Their work shows the importance of maintaining optimized pO_2 and pS_2 levels to reduce catalytic and pyrolytic carbon formation and corrosion of 304H tubes. However, the added H_2S needs to be removed, otherwise, it can contaminate products or poison catalysts. Any slip of H_2S to a downstream Fischer-Tropsch or methanol catalyst will be detrimental. Furthermore, the addition and removal H_2S are also costly operations.

Surface carbon formation on the alloy can be suppressed by the application of coating on the material. Salas *et. al* [90] have deposited Cr/Cr_2O_3 thin films on 304L stainless steel substrates via modulated pulsed power magnetron sputtering (MPPMS) to investigate the protective behavior of the thin film against metal dusting corrosion for the steel. The structure of the thin films consisted of a dense fine columnar structure composed of textured Cr_2O_3, and the thin films showed good protective behavior during exposition to a carburizing atmosphere for 20 h. The main protection mechanism proposed was associated to the coating acting as barriers for inward diffusion of O and C into the alloy and outward diffusion of the alloy elements at the early stage of the exposure. Eugene Medvedovski *et. al* [91] studied coatings in model metal dusting conditions and compared to uncoated as-received or oxidized Ni-based alloys. The coatings were obtained through the thermal diffusion process and consisted of aluminide layers. They demonstrated superior performance with respect to carbon formation despite small structural changes in the surface under severe conditions. The formation of stable oxide layer provides additional protection. It is very important to have a strong bond between coating and metal/alloy substrate when applying surface coatings. Also, metal dusting corrosion could be strong where the coating damages or fails. Furthermore, the heat transfer properties of the materials should also be considered.

The development of alloys that are resistant to metal dusting corrosion is also in progress in different research groups. Nishiyama and collaborators have developed a new technique to restrain the dissociative adsorption of CO, and have applied it to the composition design of alloy NSSMC^{TM}696. [20] The formation of protective oxide scales on the alloy surface could

reduce the activity with CO containing gas. They claimed the new alloy could improve the efficiency of reforming equipment of the heat-exchanger. Fe-based superalloy doped with yttrium has demonstrated superior anti-coking and anti-carburizing properties according to Zhou and co-workers. [92] It was reported that doped yttrium can eliminate alloy intergranular coking and carburization by forming yttrium mixed oxides of $YCrO_3$ and Y_2O_3 to inhibit the aggregation of Cr_2O_3 at alloy grain boundary, thus internal Cr_2O_3 layers forms and effectively block the permeation of outer graphite during the initial coking period. However, the qualification and consistent production of the new alloys is still a challenge.

Taylor and coworkers[93] have presented the results of a pre-oxidation heat treatment on a Si-bearing Nb-stabilised 20Cr25Ni austenitic steel. The atmosphere in the heat treatment promoted the formation of a dense, continuous, protective, adherent surface scale composed of Cr_2O_3 and $MnCr_2O_4$ with a thin Si-rich oxide at the alloy oxide interface. Oxide layers with different thicknesses (125 to 350 nm) were produced by control of the moisture content of the gas on several samples and further exposed to a gas of nominal composition CO_2/1%CO/1000 vpm C_2H_4 ($a_c > 1$) at 700 °C for 4 h. Filamentous carbon could readily form on the non-pre-oxidized alloy coupons when exposed to this gas mixture. The oxide layer produced in the pre-oxidation process could suppress carbon deposition onto the alloy and a significant reduction in carbon deposit was noted with an oxide of 125 nm thickness, and no carbon deposit was found on the sample with an oxide thickness of 350 nm. This thesis focuses on this cheap and well accepted technique to produce a dense protective oxide scale on the metal surface against metal dusting corrosion.

2.4.2 Formation of surface oxide scales

The protection by a dense defect free oxide scale is generally regarded as preferred over the addition of H_2S. Oxide scale formed or grown on the alloy surface can provide an effective and relatively inexpensive way to protect the metallic matrix against a wide range of high temperature degradation phenomena.[39, 94] The properties of the oxide scale determines the corrosion resistance of the alloy, thereby, the service life of the process equipment. It is known that Cr, Mn, Al, and Si can segregate from the bulk to the surface to form a relatively stable oxide layer on the alloy surface, so these elements are often added to the alloy to enhance the resistance to oxidation and metal dusting corrosion. Ni- and Fe- based high temperature alloys are used with Cr as a major constituent in many industrial processes. Also due to high temperature stability Cr oxide scales can generally be made dense and well-adherent and have

generally good corrosion resistance.[95] Incorporation of Cr is being applied to prevent metal dusting corrosion as well since Cr_2O_3 is known to remain stable in carbonaceous atmospheres down to very low oxygen partial pressure.[96] The presence of Al in the alloy may also facilitate the formation of a protective and thermodynamically stable oxide layer.[97, 98] Moreover, the diffusion of carbon atoms through the matrix Cr_2O_3 and Al_2O_3 is not facile.[99] Protective Cr_2O_3 and Al_2O_3 surface scales have hence demonstrated excellent performance with respect to metal dusting corrosion;[61] provided a dense and defect free oxide scale that prohibits access to the bulk matrix can be formed and maintained during industrial operation.[100]

Cr_2O_3 adopts the structure of corundum, consisting of a hexagonal close packed array of oxide anions with 2/3 of the octahedral sites occupied by Cr.[101] In addition to chromium oxide, however, oxidation of alloys may lead to a wide range of spinels forming. [102, 103] Some spinels are reported to have good resistance to metal dusting corrosion, while others are unfavorable. A high Fe-content in the spinel developed on the alloy has been reported to render the surface scale non-protective against metal dusting corrosion, due to that carbon atoms may be transported through spinels with high concentration of Fe.[104] Manganese (Mn) constitutes a main alloying element in high temperature alloys since it can stabilize the austenitic structure in the Fe-Ni-Cr alloy system. Adding Mn can also help the alloy matrix suppress galling, wear and fretting even in the annealed condition. In addition, Mn is known as an element that can diffuse to the alloy surface[105]. High mobility of Mn in Cr_2O_3 [95] enables the formation of a $CrMn_2O_4$ spinel phase with Cr, and this spinel is also established as a good protective scale against metal dusting corrosion.[106-110]

2.4.3 Plastic deformation

Recently, the processing of metallic materials through the application of severe plastic deformation (SPD) has been intensively studied. The SPD processing is able to refine the grain structure of metallic materials to sub-micrometer and nanometer ranges that cannot be attained by conventional thermal-mechanical treatments. Grain size can be regarded as a key microstructural factor affecting all aspects of the mechanical and physical behavior of polycrystalline metals as well as their biochemical and chemical response to the surrounding conditions. Many important properties benefit significantly from grain refinement. Mechanical properties such as wear, strength, and ductility by way of Hall-Petch-type relations can be improved without modification of the base alloy chemistry.[111, 112] SPD processes such as Equal Channel Angular Pressing (ECAP), Accumulative Roll-Bonding (ARB) and High pressure

Torsion (HPT) have been established and enabled the formation the ultrafine grains (UFG, mean grain sizes smaller than 1 μm) in the bulk of many different metallic materials.[113] These UFG materials obtained from SPD processes perform the strength 2 or 3 times higher than that of the starting ones[114, 115], however, the uniform elongation decreases with increasing the strength in many materials with UFG[115].The SPD processing involved in grain refinement alter both the bulk and the surface of a metallic material, leading to changes in grain orientation, grain boundary density, and residual stress. These changes in the surface eventually have an impact on electrochemical performance and consequently corrosion susceptibility. The main reason for enhancements in corrosion resistance for grain-refined materials is ascribed to an enhancement in passive film formation and adhesion to the underlying substrate due to increased grain boundary density.[112]

Special equipment and/or techniques together with large amounts of energy are needed for SPD processes to produce bulk UFG materials[113]. Therefore, a composite system of a base material with sufficient mechanical strength and a protective surface layer different in structure and/or chemical composition can be an optimum choice in combining materials properties.[13] Near surface severe plastic deformation (NS-SPD) or Surface severe plastic deformation (S^2PD) processes have been developed to introduce nanograins and grain size gradients into the surface region of metallic materials.[14] Also, the ultra-grain refinement only in the near surface regions could be accomplished by simpler processes with less amount of plastic-working energy than that of bulk materials. The nanocrystalline surface generated by S^2PD has been shown to improve the wear resistance of various steels[116, 117]. The tensile yield strengths of steel and nickel-based alloy plates have been enhanced with minimum degradation in ductility[118, 119]. The fatigue resistance has also been increased by as much as 50% for a nickel-based alloy, mainly due to the combined effects of the work hardened layer and the nanocrystalline surface[120, 121]. M. Sato and coworkers have formed nanocrystalline surface layers in various metallic materials by means of the NS-SPD process using wire brushing at ambient temperature.[122] L.L. Shaw and coworkers[123] have investigated the nanocrystallization process and mechanism in a Nickel-based alloy subjected to NS-SPD. They proposed a grain-refinement mechanism led by deformation twins and complemented by dislocation activity to explain the nanocrystallization of the coarse-grained material studied in the investigation.

NS-SPD (or S^2PD) not only yield improvement in mechanical properties but also specific corrosion behavior (mostly better corrosion resistance). Materials treated by NS-SPD (or S^2PD) have a large number of structural defects, i.e., grain boundaries, dislocations, and triple

points.[124-126] Such high amounts of structural defects will lead to a significant increase in stored energy, which may increase the reactivity of the material. However, this phenomenon is expected to have a dual effect on corrosion behavior that depends upon the material-environment system[112, 124, 127]. In depassivating electrolytes (i.e., stainless steel in many aqueous environments) a nanocrystalline structure has been reported to lead to a decrease in corrosion resistance, whilst in passivating electrolytes an improvement in corrosion resistance is reported.

In the materials treated by NS-SPD (or S^2PD), the diffusivity of alloying elements is reported to be significantly higher than that in conventional coarse grained materials as a result of considerable higher fraction of structural defects.[128] B.T. Lu and co-workers have studied the effect of cold work on surface reactivity of UNS N08800 alloy in corroding environments using in situ scanning electrochemical microscopy. As they reported, the plastic deformation could increase the surface reactivity of the alloy.[129] L. Tan et al investigated the effect of shot-peening on the oxidation behavior of alloy 800H exposed to supercritical water and cyclic oxidation.[130] Their result indicates that the shot-peening processing produced a deformation zone with a depth of ~70 μm composed of two microstructural regions: an ultrafine grained region near the surface and a transition region in the sub-surface. The increased population of grain boundaries resulted in an increased Cr diffusivity to assist in the formation of Cr-rich oxides. The surface severe plastic deformation processing was also shown to mitigate oxide exfoliation on alloy 800H.

The effect of surface treatment of alloys on the resistance to metal dusting corrosion has also been investigated by several researchers. Wen-Ta Tsai and co-workers have studied the effect of surface treatment on the 304L stainless steel exposed to a mixed gas of CO/CO_2=100/1 between 500 – 700 ℃ using thermogravimetric analyses.[131] Their result showed that the formation of graphite and nano-sized carbon filaments was affected by the surface pre-treatment applied on the stainless steel. The severe surface plastic deformation yielded a sufficient amount of facile diffusion paths for Cr, which favored the formation of protective Cr rich oxide. Enhanced carbon deposition but significant resistance to metal dusting corrosion was found. Chun et.al have also studied the influence of temperature and surface finish on the corrosion process.[132] They applied surface grinding to 304 stainless steel and found that the formation of a Cr-rich spinel oxide scale is favored by a coarser alloy surface finish at high temperature corrosion, thereby providing initial protection from carbon ingress. However, rapid carbon diffusion into the steel and extensive internal carbide precipitation were triggered by the local rupture of the scale. The rapid depletion of Cr from the steel resulting from the sequential Cr-

rich oxide scale formation and Cr-rich carbide precipitation rendered it seemingly microstructurally and/or compositionally unsuitable for protective surface oxide scale formation. K.T. Voisey and coworkers have applied laser surface melting of Alloy 800H to improve the resistance to metal dusting corrosion by the formation of a protective oxide scale.[133] A refined microstructure created by laser surface melting increased the effective diffusion coefficient for Cr in the alloy by introducing a higher density of rapid diffusion paths, thereby promoting the formation of a dense, adherent, and protective oxide scale on the surface.

3 Materials and Methods

This chapter describes all the materials and methods used in the entire PhD work. A brief introduction of the materials and sample preparation procedures is given in the first two sections. An explanation of the experimental procedures is covered in the next section. All the characterization tools used in this study are summarized in the final section.

3.1 Materials

Two different high temperature alloy materials have been investigated in this work.

i. Ni-based industrial alloy Inconel alloy 601 (UNS N06601)

ii. Fe-based industrial alloy Incoloy alloy 800 (UNS N08800)

The chemical composition of the fresh alloy samples determined by EPMA/WDS is given in Table 3.1, and found to be in agreement with the specifications of Inconel 601 and Incoloy 800[134].

Alloy	Chemical composition in wt%						
	Fe	Ni	Cr	Mn	Al	Si	Ti
Inconel alloy 601	13.38	60.65	22.71	0.60	1.28	0.08	0.31
Incoloy alloy 800	47.53	30.90	21.94	1.10	0.32	0.34	0.23

Table 3.1 Chemical composition of Inconel 601 and Incoloy 800 determined by EPMA/WDS

3.2 Sample preparation

Samples of Inconel 601 and Incoloy 800 were prepared by cutting 15 mm × 8 mm coupons from 0.5 mm thick sheets. After discarding samples with serious defects found by visual inspection. Experience gained from a previous project indicates that as-received alloy samples have an oxide layer that is created under conditions not known to this project. This oxide layer as a starting point that will continue to develop during the oxidative and carburizing exposure makes it difficult to draw conclusions. Thus, all the selected coupons were subjected to grinding and polishing and most of coupons underwent a mild preoxidation to make alloy samples have a better defined starting point.[15, 29] Alloy coupons were first subjected to consecutive grindings

with P120 (100 μm), P800 (25 μm), P1200 (15 μm), P2400 (6.5 μm) and P4000 (2.5 μm) SiC papers. Properly ground coupons up to P4000 grit were subjected to polishing with 3 μm and 1 μm diamond dusts to give a mirror finish. The alloy coupons were cleaned with water and ethanol and inspected by optical microscopy after each grinding and polishing step. A tweezer was used manually to apply the near surface severe plastic deformation (NS-SPD) treatment on a sub-set of Incoloy 800 coupons. The NS-SPD treatment was performed at ambient temperature after which the NS-SPD processed sample was thoroughly cleaned with hexane and then dried overnight before the experiments.

3.3 Sample exposure

Oxidative and carburizing exposure treatments (metal dusting corrosion tests) of alloy coupons were conducted in a laboratory experimental setup with a vertical steel tube enclosed in a furnace. A schematic diagram of the reactor flow assembly used for the gas exposures is presented in Figure 3.1. Two alloy coupons separated by a platinum ring were hung by quartz rods inside the steel tube with the internal wall plated with gold to mitigate the effect of metal dusting corrosion on the reactor tube. All the gases (H_2, CO, CO_2, and Ar) fed to the reactor with the desired composition were controlled by Bronkhorst HI-TEK mass flow controllers. Steam was obtained by controlling de-ionized water via Bronkhorst LIQUI-FLOW™ controller. De-ionized water with the desired flow rate was supplied directly to an evaporator, and the resulting super-heated steam was blended with Ar (or other gases) before entering the tube reactor. System pressure was measured and controlled by a Bronkhorst EL-PRESS digital electronic back pressure controller. All the controllers were regulated by two Bronkhorst controller-readout boxes. Temperatures of heating zones of the tube reactor were monitored by type-K thermocouples and the temperature of the furnace was controlled by Eurotherm 2416.

3.3.1 Pre-oxidation (Thermal) treatments

Most of the alloy coupons were pre-oxidized in 10% steam in Ar at 540 ˚C for 6 h at 1 bar. After loading the alloy coupons in the setup, a leakage test was carried out. Before any experiments, leak free setup was flushed with 100 Nml/min Ar for 20 min at room temperature. After ramping up the temperature by 5 ˚C/min in pure Ar, 10 vol% steam in Ar were introduced to the reactor when the temperature was stabilized at 540 ˚C and the alloy coupons were dwelled

for 6h. The resulting oxidized alloy coupons were either unloaded for characterization or kept in the reactor for further thermal treatments and/or metal dusting corrosion tests.

3.3.2 Metal dusting corrosion test with infinite carbon activity ($a_c \gg 1$)

Pre-oxidized alloy coupons were ramped up to either 550 ˚C, 650 ˚C, or 750 ˚C in Ar and kept for 20 min to stabilize the temperature. The metal dusting corrosion tests were thereafter induced using 10 vol% CO in Ar, a gas mixture with infinite carbon activity ($a_c \gg 1$) for up to 100 hours. After the corrosion tests, the alloy coupons were cooled in Ar, unloaded at ambient

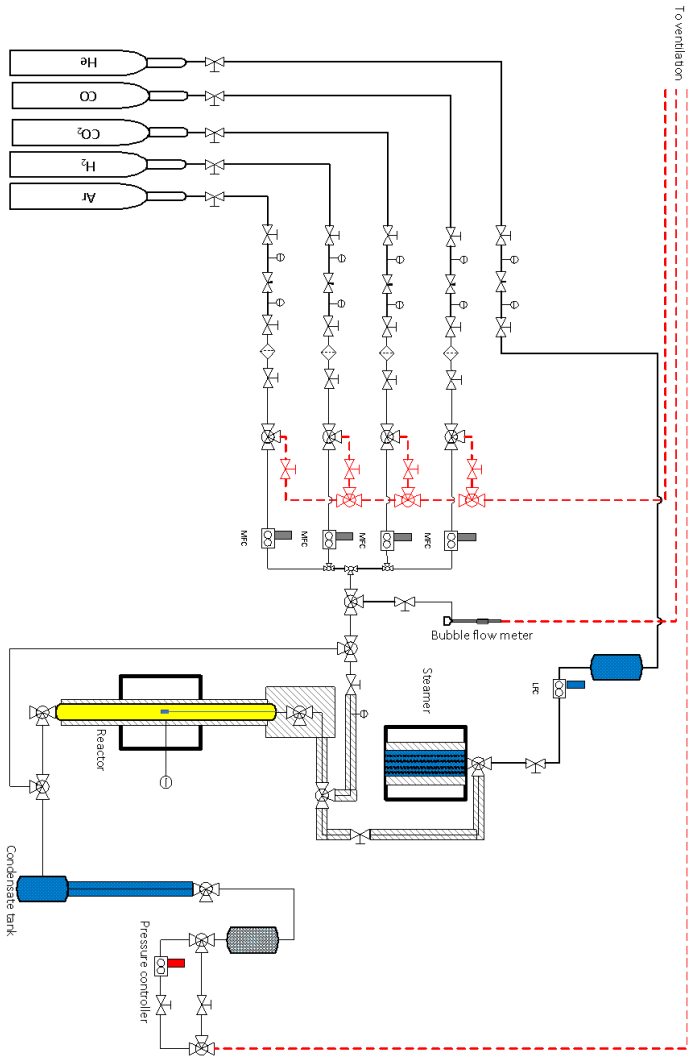

Figure 3.1: Schematic diagram of the reactor flow assembly used for metal dusting corrosion tests.

conditions and stored for further characterization. The total system pressure was 1 bar and the total gas flow rate was 100 Nml/min in all experiments.

3.3.3 Metal dusting corrosion test with finite low carbon activity (a_c~7)

Pre-oxidized alloy coupons were ramped up to either 550 ˚C, 650 ˚C, or 750 ˚C in Ar and kept for 20 min to stabilize the temperature while Ar was flowing at a rate of 300 Nml/min to pressurize the system pressure to 20 bar. Then a gas mixture with infinite carbon activity (FL-a_c) containing H_2 (25 vol%), CO (20 vol%), CO_2 (15 vol%), H_2O (10 vol%) and Ar (30 vol%) with total flow rate at 100 Nml/min was switched to the reactor when the system pressure reached 20 bar. The exposure tests were normally conducted for 20 hours, with a few longer extending tests up to 100 hours.

3.4 Characterization

Alloy coupons were characterized after polishing, after surface treatment (NS-SPD), after pre-oxidation as well as after oxidation followed by metal dusting corrosion test. The characterization techniques used include visual inspection, optical microscopy, scanning electron microscopy (SEM), energy dispersive X-ray spectroscopy (EDS), electron probe micro analysis (EPMA), Grazing Incidence X-ray Diffraction (GIXRD), Auger electron spectroscopy (AES), focused ion beam (FIB), transmission electron microscopy (TEM) and Raman spectroscopy.

3.4.1 Optical microscopy

Optical microscopy is a well-established technique employed to view small objects closely through the magnification of a lens with visible light[135]. The surface morphologies of alloy coupons before and after metal dusting corrosion tests were observed under a Leica MZ 9.5 optical microscope.

3.4.2 Scanning electron microscopy (SEM)

An SEM is one type of electron microscope that scans a focused electron beam over a surface to obtain an image.[136] The electrons in the beam interact with the sample, producing various signals that can be collected and analyzed to obtain information about the surface topography and composition.

Polished alloys coupons before and after metal dusting corrosion test were investigated using a FEI APREO field emission scanning electron microscope equipped with an Oxford Xmax 80 mm^2 Solid angle EDS (see section 3.4.4).

3.4.3 Transmission electron microscopy (TEM)

Transmission electron microscopy (TEM) is a technique used to observe the features of very small specimens.[137] A high energy electron beam is shone through a very thin sample, and the interactions between the electrons and the atoms are used to observe features such as the morphology, crystalline structure, and features in the structure like dislocations and grain boundaries. The TEM operates on the same principles as a light microscope but uses an electron beam instead of light. However, the optimal resolution attainable for TEM images is many orders of magnitude better than that from a light microscope because the wavelength of electrons is much smaller than that of light. As a result, TEM produces high-resolution, two dimensional images, allowing to reveal the finest details of internal structure, in many cases as small as individual atoms. In addition to looking at the transmitted image, it's possible to use electron diffraction to image the crystal structure of the samples. Furthermore, the composition of the specimen can also be obtained by measuring the characteristic X-rays with and EDS spectroscope and electron energy loss spectroscopy (EELS).

TEM analysis of lamellae prepared by FIB from selected alloy coupons was done on a double Cs aberration corrected cold FEG JEOL ARM 200F, operated at 200 kV and equipped with a large solid angle Centurio SDD (0.98 sr) for EDS and a Quantum ER GIF for dual electron energy loss spectroscopy (EELS).

3.4.4 Energy dispersive X-ray spectroscopy (EDS)

EDS is an analytical technique used for chemical characterization or elemental analysis of a sample. The X-ray spectrum emitted by a sample bombarded with a focused beam of electrons is analyzed to obtain a localized chemical analysis.[138] In principle, all elements from atomic number 4 (Be) to 92 (U) can be detected by EDS.

Cross-sections of selected samples were prepared and subjected to FEG JEOL ARM 200F TEM equipped with a large solid angle Centurio SDD (0.98 sr) for EDS.

3.4.5 Electron probe micro-analysis (EPMA)

EPMA is a fully quantitative and qualitative method of non-destructive elemental analysis of micron-sized volumes (1-2 microns) at the surface of materials, with sensitivity at the level of ppm.[139] EPMA works by bombarding a small sample volume with a focused electron beam and collecting the X-ray photons thereby emitted by the various elemental species. Since the wavelengths of these X-rays are characteristic of the emitting species, the composition of the sample can be identified easily by recording wavelength dispersive spectroscopy (WDS). Because of the internal properties of WDS, the sensitivity, the analysis of light elements, and accuracy of interpretation of qualitative spectra, EPMA provides better results than standard SEM equipped with EDS.

The bulk composition of polished Inconel 601 and Incoloy 800 alloy coupons were analyzed by JEOL JXA-8500F high performance thermal field emission electron probe micro analyzer (EPMA) equipped with 5 WDS and an EDS.

3.4.6 Grazing Incidence X-ray Diffraction (GIXRD)

X-ray diffraction (XRD) provides information on unit cell dimensions and can be used for phase identification of crystalline material.[140] In conventional XRD with large incident angles, the X-ray beam penetrates deep into a material and generally produces an intense signal from the bulk but only weak signals from the near surface region. To limit the incident X-ray beam penetration to the surface, grazing incidence X-rays are needed. Grazing incidence X-rays use small incident angles for the incoming X-ray so that diffraction can be made surface sensitive.

The near surface regions of Inconel 601 and Incoloy 800 alloy coupons were analyzed by Bruker D8 A25 DaVinci X-ray Diffractometer with CuKα radiation equipped with LynxEye™ SuperSpeed Detector.

3.4.7 Auger electron spectroscopy (AES)

AES is an analytical technique used in the area of materials science, specifically in the study of the chemical composition of surfaces.[141] The Auger principle operates by bombarding a sample by an accelerated and focused electron beam allowing a high energy electron from a higher orbit moves to fill the empty space. As the electron changes from a higher orbit to a lower one, it releases energy. This energy might eject a third electron (Auger electron) from another orbit. By measuring the energy of the emitted Auger electron, the atom can be identified.

Depth profile analysis by AES under Ar ion sputtering is used to study the depth-wise concentration variation of elements of the oxide scale on the alloy coupons. The depth-wise concentration variation of C, O, Cr, Ni, Fe, Al, Ti, Mn, and Si, etc. were obtained in a JEOL JAMP-9500F Field Emission Auger Microprobe. The analysis was performed at 30° tilt under Ar^+ of 1 keV. The obtained depth profiles provide semi-qualitative information about the thickness of the oxide scales. The depths estimated here refer to the sputtering of a standard SiO_2 sample.

3.4.8 Focused ion beam (FIB) sputtering

Focused ion beam (FIB) is a tool for manipulating the structure of a wide range of materials including metals, ceramics, polymers, semiconductors, biological materials, and tissues at the nanoscale. FIB micromachining uses highly focused ion beams to bombard a target material, thereby sputtering atoms from the target surface within a vacuum chamber. [142] The FIB system can be used for milling, deposition, implantation, and imaging. The focused ion beam can directly mill the specimen surface, and this milling can be controlled at the nanometer level. Also, chemical vapor deposition (CVD) assisted by ion beam can be used to deposit material with the same precision level to FIB milling. FIB is nowadays widely used as a tool for the preparation of site-specific transmission electron microscopy (TEM) specimens by thin lamella extraction through the lift-out technique.

All the cross-section TEM lamellae were prepared from selected alloy coupons by an FEI Helios G4 PFIB UXe equipped with EasyLift EX NanoManipulator. Platinum or carbon protection layers were deposited on the selected regions prior to cutting out the TEM lamella. The coarse thinning of the TEM lamellae was performed at 30 kV acceleration voltage. The later part of the thinning was performed at 5 kV and finally 2 kV on either side of the TEM lamellae to minimize ion-beam induced surface damage. The process is presented in **Figure 3.2**.

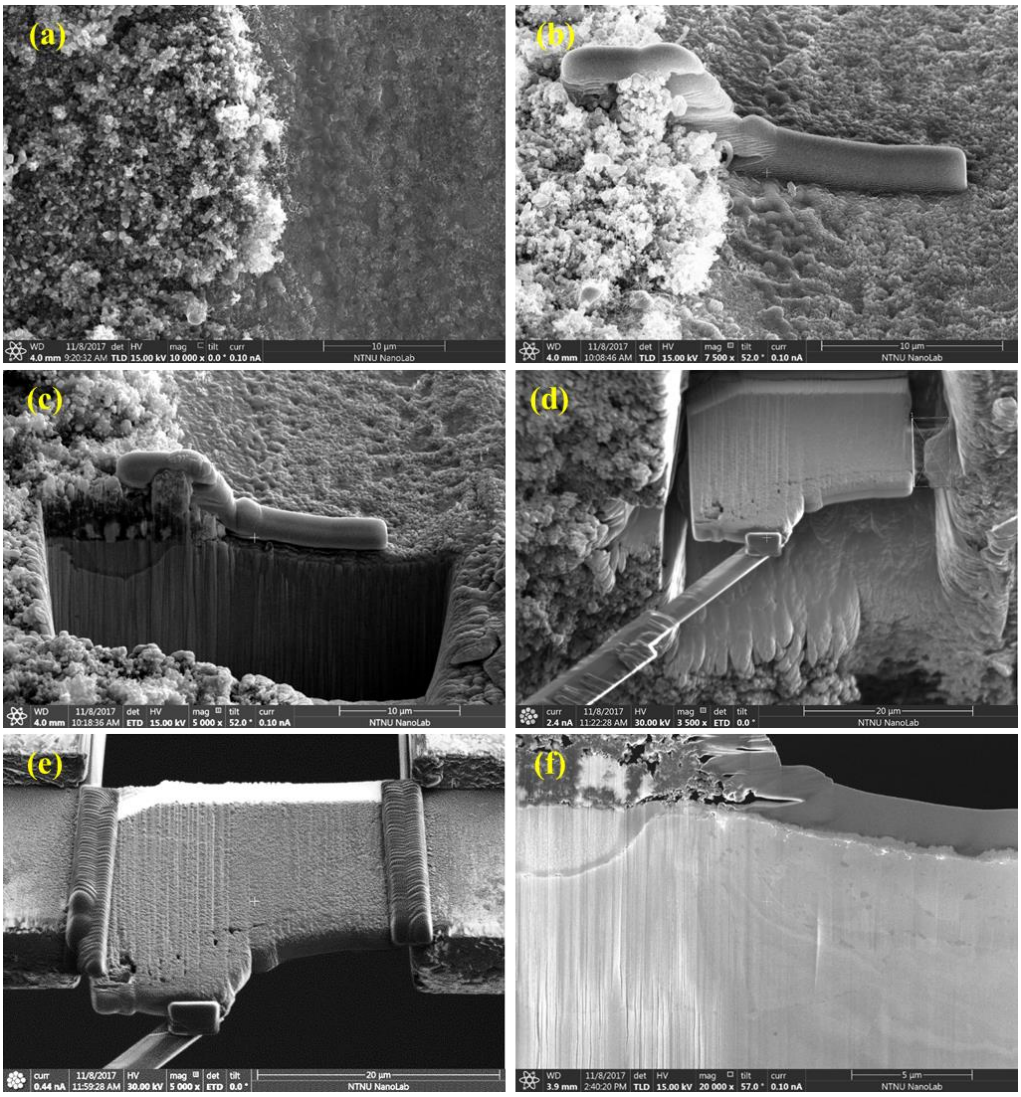

Figure 3.2: SE images of a FIB prepared TEM lamella through (a) select the ROI (region of interest) on the sample, (b) Protection layer is deposited on the ROI by coating of carbon or platinum, (c) Surroundings of the ROI are roughly milled with Ga ion beam to prepare a slice (thickness: a few μm or less), (d) A tungsten needle "welded" to the slice (e) Attachment of slice to a TEM grid, (f) Thin lamella (thickness: 10 - 100 nm) is created from the slice by coarse and fine milling and ready to be analyzed by TEM.

3.4.9 Raman spectroscopy

Raman spectroscopy is a spectroscopic technique typically used to detect vibrational, rotational, and other states of molecules based on inelastic scattering of monochromatic light from a laser source.[143] The gross selection rule in Raman spectroscopy is that the vibration must lead to a change in polarizability, and it is hence complementary to IR spectroscopy.[144] Bonds that are relatively neutral, such as C-C, C=C, and C-H, undergo large changes in polarizability during vibration and therefore have very active Raman features. Thus, Raman spectroscopy provides an analytical tool for molecular fingerprinting and monitoring changes in molecular bond structure, and it is also capable of probing the chemical composition of materials. Raman spectroscopy provides a nondestructive technique for structure characterization of carbon materials and oxide scales.

Raman spectra of selected alloy coupons were collected by focusing on a Horiba Jobin Yvon LabRAM HR800 spectrometer, the emission line at 633 nm from a He–Ne laser on the samples with a 50× LWD objective with a motorized x–y stage. The output power of the laser was 8.25 mW with a spot diameter of approximately 1.5 μm. Spectral measurements were performed with continuous scans in the range of 300–3000 cm^{-1}. **Figure 3.3** displays an example of the Raman spectrum of deposited carbon materials on Incoloy 800 after metal dusting corrosion test. Characteristic peaks of carbon (so-called D, 2D, and G bands) are confirmed by the Raman spectrum. The position and ratio of these peaks are indicative of the type and crystallinity of the carbon.

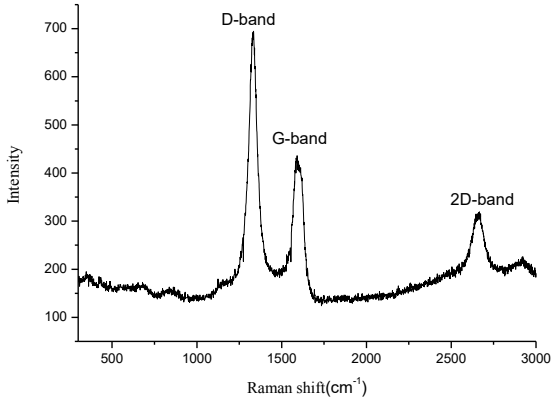

Figure 3.3: Raman spectrum of the surface of polished Incoloy 800 after oxidation (10% H_2O in Ar, 540 ˚C, 1bar for 6h) and then exposure to a carburizing gas mixture with infinite carbon activity (10% CO in Ar, 550 ˚C, 1bar for 2h)

4 Main Results and Conclusions

4.1 Carburization and oxidation of Inconel 601

Nickel-based alloy (Inconel 601) samples have been pre-oxidized in 10% steam in Ar at 540 for 6h before exposure to two different metal dusting conditions at 750 ˚C. We have shown that by varying the exposure times over relatively short exposures, we may capture the initiation and progress of carbon formation on alloy surfaces that eventually lead to metal dusting. The carbon deposition is clearly a function of the gas composition during exposure. After exposure to 10% CO in Ar (1 bar), i.e infinite carbon activity (I-a_c) for 1 h (Figure 4.1 (a)), the alloy sample displays short carbon filaments with nanoparticles at the tip. For the sample exposed to synthesis gas with finite low carbon activity(FL-a_c; 25% H_2, 20% CO, 15% CO_2, 10% H_2O, and 30%Ar, 20 bar) (Figure 4.1 (b)), no carbon filament was observed. After 20 h, less carbon has formed under I-a_c(Figure 4.1 (c)), than under FL-a_c(Figure 4.1 (d)). However, the formation of carbon under FL-a_c exhibits a longer induction period than under I-a_c, but more facile growth after the first 1-2 h. SEM confirms the formation of filamentous carbon for both exposures, albeit overall larger diameters with H, CO_2, and H_2O present in the mixture. Moreover, Raman spectroscopy reveals significant differences in the nature of the carbon formed (Figure 4.1 (e)). With only CO reacting (I-a_c), more ordered carbon develops as the exposure time increases, while this is not case under synthesis gas. Combined, this points to a difference in the catalytic reaction mechanism and kinetics on the surface.

In addition, XRD, Raman, and TEM characterization reveal that the surface oxide layer formed on Inconel 601 develops very differently under the two metal dusting conditions applied. Cr_2O_3 develops as a thin surface oxide scale layer under exposure to CO in Ar. The Cr_2O_3 / spinel peak ratio is increasing during the exposure to I-a_c, however, the Cr_2O_3 / spinel peak ratio is practically constant during the exposure to FL-a_c (Figure 4.1 (e)). A more fine-grain structure present near the surface in certain regions on this sample is found important in terms of rapidly supplying Cr, Mn, and Al to the surface under elevated temperature to form a dense, protective layer and thereby slowing the metal dusting corrosion. TEM analysis captured another interesting evolution under I-a_c(Figure 4.1 (f)), which suggests “purification” of the catalyst particles along with carbon filaments growth as a possible reason for the improved overall crystallinity of the carbon formed during prolonged exposure. In presence of synthesis gas (FL-a_c) (Figure 4.1 (g)), oxidation proceeds within a larger part of the near-surface region, but results

to a larger extent in (Ni, Fe, Cr)$_3$O$_4$ spinel formation. We suggest that this phase continuously forms and reduces to new carbon formation catalyst (Ni, Fe) particles that nucleate the formation of more, less ordered carbon.

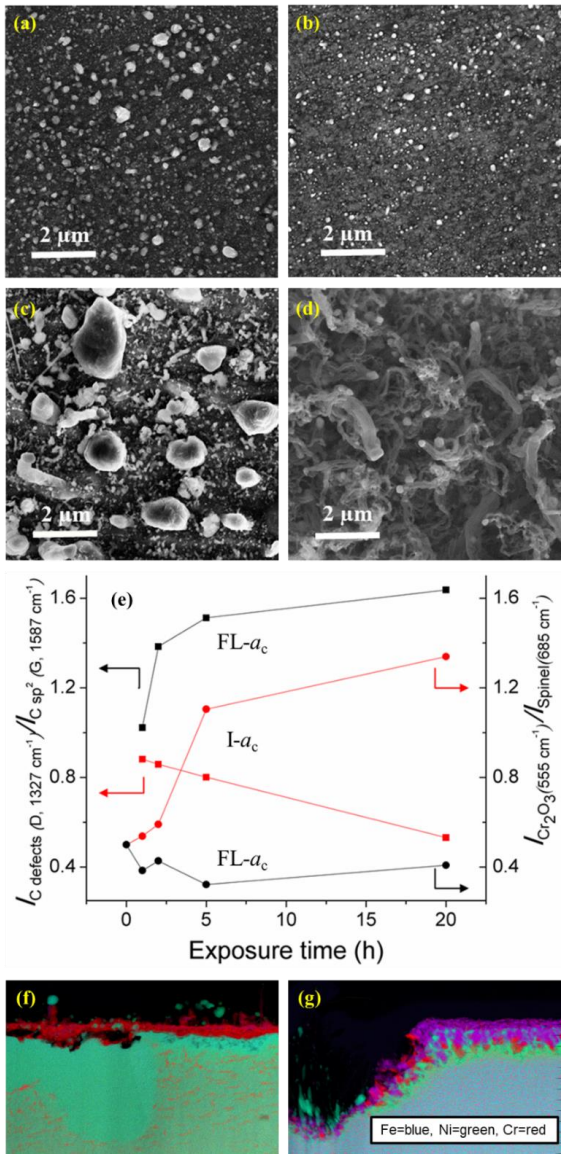

Figure 4.1 SEM micrographs of oxidized Inconel 601 surface after exposure to infinite carbon activity (I- a_c) at 750 °C for 1 h (a), and 20 h (c); after exposure to finite low carbon activity (FL-ac) at 750°C for 1 h (b), and 20 h (d); (e) I_D/I_G intensity ratios of the Raman spectra for oxidized Inconel 601 after exposure to I-a_c or FL-a_c plotted as a function of exposure time; RGB element merge of

selected regions of TEM lamellae milled by FIB from oxidized Inconel 601 sample after exposure at 750°C for 20 h to I-a_c (f) and FL- a_c (g)

4.2 Investigation of metal dusting corrosion over Incoloy 800

Fe-based Incoloy 800 alloy samples have been pre-oxidized in 10% steam in Ar at 540 °C for 6 hours at 1 bar before exposure to a highly carburizing gas mixture in order to understand the initial carbon formation preceding metal dusting corrosion. Figure 4.2 (a) shows the alloy surface after the pre-oxidation. Raman spectra indicate that the alloy surface is covered by Fe_3O_4 and Cr_2O_3. The amount of carbon formed on Incoloy 800 alloy is clearly a function of exposure temperature (Figure 4.2 (b), (c), and (d)). Increasing exposure temperature under CO-Ar gas appears to result in lower carbon formation as assessed by the amount of filamentous carbon. In addition, pits are observed in the surface upon removal of the loosely adhered carbon deposits and corrosion products for the exposure at 550 °C, while this is not the case for 650 and 750 °C. Raman spectroscopy shows, however, that several types of carbon have formed. Amorphous carbon remained on the surface of the Incoloy 800 alloy after ultrasonic cleaning in acetone. In addition, some carbon islands formed at 750°C that also remained after ultrasonic treatment are significantly more resistant to sputtering than the surrounding surface. These islands show similar Raman spectral features as the loosely bound deposits and corrosion products present on the sample before cleaning. These common spectral features are characteristic of more ordered carbon which may use amorphous carbon as an anchor (or template) for its formation. The amorphous layer may hence be the first to be synthesized during the CO exposure, giving a first insight of how some more ordered carbon nanostructures may be catalytically synthesized on top of disordered and amorphous carbon. Some of the carbon nanostructures on top of amorphous carbon also seem to be in the middle of a grain and extremely well anchored to the amorphous carbon layer beneath, even after ultrasonic agitation in acetone.

The Auger sputtering depth profiles of pre-oxidized Incoloy 800 samples after exposure to 10% CO in Ar carburizing mixture for 20 h at 550 ˚C and 750 ˚C and removal of corrosion products are shown in Figure 4.2 (e) and (f). The dissociation of CO on the alloy surface may lead to inward diffusion of both oxygen and carbon that can react with metal components in the alloy. The O-rich zone becomes thicker after exposure to CO and the sample which underwent 750 ˚C exposure shows the thickest layer. Cr enrichment in the oxide region is clear in the case of CO exposure at 750 ˚C, while a slight depletion upon exposure at 550 ˚C. Ni and Fe content in the O-rich layer is

depleted with increasing exposure temperature. Carbon concentration within the O-rich layers is rather low, but the penetration of C into the bulk has also occurred. This is particularly notable for the 550 ˚C exposure where significant Cr enrichment has not taken place.

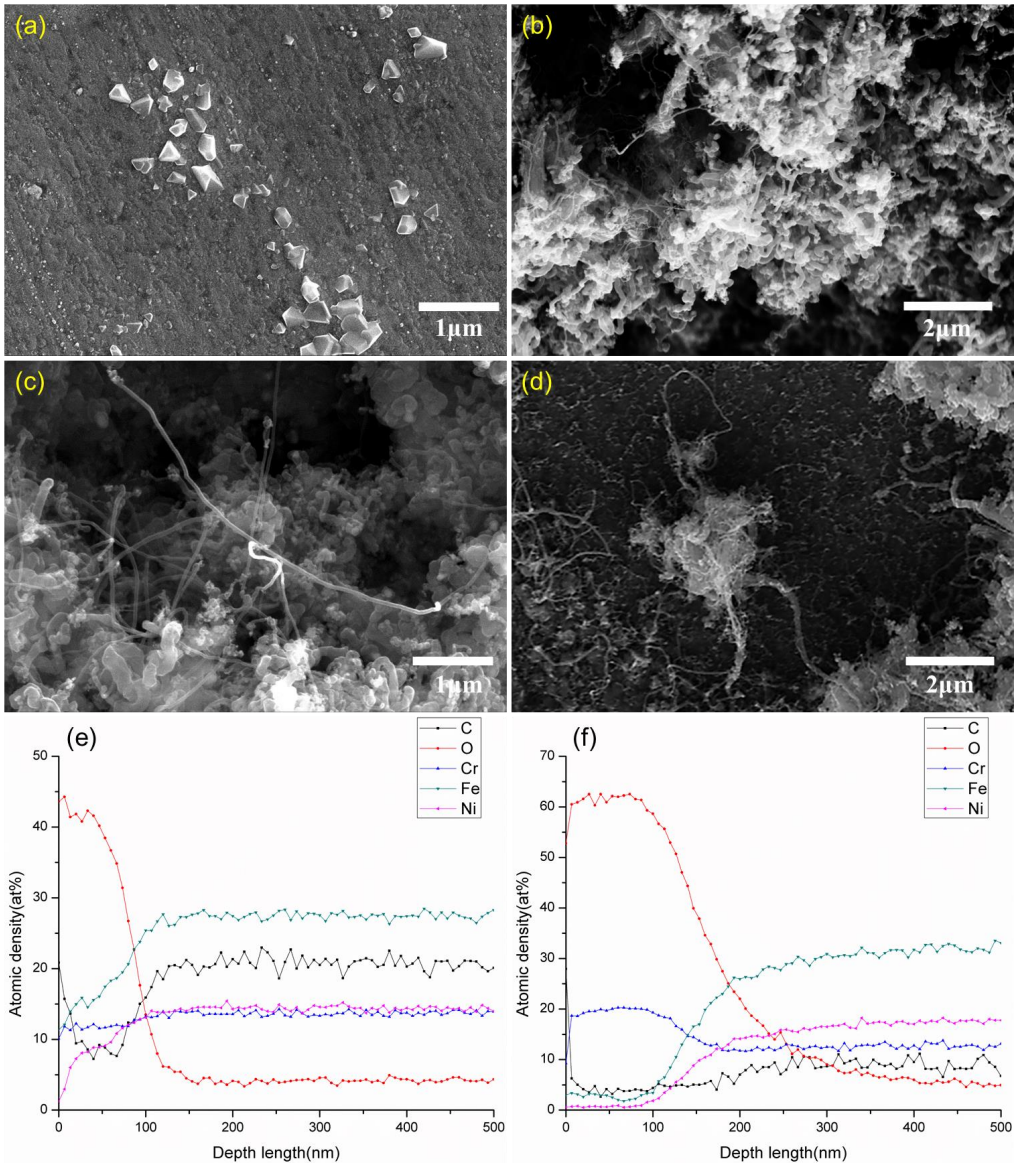

Figure 4.2 SEM micrographs of polished Incoloy 800 samples after pre-oxidation (a), and after exposure to the 10% CO in Ar for 20h: (b) 550 ˚C; (c) 650 ˚C; (d) 750 ˚C. Total pressure 20bar; Auger depth profiles of the sample after exposure at 550 ˚C (e) and 750 ˚C (f).

4.3 Inhibition of metal dusting corrosion on Incoloy 800

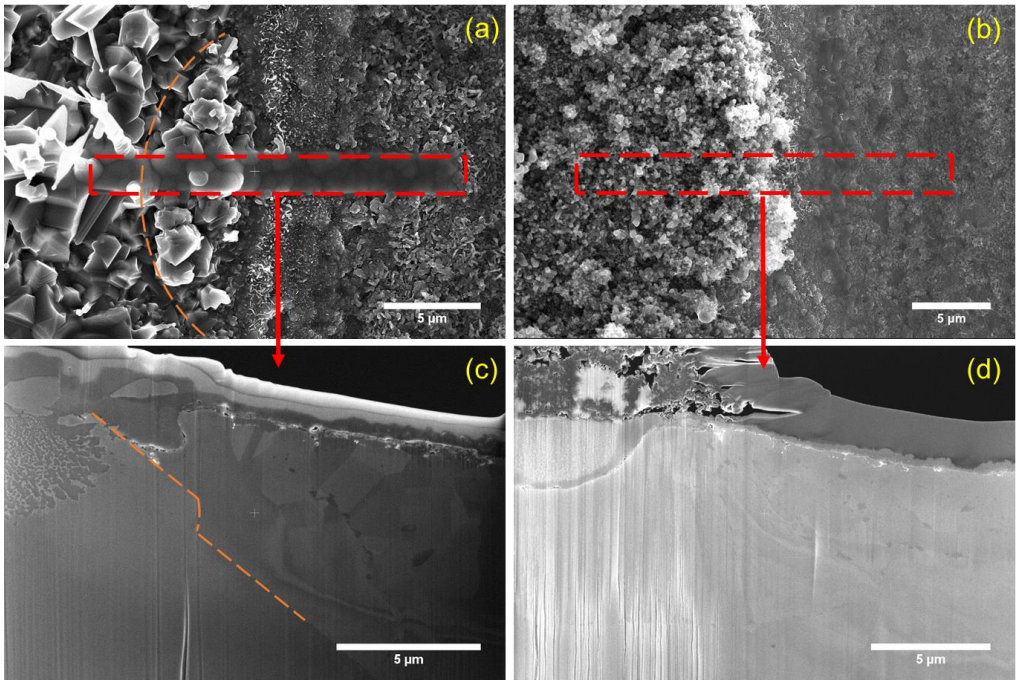

Figure 4.3. SEM surface view of polished alloy samples with right part treated by NS-SPD: (a) Alloy sample after second step preoxidation, a thin protection layer of Pt was deposited on the alloy surface before ion milling and can be observed in the red square. Cross-section TEM lamella showed in (c). A grain boundary visible on the sample surface in (a) is marked with orange dash lines both in (a) and (c). (b) Alloy sample after the corrosion test, a cross-section TEM lamella is prepared from the area in the red squares shown in (d).

The research on Inconel 601 indicated that the fine-grain structure present near the surface on the sample is important in terms of rapidly supplying Cr, Mn, and Al to the surface under oxidizing conditions at elevated temperature. A dense and more protective layer could be formed, thereby slowing the metal dusting corrosion. Here, we used a metal process technique called near surface severe plastic deformation (NS-SPD) to create a high density of deformation microstructures, such as dislocations and twins, in the near surface region of Incoloy 800. Under the treatments and conditions applied, the microstructures developed into refined micro-structure that increase the effective diffusion coefficient for Cr and Mn in the alloy by introducing a higher density of rapid diffusion paths. This promoted the formation of a protective oxide layer.

TEM cross section analysis of the processed samples after second step peroxidation show that the NS-SPD region is covered by a thin (ca. 300-600 nm) Cr-rich oxide layer depleted of Fe and Al compared to a thick (ca. 8 μm) oxide layer developed in the polished (non-NS-SPD) region after thermal treatment (Figure 4.3 (a), (c) and Figure 4.4). After a 20 h corrosion test with infinite carbon activity (I-a_c) the NS-SPD region shows no dissimilarity, neither carbon filaments nor carbon containing phases could be found in SEM or Raman spectra. While thick corrosion products containing C, Ni, and Fe particles could be observed on top of the polished region, no carbon material is produced in the NS-SPD region (Figure 4.3 (b), (d), and Figure 4.5) even upon prolonging the corrosion test to 100 h. This indicates that the corrosion resistance of Incoloy 800 samples has been successfully improved by combined NS-SPD and thermal treatment. Also, since internal oxidation is prevented in the NS-SPD region, this method may also inhibit internal inter-granular oxidation embrittlement. The new alloy pretreatment method may have a broad influence on not only metal dusting, but also in other corrosion areas such as steam generator, ethylene furnace and supercritical water-cooled reactor where a dense Cr-rich oxide scale is also highly demanded.

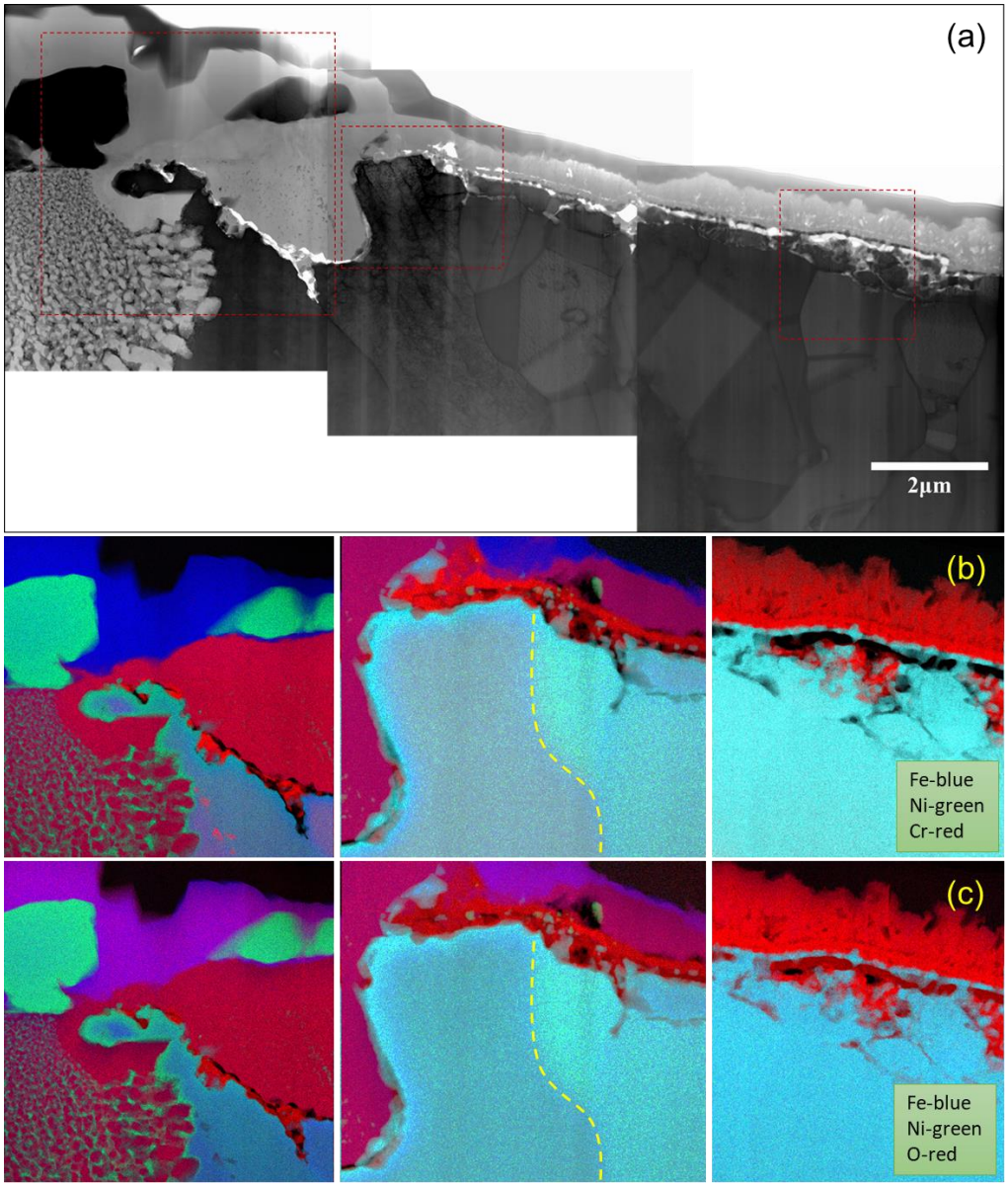

Figure 4.4. TEM lamella prepared by FIB milling from the sample after second step preoxidation in at 750˚C for 20h as indicated in figure 4.3(c): Stitched bright field transmission electron microscopy (TEM) images with three areas marked by red dash square for EDS analysis (a). RGB color-coded images of three regions: Cr (red), Ni (green) and Fe (blue) (b) and O (red), Ni (green) and Fe (blue) (c).

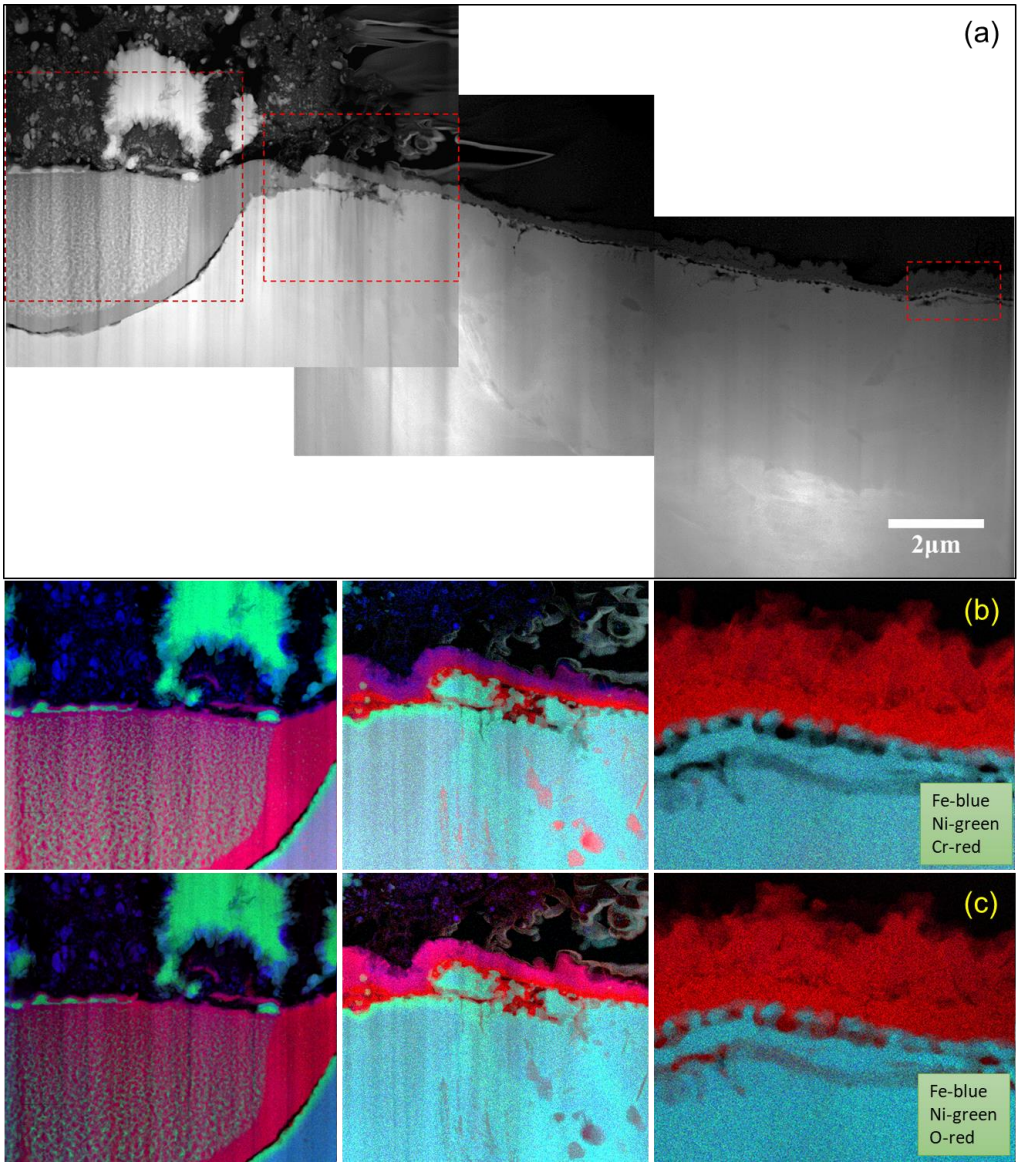

Figure 4.5. TEM lamella prepared by FIB milling from the sample after metal dusting corrosion test in at 550˚C for 20h as indicated in figure 4.3(d): Stitched bright field transmission electron microscopy (TEM) images with three areas marked by red dash square for EDS analysis (a). RGB color-coded images of three regions: Cr (red), Ni (green) and Fe (blue) (b) and O (red), Ni (green) and Fe (blue) (c).

4.4 Conclusions

Efforts have been given to advance the understanding of the initial stages of metal dusting corrosion over two high temperature alloys, i.e. Ni-based Inconel 601 and Fe-based Incoloy 800 and propose a pretreatment method to inhibit the corrosion. The formation of carbon on the alloy surface was studied as a function of exposure time, temperature, and composition of the carburizing gas mixture. The investigation was combined with detailed characterizations of the *preoxidized* samples before and after the carburizing gas exposure to find the relationship between the nature of the oxide and its propensity to form carbon filaments.

For *Ni-based alloy Inconel 601*, less carbon is formed under infinite carbon activity (10% CO in Ar) than under synthesis gas with finite low carbon activity at 750 ˚C, and the carbon becomes more ordered with increasing exposure time. This is due to a thin oxide scale rich in Cr_2O_3 developing during the exposure. In contrast, prolonged exposure to synthesis gas yields $(Ni, Fe, Cr)_3O_4$ spinel while the carbon formed retains its disordered character. Hence, a marginal Cr_2O_3 stabilization in absence of O_2 or H_2O is sufficient to lower the metal dusting corrosion rate, while the $(Ni, Fe, Cr)_3O_4$ spinel represents an unstable redox state that grows and continuously yields new carbon formation. Also, a fine-grained surface structure is established as beneficial for the formation of the Cr_2O_3-rich protective oxide.

With respect to the *Fe-based alloy Incoloy 800*, more carbon filaments were formed when decreasing the exposure temperature from 750 ˚C to 550 ˚C under 10% CO in Ar at 20 bar. Moreover, upon removal of the loosely adhered corrosion products and carbon deposits, pits were observed on the alloy surface after exposure at 550 ˚C, but not at 650 ˚C and 750 ˚C. Raman spectroscopy reveals that amorphous carbon is first synthesized from CO, with more ordered carbon growing on top of the amorphous carbon.

Finally, the research performed shows how the metal dusting corrosion resistance of Incoloy 800 can be significantly improved by combined *near surface severe plastic deformation (NS-SPD)* followed by *thermochemical treatment*. A higher density of dislocations and other crystal lattice defects were introduced into the near surface region by the NS-SPD treatment. Recrystallization during the following thermochemical treatment results in an ultrafine grain structure. Rapid Cr diffusion paths provided by grain boundaries and dislocations promote the formation of *a protective, Cr rich, oxide scale, which completely prevents carbon formation* when exposing to the carburizing gas mixture. Conversely, the non-NS-SPD region developed an external Fe_3O_4 oxide and internal, Cr rich oxide phases in the thermochemical process, which

are not protective and significant corrosion products were found after exposure to the carburizing gases. We believe that there is potential to develop commercial protection technologies for high temperature alloys from this discovery.

5 Recommendations for Further Research

The present work has been focused on certain aspects of how the pre-oxidized alloy coupons behave in different metal dusting corrosion conditions and how to develop a dense and defect-free oxide scale to inhibit metal dusting corrosion. Based on the results obtained and the experience gained, some suggestions for improving the experimental rig and some new areas considered interesting for further research are presented.

- **Experimental rig improvement**

After modification of the mounting method in the existing rig, treatment of two samples instead of one is allowed. There is still room for improvement, like to change the reactor from vertical to horizontal alignment to make the mounting/dismounting procedure more convenient, and/or to make the diameter of the reactor large allow producing more parallel samples.

- **Further explore the conditions of thermal treatment after NS-SPD**

The two-step thermal treatment after NS-SPD we developed so far uses different temperatures, different pressures, and different atmospheres. These conditions enabled oxidation of Cr and Mn diffused from the near surface region while keeping Fe and Ni in the metallic state in the bulk. Such a goal might be achieved by more simple conditions i.e. more simple gas compositions, lower total pressure, lower temperature, etc. Studying the role of each gas could also worth some attention.

- **Failure study of the obtained "protective" oxide scale.**

"Every failure is a step to success." Though the protective oxide scale on the Incoloy 800 developed by combined NS-SPD and thermal treatment showed very good resistance to metal dusting corrosion for up to 100 hours, we believe that every protective scale will not be remaining intact after exposure to harsh conditions. Thermal cycling could make strains between oxide and substrates, thus pose a significant threat to the integrity of the protective oxide scale. Running the corrosion test under rapid thermal cycling conditions or prolonging the current CO exposure time from 100h to 1 month (or even longer) to test the performance of the protective oxide scale is needed too. Finding the reason for the failure of the oxide scale could guide us to further improvement of the pre-treatment method, both in the NS-SPD and in the following thermal treatment procedure.

- **Extend the current method to other alloys and applications**

The current pre-treatment method should be modified to extend such method to other high-temperature alloys such as Inconel 601 to develop a similar protective oxide scale against metal dusting corrosion. Also, such a dense Cr-rich oxide scale is highly desired in many other applications such as steam generator[129, 145, 146], ethylene furnace[147], and supercritical water-cooled reactor[148] where a dense Cr-rich oxide scale is also highly demanded.

- **Investigate the current method to weld joints**

Weld joints and the heat affected zones near the weld normally attacked even stronger than the straight machined sections. The microstructure and composition of the welded joints caused enhanced attack. Test our combined NS-SPD and thermal treatment method on the welded joint may be worth considering.

- **Employ density functional theory and reactive force field molecular dynamics simulations**

The first carbon nucleation on the alloy surface is result from dissociative adsorption of carbon precursors, subsequent carbon growth, and finally also solid state reactions leading to metal dusting corrosion. Metal dusting corrosion is closely related to carbon nucleation and growth processes on the molecular level. Density functional theory (DFT) is a quantum mechanical modelling method to investigate the nuclear structure of many-body systems, while molecular dynamics simulates the physical movements of atoms and molecules. Therefore, density functional theory (DFT) and reactive force field molecular dynamics simulations could be used as powerful tools in the investigations of metal dusting. These two methods could be employed to investigate the effect of surface conditions on the alloy oxidation and carbon species activation directly related to metal dusting corrosion. For example, the effect of surface defects and the role of hydrogen in the carburizing atmosphere on the CO dissociation.

Bibliography

1. Grabke, H., Metal dusting. *Mater. Corros.* **2003,** *54* (10), 736-746.
2. Grabke, H.; Krajak, R.; Paz, J. N., On the mechanism of catastrophic carburization:'metal dusting'. *Corros. Sci.* **1993,** *35* (5-8), 1141-1150.
3. Young, D. J.; Zhang, J.; Geers, C.; Schütze, M., Recent advances in understanding metal dusting: A review. *Mater. Corros.* **2011,** *62* (1), 7-28.
4. Grabke, H., Thermodynamics, mechanisms and kinetics of metal dusting. *Mater. Corros.* **1998,** *49* (5), 303-308.
5. Yin, H.; Zhang, J.; Young, D. J., Effect of gas composition on coking and metal dusting of 2.25 Cr–1Mo steel compared with iron. *Corros. Sci.* **2009,** *51* (12), 2983-2993.
6. Grabke, H. J., Metal dusting. *Mater. Corros.* **2003,** *54* (10), 736-746.
7. Zeng, Z.; Natesan, K., Relationship of carbon crystallization to the metal-dusting mechanism of nickel. *Chem. Mater.* **2003,** *15* (4), 872-878.
8. Holland, M.; De Bruyn, H., Metal dusting failures in methane reforming plant. *International journal of pressure vessels and piping* **1996,** *66* (1-3), 125-133.
9. Tomkings, A. B.; Lant, T. In *Operating Experience of Metal Dusting Failures*, CORROSION 2001, NACE International: 2001.
10. Kaewkumsai, S.; Khonraeng, W.; Sathirachinda, N., High temperature failure of natural gas feed burner pipe. *Engineering Failure Analysis* **2013,** *27*, 74-83.
11. Orlikowski, J.; Jazdzewska, A.; Darowicki, K.; Karczewski, J.; Dampc, J.; Gospos, R., Metal dusting phenomena of 501 AISI furnace tubes in refinery fractional distillation unit. *Engineering Failure Analysis* **2018,** *91*, 108-114.
12. Venvik, H. J.; Yang, J., Catalysis in microstructured reactors: Short review on small-scale syngas production and further conversion into methanol, DME and Fischer-Tropsch products. *Catal. Today* **2017,** *285*, 135-146.
13. Stroosnijder, M.; Mevrel, R.; Bennett, M., The interaction of surface engineering and high temperature corrosion protection. *Mater. High Temp.* **1994,** *12* (1), 53-66.
14. Ke, L.; Jian, L., Surface nanocrystallization (SNC) of metallic materials-presentation of the concept behind a new approach. *J. Mater. Sci. Technol.* **1999,** *15* (3), 193-197.
15. Gunawardana, P., Carbon formation phenomena and the initial stage of metal dusting corrosion–an experimental investigation. **2014**.
16. Betz, W., *High temperature alloys for gas turbines and other applications, 1986:: proceedings of a conference held in Liege, Belgium, 6-9 October 1986*. Springer Science & Business Media: 1987; Vol. 10567.
17. aesteironsteelpipes, http://aesteironsteelpipes.com/. **2019**.
18. Corporation, S. M. Inconel alloy 601. http://www.specialmetals.com/assets/smc/documents/alloys/inconel/inconel-alloy-601.pdf.
19. Klarstom, D. L.; Paul, L. D.; Grabke, H. J. In *The metal dusting behavior of several high temperature nickel based alloys*, CORROSION 2001, NACE International: 2001.
20. NISHIYAMA, Y.; MORIGUCHI, K.; OKADA, H.; OSUKI, T.; KURIHARA, S., Development of Metal Dusting Resistant Alloy for Synthesis Gas Production Plants. *NIPPON STEEL & SUMITOMO METAL TECHNICAL REPORT* **2015**.
21. Put, A. R.-V.; Unocic, K. A.; Brady, M. P.; Pint, B. A., Performance of chromia-and alumina-forming Fe-and Ni-base alloys exposed to metal dusting environments: The effect of water vapor and temperature. *Corros. Sci.* **2015,** *92*, 58-68.

22. Stahl, H.; Smith, G.; Wastiaux, S., Strain-age cracking of alloy 601 tubes at 600° C. *Practical failure analysis* **2001,** *1* (1), 51-54.
23. Toh, C. H.; Munroe, P. R.; Young, D. J.; Foger, K., High temperature carbon corrosion in solid oxide fuel cells. *Mater. High Temp.* **2003,** *20* (2), 129-136.
24. Mulaudzi, F.; Cornish, L.; Slabbert, G.; Papo, M.; Zhang, J., A study of metal dusting corrosion on Fe-and Ni-based alloys. *Journal of the Southern African Institute of Mining and Metallurgy* **2013,** *113* (2), 121-128.
25. Chun, C. M.; Ramanarayanan, T. A., Metal dusting resistant alumina forming coatings for syngas production. *Corros. Sci.* **2009,** *51* (11), 2770-2776.
26. Nishiyama, Y.; Okada, H.; Osuki, T.; Kurihara, S.; Ogawa, H. In *Improved metal dusting resistance of new sumitomo 696 ni-base alloy for synthesis gas environments*, Nitrogen+ Syngas 2011 International Conference, 2011; pp 129-138.
27. Walmsley, J. C.; Albertsen, J. Z.; Friis, J.; Mathiesen, R. H., The evolution and oxidation of carbides in an Alloy 601 exposed to long term high temperature corrosion conditions. *Corros. Sci.* **2010,** *52* (12), 4001-4010.
28. Gunawardana, P.; Venvik, H.; Walmsley, J. In *Investigation of the initial stage of metal dusting corrosion in the conversion of natural gas to synthesis gas*, CORROSION 2013, NACE International: 2013.
29. Gunawardana, P.; Walmsley, J.; Holmen, A.; Chen, D.; Venvik, H. J., Metal dusting corrosion initiation in conversion of natural gas to synthesis gas. *Energy Procedia* **2012,** *26*, 125-134.
30. Gunawardana, P. D. S.; Nguyen, T. T. M.; Walmsley, J. C.; Venvik, H. J., Initiation of metal dusting corrosion in conversion of natural gas to syngas studied under industrially relevant conditions. *Industrial & Engineering Chemistry Research* **2013,** *53* (5), 1794-1803.
31. Corporation, S. M. Incoloy alloy 800. http://www.specialmetals.com/assets/smc/documents/alloys/incoloy/incoloy-alloy-800.pdf.
32. Leistikow, S.; Wolf, I.; Grabke, H. J. M.; Corrosion, Effects of cold work on the oxidation behavior and carburization resistance of Alloy 800. **1987,** *38* (10), 556-562.
33. Grabke, H.; Schütze, M., *Corrosion by Carbon and Nitrogen: Metal Dusting, Carburisation and Nitridation*. Elsevier: 2014; Vol. 41.
34. Zhang, J.; Young, D. J., Coking and dusting of Fe–Ni alloys in CO–H2–H2O gas mixtures. *Oxid. Met.* **2008,** *70* (3-4), 189-211.
35. Grabke, H.; Krajak, R.; Müller-Lorenz, E.; Strauß, S., Metal dusting of nickel-base alloys. *Mater. Corros.* **1996,** *47* (9), 495-504.
36. Grabke, H. J.; Müller-Lorenz, E. M.; Eltester, B.; Lucas, M.; Monceau, D., Resistance of 9−20% Cr-steels against metal dusting. *steel research international* **1997,** *68* (4), 179-185.
37. Strauß, S.; Krajak, R.; Grabke, H., Coking by metal dusting of nickel-base alloys. *Mater. Corros.* **1999,** *50* (11), 622-627.
38. Hochman, R., The fundamentals of metal dusting. *API Division of Refining Proc.* **1966,** *46*, 331.
39. Grabke, H.; Krajak, R.; Müller-Lorenz, E., Metal dusting of high temperature alloys. *Mater. Corros.* **1993,** *44* (3), 89-97.
40. Chun, C.; Ramanarayanan, T.; Mumford, J., Relationship between coking and metal dusting. *Mater. Corros.* **1999,** *50* (11), 634-639.
41. Szakalos, P.; Pettersson, R.; Hertzman, S., An active corrosion mechanism for metal dusting on 304L stainless steel. *Corros. Sci.* **2002,** *44* (10), 2253-2270.
42. Helveg, S.; López-Cartes, C.; Sehested, J.; Hansen, P. L., Atomic-scale imaging of carbon nanofibre growth. *Nature* **2004,** *427* (6973), 426.

43. Jones, G.; Jakobsen, J. G.; Shim, S. S.; Kleis, J.; Andersson, M. P.; Rossmeisl, J.; Abild-Pedersen, F.; Bligaard, T.; Helveg, S.; Hinnemann, B., First principles calculations and experimental insight into methane steam reforming over transition metal catalysts. *J. Catal.* **2008,** *259* (1), 147-160.
44. Sperle, T.; Chen, D.; Lødeng, R.; Holmen, A., Pre-reforming of natural gas on a Ni catalyst: criteria for carbon free operation. *Applied Catalysis A: General* **2005,** *282* (1-2), 195-204.
45. Chen, D.; Lødeng, R.; Omdahl, K.; Anundskås, A.; Olsvik, O.; Holmen, A., A model for reforming on Ni catalyst with carbon formation and deactivation. In *Stud. Surf. Sci. Catal.*, Elsevier: 2001; Vol. 139, pp 93-100.
46. Kunadian, I.; Andrews, R.; Qian, D.; Mengüç, M. P., Growth kinetics of MWCNTs synthesized by a continuous-feed CVD method. *Carbon* **2009,** *47* (2), 384-395.
47. Yamada, T.; Namai, T.; Hata, K.; Futaba, D. N.; Mizuno, K.; Fan, J.; Yudasaka, M.; Yumura, M.; Iijima, S., Size-selective growth of double-walled carbon nanotube forests from engineered iron catalysts. *Nature nanotechnology* **2006,** *1* (2), 131.
48. Xiang, R.; Luo, G.; Qian, W.; Zhang, Q.; Wang, Y.; Wei, F.; Li, Q.; Cao, A., Encapsulation, compensation, and substitution of catalyst particles during continuous growth of carbon nanotubes. *Adv. Mater.* **2007,** *19* (17), 2360-2363.
49. Li, X.; Cao, A.; Jung, Y. J.; Vajtai, R.; Ajayan, P. M., Bottom-up growth of carbon nanotube multilayers: unprecedented growth. *Nano Lett.* **2005,** *5* (10), 1997-2000.
50. Lee, Y. H.; Kim, S. G.; Tománek, D., Catalytic growth of single-wall carbon nanotubes: an ab initio study. *Phys. Rev. Lett.* **1997,** *78* (12), 2393.
51. Maiti, A.; Brabec, C.; Bernholc, J., Kinetics of metal-catalyzed growth of single-walled carbon nanotubes. *Physical Review B* **1997,** *55* (10), R6097.
52. Bathgate, G.; Iyuke, S.; Kavishe, F., Comparison of Straight and Helical Nanotube Production in a Swirled Fluid CVD Reactor. *ISRN Nanotechnology* **2012,** *2012*.
53. XU, X., Metal Dusting--recent progress and industrial experience. *www.corrosionguru.com* **2017**.
54. Agüero, A.; Gutiérrez, M.; Korcakova, L.; Nguyen, T. T. M.; Hinnemann, B.; Saadi, S., Metal Dusting Protective Coatings. A Literature Review. *Oxid. Met.* **2011,** *76* (1-2), 23-42.
55. Tortorelli, P. F.; DeVan, H.; Judkins, R. R. *Carbon formation and metal dusting in hot-gas cleanup systems of coal gasifiers*; Oak Ridge National Lab., TN (United States): 1995.
56. Szakálos, P. Mechanisms of metal dusting. KTH, 2004.
57. Chun, C.; Ramanarayanan, T. A., Mechanism and control of carbon deposition on high temperature alloys. *J. Electrochem. Soc.* **2007,** *154* (9), C465-C471.
58. Viklund, P.; Norling, R., Cyclic long-term testing of gas turbine burner materials in reducing environments at 700 °C. *Mater. Corros.* **2014,** *65* (2), 169-177.
59. Fang, S.; Brinkman, K. S.; Chen, F., Hydrogen permeability and chemical stability of Ni–BaZr0.1Ce0.7Y0.1Yb0.1O3−δ membrane in concentrated H2O and CO2. *Journal of Membrane Science* **2014,** *467*, 85-92.
60. De Bruyn, H. J.; Edwin, E. H.; Brendryen, S. In *Apparent influence of steam on metal dusting*, CORROSION 2001, NACE International: 2001.
61. Grabke, H.; Muller-Lorenz, E.; Strauss, S.; Pippel, E.; Woltersdorf, J., Effects of grain size, cold working, and surface finish on the metal-dusting resistance of steels. *Oxid. Met.* **1998,** *50* (3), 241-254.
62. Zeng, Z.; Natesan, K., Relationship between the growth of carbon nanofilaments and metal dusting corrosion. *Chem. Mater.* **2005,** *17* (14), 3794-3801.
63. Albertsen, J. Z., Experimental and theoretical investigations of metal dusting corrosion in plant exposed nickel-based alloys. **2007**.

64. Albertsen, J. Z.; Grong, Ø.; Walmsley, J. C.; Mathiesen, R. H.; Van Beek, W., A Model for High-Temperature Pitting Corrosion in Nickel-Based Alloys Involving Internal Precipitation of Carbides, Oxides, and Graphite. *Metallurgical and Materials Transactions A* **2008,** *39* (6), 1258-1276.
65. Albertsen, J.; Grong, Ø.; Mathiesen, R.; Schmid, B., Metallurgical investigation of metal dusting corrosion in plant-exposed nickel-based alloy 602CA. *Corrosion engineering, science and technology* **2005,** *40* (3), 239-243.
66. Szakálos, P., Mechanisms and driving forces of metal dusting. *Mater. Corros.* **2003,** *54* (10), 752-762.
67. Szakálos, P.; Lundberg, M.; Pettersson, R., Metal dusting on an alumina forming Ni-base alloy. *Corros. Sci.* **2006,** *48* (7), 1679-1695.
68. Chun, C.; Ramanarayanan, T., Corrosion resistance of a high-silicon alloy in metal-dusting environments. *Oxid. Met.* **2007,** *67* (3-4), 215-234.
69. Pippel, E.; Woltersdorf, J.; Schneider, R., Micromechanisms of metal dusting on Fe-base and Ni-base alloys. *Mater. Corros.* **1998,** *49* (5), 309-316.
70. Pippel, E.; Woltersdorf, J.; Grabke, H., Microprocesses of metal dusting on iron-nickel alloys and their dependence on the alloy composition. *Mater. Corros.* **2003,** *54* (10), 747-751.
71. Fabas, A.; Monceau, D.; Josse, C.; Lamesle, P.; Rouaix-Vande Put, A., Mechanism of metal dusting corrosion by pitting of a chromia-forming alloy at atmospheric pressure and low gas velocity. *Corros. Sci.* **2016,** *107*, 204-210.
72. Szkodo, M.; Gajowiec, G., Studies of the mechanism of metal dusting of 10CrMo9-10 steel after 10 years of operation in the semi-regenerative catalytic reformer. *Corros. Sci.* **2016,** *102*, 279-290.
73. Fabas, A.; Monceau, D.; Doublet, S.; Put, A. R.-V., Modelling of the kinetics of pitting corrosion by metal dusting. *Corros. Sci.* **2015,** *98*, 592-604.
74. Camperos Guevara, S. H. Statistical lifetime modeling of FeNiCr alloys for high temperature corrosion in waste to energy plants and metal dusting in syngas production plants. 2016.
75. Yang, X.; Mai, Y.-W., J-integral for spallation of protective layer subjected to metal dusting corrosion. *Materials & Design* **2017,** *119*, 263-269.
76. Bentria, E. T.; N'Tsouaglo, G. K.; Becquart, C. S.; Bouhali, O.; Mousseau, N.; El-Mellouhi, F., The role of emerging grain boundary at iron surface, temperature and hydrogen on metal dusting initiation. *Acta Mater.* **2017,** *135*, 340-347.
77. Chakrabarty, A.; Bentria, E. T.; Omotayo, S. A.; Bouhali, O.; Mousseau, N.; Becquart, C. S.; El Mellouhi, F., Elucidating the role of extended surface defects at Fe surfaces on CO adsorption and dissociation. *Appl. Surf. Sci.* **2019,** *491*, 792-798.
78. Madloch, S.; Dorcheh, A.; Galetz, M., Effect of Pressure on Metal Dusting Initiation on Alloy 800H and Alloy 600 in CO-rich Syngas. *Oxid. Met.* **2018,** *89* (3-4), 483-498.
79. Hattendorf, H.; Hermse, C. G. M.; Ijzerman, R. M., The influence of alloying elements on metal dusting behavior of nickel chromium alloys and their statistical correlation. *Mater. Corros.* **2019,** *70* (8), 1385-1399.
80. Fabas, A.; Put, A. R.-V.; Doublet, S.; Domergue, D.; Salem, M.; Monceau, D., Metal dusting corrosion of austenitic alloys at low and high pressure with the effects of Cr, Al, Nb and Cu. *Corros. Sci.* **2017**.
81. Vaché, N.; Cazottes, S.; Douillard, T.; Duret-Thual, C.; Dupoiron, F.; Augustin, C.; Steyer, P. J. O. o. M., Origin of Nickel Catalytic Particles in Carbon Nanotube Formation on a High-Carbon 25Cr–35Ni–Nb Cast Alloy. **2019,** *91* (3-4), 279-290.
82. Sridhar, D.; Omanovic, S.; Meunier, J.-L., Direct growth of carbon nanofiber forest on nickel foam without any external catalyst. *Diamond Relat. Mater.* **2018,** *81*, 70-76.

83. Rajendran Pillai, S., Thermal cycling of sodium system and possibility of metal dusting: an analysis. *Mater. High Temp.* **2014,** *28* (1), 12-16.
84. Sun, X.; Ma, H. T.; Yang, L. Z.; Sanchez-Pasten, M.; Craig Penner, D.; Li, Y. S.; Yang, Q., Metal dusting, carburization and diamond deposition on Fe–Cr alloys in CH4–H2 plasma atmospheres. *Corros. Sci.* **2015,** *98*, 619-625.
85. Li, X. J.; He, L. L.; Li, Y. S.; Yang, Q., Catalytic graphite mechanism during CVD diamond film on iron and cobalt alloys in CH4-H2 atmospheres. *Surf. Coat. Technol.* **2019,** *360*, 20-28.
86. Orlikowski, J.; Jazdzewska, A.; Darowicki, K.; Karczewski, J.; Dampc, J., Metal dusting phenomena of 501 AISI furnace tubes in refinery fractional distillation unit. *Engineering Failure Analysis* **2018,** *91*, 108-114.
87. L'vov, S. G.; Kukovitsky, E. F.; Shustov, V. A.; Lyadov, N. M., Formation of Carbon-Nanotube Layers on Bulk Nickel: The Effect of Surface Topography Defects. *Journal of Surface Investigation: X-ray, Synchrotron and Neutron Techniques* **2019,** *13* (3), 400-407.
88. Ramezanipour, F.; Singh, A.; Paulson, S.; Farag, H.; Birss, V. I.; Thangadurai, V., Carbon formation on stainless steel 304H in convection section of ethane cracking plant. *Corrosion Engineering, Science and Technology* **2014,** *50* (4), 303-310.
89. Singh, A.; Paulson, S.; Farag, H.; Birss, V.; Thangadurai, V., Role of Presulfidation and H2S Cofeeding on Carbon Formation on SS304 Alloy during the Ethane–Steam Cracking Process at 700° C. *Industrial & Engineering Chemistry Research* **2018**.
90. Melo-Máximo, L.; Pérez, M.; Lin, J.; Salas, O.; Melo-Máximo, D.; Oseguera, J.; López-Hirata, V. M.; Torres, R. D.; Souza, R. M., Performance of MPPMS Cr/Cr2O3films in protection against metal dusting. *Surf. Eng.* **2014,** *31* (2), 166-172.
91. Eugene Medvedovski, J. M., Xiaoyang Guo, Estelle Vanhaecke and Hilde Venvik, Studies of Corrosion Resistance of Aluminized Coatings in Metal Dusting Environments. In *Materials Science & Technology 2017*, 2017.
92. Li, M.; Zhu, Y.; Zhou, C., Effect of yttrium on the coking behavior of Fe-based superalloy in heavy hydrocarbon. *Corros. Sci.* **2015,** *98*, 81-87.
93. Ding, R.; Taylor, M.; Chiu, Y.-L.; Smith, N.; Mowforth, C.; Evans, H. J. O. o. M., Influence of Pre-oxidation on Filamentary Carbon Deposition on 20Cr25Ni Stainless Steel. **2019**, 1-19.
94. Ryan, M. P.; Williams, D. E.; Chater, R. J.; Hutton, B. M.; McPhail, D. S., Why stainless steel corrodes. *Nature* **2002,** *415* (6873), 770-774.
95. Lobnig, R.; Schmidt, H.; Hennesen, K.; Grabke, H., Diffusion of cations in chromia layers grown on iron-base alloys. *Oxid. Met.* **1992,** *37* (1-2), 81-93.
96. Zeng, Z.; Natesan, K.; Grimsditch, M., Effect of oxide scale compositions on metal dusting corrosion of Fe-based alloys. *Corrosion* **2004,** *60* (7), 632-642.
97. Strauss, S.; Grabke, H., Role of alloying elements in steels on metal dusting. *Mater. Corros.* **1998,** *49* (5), 321-327.
98. Rosado, C.; Schütze, M., Protective behaviour of newly developed coatings against metal dusting. *Mater. Corros.* **2003,** *54* (11), 831-853.
99. Wolf, I.; Grabke, H., A study on the solubility and distribution of carbon in oxides. *Solid State Commun.* **1985,** *54* (1), 5-10.
100. Toh, C.; Munroe, P.; Young, D., Metal dusting of Fe–Cr and Fe–Ni–Cr alloys under cyclic conditions. *Oxid. Met.* **2002,** *58* (1-2), 1-21.
101. Finger, L. W.; Hazen, R. M. J. J. o. A. P., Crystal structure and isothermal compression of Fe2O3, Cr2O3, and V2O3 to 50 kbars. **1980,** *51* (10), 5362-5367.
102. Edwards, M. W.; McIntyre, N. S., Gas Phase Initial Oxidation of Incoloy 800 Surfaces. *Oxid. Met.* **2013,** *79* (1-2), 179-200.

103. Essuman, E.; Meier, G.; Żurek, J.; Hänsel, M.; Quadakkers, W., The effect of water vapor on selective oxidation of Fe–Cr alloys. *Oxid. Met.* **2008,** *69* (3-4), 143-162.
104. Zeng, Z.; Natesan, K., Initiation of Metal-Dusting Pits and a Method to Mitigate Metal-Dusting Corrosion. *Oxid. Met.* **2006,** *66* (1-2), 1-20.
105. Wilson, P.; Chen, Z. J. C. s., The effect of manganese and chromium on surface oxidation products formed during batch annealing of low carbon steel strip. **2007,** *49* (3), 1305-1320.
106. Li, H.; Chen, W., High temperature carburization behaviour of Mn–Cr–O spinel oxides with varied concentrations of manganese. *Corros. Sci.* **2011,** *53* (6), 2097-2105.
107. Li, H.; Chen, W., Stability of MnCr2O4 spinel and Cr2O3 in high temperature carbonaceous environments with varied oxygen partial pressures. *Corros. Sci.* **2010,** *52* (7), 2481-2488.
108. Li, H.; Zheng, Y.; Benum, L. W.; Oballa, M.; Chen, W., Carburization behaviour of Mn–Cr–O spinel in high temperature hydrocarbon cracking environment. *Corros. Sci.* **2009,** *51* (10), 2336-2341.
109. Ramanarayanan, T. A.; Chun, C., Metal dusting resistant alloys. Google Patents: 2004.
110. Bao, B.; Liu, J.; Xu, H.; Liu, B.; Zhang, W., Inhibitory effect of MnCr 2 O 4 spinel coating on coke formation during light naphtha thermal cracking. *RSC Advances* **2016,** *6* (73), 68934-68941.
111. Kus, E.; Lee, Z.; Nutt, S.; Mansfeld, F., A comparison of the corrosion behavior of nanocrystalline and conventional Al 5083 samples. *Corrosion* **2006,** *62* (2), 152-161.
112. Ralston, K.; Birbilis, N., Effect of grain size on corrosion: a review. *Corrosion* **2010,** *66* (7), 075005-075005-13.
113. Tsuji, N.; Saito, Y.; Lee, S. H.; Minamino, Y., ARB (Accumulative Roll-Bonding) and other new techniques to produce bulk ultrafine grained materials. *Adv. Eng. Mater.* **2003,** *5* (5), 338-344.
114. Saito, Y.; Utsunomiya, H.; Tsuji, N.; Sakai, T., Novel ultra-high straining process for bulk materials—development of the accumulative roll-bonding (ARB) process. *Acta Mater.* **1999,** *47* (2), 579-583.
115. Tsuji, N.; Ito, Y.; Saito, Y.; Minamino, Y., Strength and ductility of ultrafine grained aluminum and iron produced by ARB and annealing. *Scripta Mater.* **2002,** *47* (12), 893-899.
116. Liu, G.; Lu, J.; Lu, K., Surface nanocrystallization of 316L stainless steel induced by ultrasonic shot peening. *Materials Science and Engineering: A* **2000,** *286* (1), 91-95.
117. Wang, Z.; Tao, N.; Li, S.-s.; Wang, W.; Liu, G.; Lu, J.; Lu, K., Effect of surface nanocrystallization on friction and wear properties in low carbon steel. *Materials Science and Engineering: A* **2003,** *352* (1-2), 144-149.
118. Liu, G.; Wang, S.; Lou, X.; Lu, J.; Lu, K., Low carbon steel with nanostructured surface layer induced by high-energy shot peening. *Scripta Mater.* **2001,** *44* (8-9), 1791-1795.
119. Tian, J.; Shaw, L.; Liaw, P.; Dai, K., On the ductility of a surface severely plastically deformed nickel alloy. *Materials Science and Engineering: A* **2008,** *498* (1-2), 216-224.
120. Villegas, J.; Shaw, L.; Dai, K.; Yuan, W.; Tian, J.; Liaw, P.; Klarstrom, D., Enhanced fatigue resistance of a nickel-based hastelloy induced by a surface nanocrystallization and hardening process. *Philos. Mag. Lett.* **2005,** *85* (8), 427-438.
121. Dai, K.; Shaw, L., Analysis of fatigue resistance improvements via surface severe plastic deformation. *Int. J. Fatigue* **2008,** *30* (8), 1398-1408.
122. Sato, M.; Tsuji, N.; Minamino, Y.; Koizumi, Y., Formation of nanocrystalline surface layers in various metallic materials by near surface severe plastic deformation. *Science and Technology of Advanced Materials* **2004,** *5* (1), 145-152.
123. Villegas, J.; Shaw, L., Nanocrystallization process and mechanism in a nickel alloy subjected to surface severe plastic deformation. *Acta Mater.* **2009,** *57* (19), 5782-5795.

124. Gupta, R.; Birbilis, N., The influence of nanocrystalline structure and processing route on corrosion of stainless steel: A review. *Corros. Sci.* **2015,** *92*, 1-15.
125. Gleiter, H., Nanostructured materials: basic concepts and microstructure. *Acta Mater.* **2000,** *48* (1), 1-29.
126. Palumbo, G.; Thorpe, S.; Aust, K., On the contribution of triple junctions to the structure and properties of nanocrystalline materials. *Scripta metallurgica et materialia* **1990,** *24* (7), 1347-1350.
127. Liu, L.; Li, Y.; Wang, F., Electrochemical corrosion behavior of nanocrystalline materials—a review. *Journal of Materials Science & Technology* **2010,** *26* (1), 1-14.
128. Wang, Z.; Tao, N.; Tong, W.; Lu, J.; Lu, K., Diffusion of chromium in nanocrystalline iron produced by means of surface mechanical attrition treatment. *Acta Mater.* **2003,** *51* (14), 4319-4329.
129. Zhu, R.; Lu, B.; Luo, J.; Lu, Y., Effect of cold work on surface reactivity and nano-hardness of alloy 800 in corroding environments. *Appl. Surf. Sci.* **2013,** *270*, 755-762.
130. Tan, L.; Ren, X.; Sridharan, K.; Allen, T., Effect of shot-peening on the oxidation of alloy 800H exposed to supercritical water and cyclic oxidation. *Corros. Sci.* **2008,** *50* (7), 2040-2046.
131. Lin, C.-Y.; Chang, C.-H.; Tsai, W.-T., Morphological and microstructural aspects of metal dusting on 304L stainless steel with different surface treatments. *Oxid. Met.* **2004,** *62* (3), 153-174.
132. Chun, C.; Ramanarayanan, T., Metal dusting corrosion of austenitic 304 stainless steel. *J. Electrochem. Soc.* **2005,** *152* (5), B169-B177.
133. Voisey, K.; Liu, Z.; Stott, F., Inhibition of metal dusting of Alloy 800H by laser surface melting. *Appl. Surf. Sci.* **2006,** *252* (10), 3658-3666.
134. Baker, B. A.; Smith, G. D.; Hartmann, V.; Shoemaker, L. E.; McCoy, S., Nickel-base material solutions to metal dusting problems. *Special Metals Corporation, USA and Special Metals Wiggin Ltd UK* **2002**.
135. Mertz, J., *Introduction to optical microscopy*. Cambridge University Press: 2019.
136. Reimer, L., *Scanning electron microscopy: physics of image formation and microanalysis*. Springer: 2013; Vol. 45.
137. Reimer, L., *Transmission electron microscopy: physics of image formation and microanalysis*. Springer: 2013; Vol. 36.
138. Garratt-Reed, A. J.; Bell, D. C., *Energy dispersive X-ray analysis in the electron microscope*. Bios: 2003.
139. Tousimis, A.; Marton, L., *Electron probe microanalysis*. Elsevier: 2013; Vol. 6.
140. Guinier, A., *X-ray diffraction in crystals, imperfect crystals, and amorphous bodies*. Courier Corporation: 1994.
141. Wolstenholme, J., *Auger electron spectroscopy: practical application to materials analysis and characterization of surfaces, interfaces, and thin films*. Momentum Press: 2015.
142. Yao, N., *Focused ion beam systems: basics and applications*. Cambridge University Press: 2007.
143. Ferraro, J. R., *Introductory raman spectroscopy*. Elsevier: 2003.
144. Schrader, B., *Infrared and Raman spectroscopy: methods and applications*. John Wiley & Sons: 2008.
145. Paul, A.; Kaimal, K.; Naik, M.; Dharwadkar, S., Lattice and grain boundary diffusion of chromium in superalloy Incoloy-800. *J. Nucl. Mater.* **1994,** *217* (1-2), 75-81.
146. Persaud, S.; Ramamurthy, S.; Korinek, A.; Botton, G.; Newman, R., The influence of the high Fe and Cr contents of Alloy 800 on its inter-and intragranular oxidation tendency in 480° C hydrogenated steam. *Corros. Sci.* **2016,** *106*, 117-126.

147. Luan, T.-C.; Eckert, R. E.; Albright, L. F., Gaseous pretreatment of high-alloy steels used in ethylene furnaces: Pretreatment of Incoloy 800. *Industrial & engineering chemistry research* **2003,** *42* (20), 4741-4747.
148. Fulger, M.; Ohai, D.; Mihalache, M.; Pantiru, M.; Malinovschi, V., Oxidation behavior of Incoloy 800 under simulated supercritical water conditions. *J. Nucl. Mater.* **2009,** *385* (2), 288-293.

Appendix

Paper I

Effects of metal dusting relevant exposures of alloy 601 surfaces on carbon formation and oxide development

Xiaoyang Guo, Estelle Vanhaecke, Per Erik Vullum, Jianyu Ma, P. V. D. S. Gunawardana, John C. Walmsley, De Chen, Hilde J. Venvik

Catalysis Today xxx (xxxx) xxx–xxx

Contents lists available at ScienceDirect

Catalysis Today

journal homepage: www.elsevier.com/locate/cattod

Effects of metal dusting relevant exposures of alloy 601 surfaces on carbon formation and oxide development

Xiaoyang Guo[a], Estelle Vanhaecke[a], Per Erik Vullum[b], Jianyu Ma[a], P.V. Daham S. Gunawardana[a,1], John C. Walmsley[b,2], De Chen[a], Hilde J. Venvik[a,*]

[a] Department of Chemical Engineering, NTNU - Norwegian University of Science and Technology, Trondheim, 7491, Norway
[b] SINTEF Industry, Trondheim, 7465, Norway

ARTICLE INFO

Keywords:
carbon formation
metal dusting
synthesis gas alloy 601
chromium oxide
spinel

ABSTRACT

Ni and Fe are excellent catalysts for carbon formation, and industrial alloys are therefore susceptible to metal dusting corrosion; a costly issue in e.g. synthesis gas manufacture. The objective of this work is to better understand the initial reaction phenomena leading to metal dusting, and thereby minimize the corrosion through optimum alloy selection and pretreatment. Pre-oxidized alloy 601 samples were subjected to carburizing gaseous environments at 750 °C, and carbon formation and surface oxide layer development were investigated by SEM, optical microscopy, AES and Raman spectroscopy. Thin (S)TEM/EDS cross-section lamellae were prepared by Focussed Ion Beam milling.

Beyond the initial incubation period, less carbon is formed under 10% CO/Ar than under synthesis gas with finite low carbon activity. Cr_2O_3 evolves as a thin surface oxide layer with only CO reacting and more ordered carbon develops with increasing exposure time. In contrast, oxidation yields (Ni, Fe, Cr)$_3O_4$ spinel formation while the materializing carbon remains its disorder during prolonged exposure to synthesis gas. The metal dusting corrosion rate is hence lowered due to Cr_2O_3 stabilization, while the spinel represents an unstable redox state that continuously yields new carbon. A fine-grained alloy surface structure is also found beneficial to the Cr_2O_3 formation.

1. Introduction

Fe, Ni and Co are known as catalysts for producing carbon nanotubes and carbon nanofibers due to their ability to activate gaseous carbon-containing molecules to form carbon-carbon bonds. In the petrochemical industries, metals and alloys are typically exposed to carbon-saturated gaseous environments with low partial pressures of oxygen and/or steam in a critical temperature range of 400–900 °C [1–4]. Fe and Ni are also main constituent elements of common industrial alloys with desirable high temperature stability. Equipment based on these alloys is therefore susceptible to so-called metal dusting corrosion; a detrimental degradation phenomenon that proceeds by a gradual breakdown of the material into a powdery mixture of graphite, carbide and metal particles. Metal dusting carries significant cost, since considerable measures need to be implemented in order to avoid catastrophic events in the industrial operation.

One of the measures that are being applied to prevent metal dusting (as well as other) corrosion is the incorporation of chromium (Cr) in the alloy to facilitate the formation of a Cr oxide at the surface. Cr_2O_3 is known as impermeable to carbon and remains stable in carbonaceous and reducing atmospheres down to very low oxygen partial pressure [5]. Surface layers of Cr_2O_3 are excellent in preventing alloys from metal dusting corrosion [6,7] provided a dense and defect free oxide layer that prohibits access to the bulk matrix can be formed and maintained during industrial operation. Manganese (Mn) is another alloying element in high temperature alloys, known to suppress the hot working brittleness. High mobility of Mn in Cr_2O_3 [8] enables formation of a $CrMn_2O_4$ spinel phase, and this spinel is also established as a good protective scale [9–13].

The phenomenon of metal dusting has been studied for decades [4,14–20]. Metal dusting of Fe-based alloys has been shown to involve metastable Fe_3C formation and the subsequent decomposition [18,21] and/or disintegration [7,22] of this compound. The resulting nanoparticles serve as catalysts for further carbon deposition. It should be

* Corresponding author.
E-mail address: hilde.j.venvik@ntnu.no (H.J. Venvik).
[1] Present address: Yara International ASA, Hydrovegen 67, 3936 Porsgrunn, Norway.
[2] Present address: Department of Materials Science and Metallurgy, University of Cambridge, 27 Charles Babbage Road, Cambridge CB3 0FS, United Kingdom.

https://doi.org/10.1016/j.cattod.2020.04.029
Received 15 October 2019; Received in revised form 30 March 2020; Accepted 6 April 2020

noted that Ni-based alloys show better metal dusting corrosion resistance compared to Fe-based alloys. There are several reasons for this difference. Cr atoms diffuse relatively fast within the alloy and the amount of Cr increases with the Ni content [23]. Unlike Fe-based alloys, Ni-based alloys do not form metastable M_3C (M = metal) intermediates during the carburization [24]. The carbon permeability is lower in Ni-based alloys compared to Fe-based alloys [16,18,25,26]. Finally, fewer and larger metal particles are formed during the metal dusting process on Ni-based alloys compared to on Fe-based alloys, thereby lowering the total catalytic surface area for carbon formation [16,27]. Once graphite has formed, Ni atoms may diffuse via intercalation to form nanoparticles that catalyze further carbon deposition [17].

Ni-based Inconel 601 generally displays resistance against corrosion under oxidizing and reducing conditions at high temperature [20,28–39]. Inconel 601 is thus widely used in petrochemical and other process equipment, and several investigations have addressed its susceptibility to metal dusting. Klarstrom et al. have exposed Inconel 601 to a flowing gas mixture for 10,000 hours to find significant metal wastage in the form of numerous rounded pits with diameter up to 1.2 mm. [28]. Walmsley et al. have studied the basic features of carburization and carbide oxidation of Inconel 601 alloy exposed to metal dusting conditions for 2 years in a commercial methanol plant [37]. Nishiyama et al. compared alloy 601 to their own NSSMC 696 alloy under synthesis gas for more than 10,000 hours and concluded that the pits observed occur earlier and grow faster on 601 [29]. Many of these studies have been based on the analysis of long-term exposed material (both in laboratory and in industrial plant), however, the mechanism of the initial carbon formation on the metal dusting relevant alloy surface is less described, documented and understood.

The overall objective of our research is to provide a better general understanding and prediction of carbon formation phenomena leading to metal dusting, as well as enabling alloy selection and alloy pretreatment protocols that minimize metal dusting corrosion. We have previously demonstrated in a qualitative way that the tendency to form solid carbon on the Inconel 601 surface is strongly linked to the pre-oxidation conditions, through the composition and structure of the Cr-rich oxide layer formed [20,38,39]. The carbon formation was catalyzed by Fe and/or Ni (alloy) particles, seemingly originating from the reducible phases presence within this layer [20]. Moreover, we exposed the Inconel 601 to a model syngas at varying temperature to show that pitting features, observed in alloys applied in industrial process equipment, could be formed within relatively short exposures [20]. In this study, by varying the exposure time, we assess the point at which the reducible phases are initiating the first carbon formation as well as how the carbon formation progresses during the initial phase. CO is the main source of carbon, but the effects of adding common synthesis gas components (H_2, CO_2 and H_2O) are also addressed. Characterization by SEM, XRD, Raman and TEM, the latter involving advanced sample preparation by Focused Ion Beam (FIB) milling and EDS/EELS elemental analysis, are combined to yield information on the amount and type of carbon evolving, the nature of the catalyst particles associated with the formation of carbon, the composition and topology of the oxide phases developing at and near the surface during exposure, and finally the characteristics of the initial pitting.

2. Materials and methods

Inconel 601 alloy samples with dimension 15 × 8 × 0.5 mm^3 were cut and first subjected to a procedure intended to yield a consistent and bulk representative starting point. Gradually finer polishing was applied until reaching 1 μm diamond grain size, then ultrasonic cleaning in 99% hexane for 30 min and drying overnight. Oxidation and carburization exposures were thereafter conducted in an experimental setup described elsewhere with a vertical, internally gold-coated, steel tube (Incoloy 800 H) enclosed in a furnace [40].

Oxidation of the alloy samples was performed by ramping the temperature by 10 °C/min in 10% steam in Ar to 540 °C, and then the samples were kept at 540 °C for 6 h at 1 bar. The resulting samples were either unloaded for characterization or exposed to carburizing conditions at 750 °C. Two different gas mixtures (100 Nml/min total flow rate) were used for the experiments; one representing infinite carbon activity ($a_c \gg 1$) and consisting of 10% CO in Ar at 1 bar (denoted as I-a_c), the other simulating syngas at industrially relevant conditions, i.e. finite low carbon activity ($a_c \sim 7$, denoted as FL-a_c), and containing a mixture of H_2 (25%), CO (20%), CO_2 (15%), H_2O (10%) and Ar (30%) at 20 bar total pressure [40]. The metal dusting exposure time varied from 1 h to 20 h. After oxidation/exposure, the samples were cooled under Ar flow and unloaded at ambient conditions.

The resulting samples were characterized by a range of techniques to relate the carbon formation propensity and potential progression of the metal dusting to the initial structure and composition, as well as the development of the metal/oxide matrix during the carburizing exposures. A Zeiss Ultra 55 LE thermal field emission gun scanning electron microscope (FEG-SEM) was operated at 10 kV. The depth profiles of Inconel 601 before and after oxidization were analyzed by Auger spectroscopy under Ar-ion sputtering in a field emission JEOL 9500 F instrument. The acceleration voltage of the electron beam was 10 keV and analysis was performed at 30° under Ar^+ of 1 keV. Raman spectra were collected by focusing a Horiba Jobin Yvon LabRAM HR800 spectrometer, using the emission line at 633 nm from a He-Ne laser, on the sample with a 50 × LWD objective with a motorized x-y stage. The output power of the laser was 8 mW with a spot diameter of approximately 1.5 μm. The spectra were recorded with continuous scans in the range 300-3000 cm^{-1}. Spectra were taken at three different locations on a given sample to verify that the observed surface characteristics were uniform and representative. Grazing incidence X-ray diffraction (XRD) was applied to investigate the near surface region of the samples using a Bruker D8 A25 DaVinci X-ray Diffractometer with Cu Kα radiation with a 1° incidence angle.

Finally, cross-section TEM lamellae were prepared from selected samples by a FEI Helios G4 UX focused ion beam (FIB). Carbon or platinum protection layers (the first part of the layer made by e-beam assisted deposition to avoid ion-beam induced surface damage) were deposited on the selected regions prior to cutting out the TEM lamella. Coarse thinning was performed at 30 kV acceleration voltage. The last part of the thinning was performed at 5 kV and finally 2 kV to minimize ion-beam induced surface damage on either side of the TEM lamellae. The TEM analysis was done on a double C_s aberration corrected cold FEG JEOL ARM 200 F, operated at 200 kV and equipped with a large solid angle Centurio SDD (0.98 sr) for X-ray energy dispersive spectroscopy (EDS) and a Quantum ER GIF for dual electron energy loss spectroscopy (EELS).

3. Results and Discussion

3.1. Initial structure and composition

The nature of the surface oxide layer, i.e. microstructure and composition as resulting from the initial polishing to uncover the bulk and subsequent oxidation in steam at elevated temperature, represents the starting point of this investigation. Fig. 1(a) shows a SEM micrograph of the oxide layer for the pre-oxidized alloy sample before exposure to the carburizing mixture. The parallel streaky features appearing on the alloy surface result from the polishing. Particle-like features can also be observed, and these were formed upon the steam exposure. The corresponding X-ray diffractogram (Fig. 1(b)), displays two strong diffraction peaks from the fcc bulk alloy matrix. Peaks representative of oxides are practically undetectable. The particles are seemingly also recognizable in the Raman optical microscope as the darker features of the image shown in Fig. 1(c). Raman spectroscopy was performed at the center of Fig. 1(c), with the result given in Fig. 1(d). The Raman bands at 358 cm^{-1}, 528 cm^{-1}, 555 cm^{-1}, 623 cm^{-1} correspond to Cr_2O_3 [41],

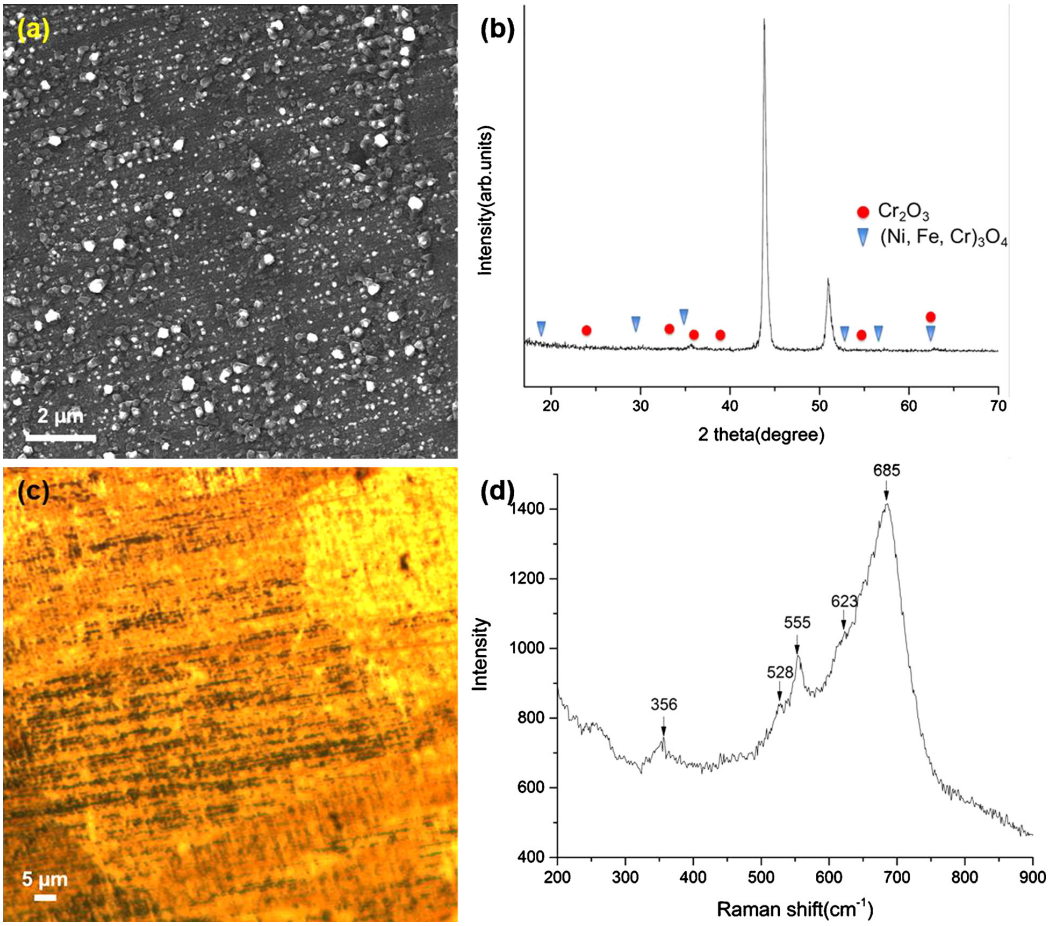

Fig. 1. Surface characterization of polished Inconel 601 sample after oxidation under 10% steam in Ar at 540 °C for 6 h at 1 bar; (a) SEM micrograph; (b) X-ray diffraction (c) Raman optical micrograph; (d) Raman spectroscopy.

while the peak at 685 cm^{-1} may be assigned to $(Ni, Fe, Cr)_3O_4$ spinel [35]. Spectra from other areas on the sample display similar characteristics.

Auger depth profiles of Inconel 601 before and after oxidization are shown in Fig. 2. It can be noted that the alloy samples also exhibit a very thin oxide layer before oxidization, with thickness ~2 nm, as a result of exposure to ambient conditions during sample transfer. The steam oxidation at 540 °C results in an oxygen rich region of 40-50 nm thickness. The sputtering rate may depend somewhat on the composition and structure of the material [39]. The obtained depth profiles thus provide semi-quantitative information, since the estimated depth refers to sputtering of a SiO_2 standard. The oxide layer estimate corresponds well, however, to thicknesses obtained from TEM cross section analysis of a similar sample (Shown in Fig. S1, Supporting Information), ranging locally from 30 nm to 90 nm. The O concentration decreases when moving from the surface to the bulk alloy matrix. Fig. 2(b) further indicates that the oxidized surface layer is depleted in, but not free from, Fe and Ni, in accordance with the Raman spectroscopy results (Fig. 1(d)). The amount of Cr relative to Ni and Fe is hence significantly higher than in the bulk.

Combined, the information from Raman spectroscopy and Auger depth profiling shows that a ~40 nm oxide scale has formed after oxidization in 10% steam in Ar. This scale is too thin to yield a significant X-ray diffraction signal, and contains Cr_2O_3 as well as $(Ni, Fe, Cr)_3O_4$ spinel.

3.2. Carbon formation

The pre-oxidized alloy samples were subjected to the carburizing gas mixtures at 750 °C as previously described. Carbon formed on the pre-oxidized alloy samples under 1 h to 20 h of infinite carbon activity (1 bar 10% CO in Ar; I-a_c) conditions is illustrated by the SEM micrographs in Fig. 3. Carbon filaments are found after all exposure times. With time, the number of filaments increases as well as the length and the diameter of each filament. The samples exposed for 1 h (Fig. 3(a and b)) display short carbon fibers with nanosized particles at the tip, which is typical of a Ni/Fe catalyzed carbon growth mode. When the exposure time is prolonged to 2 h (Fig. 3(c and d)) a wider range in filament length and diameter is observed. After 5 h exposure time (Fig. 3(e and f)), catalyst particles can be observed not only at the tip of the filaments, but also along the center axis. The twisted morphology of the carbon filaments may have originated from splitting of the catalyst particles. This shape of carbon filaments is more evident after 20 h exposure to the I-a_c conditions (Fig. 3(g and h)). The diameter of the carbon filaments at one end is larger while, as the growth proceeds, the filament diameter gradually decreases. Two different types of catalyst

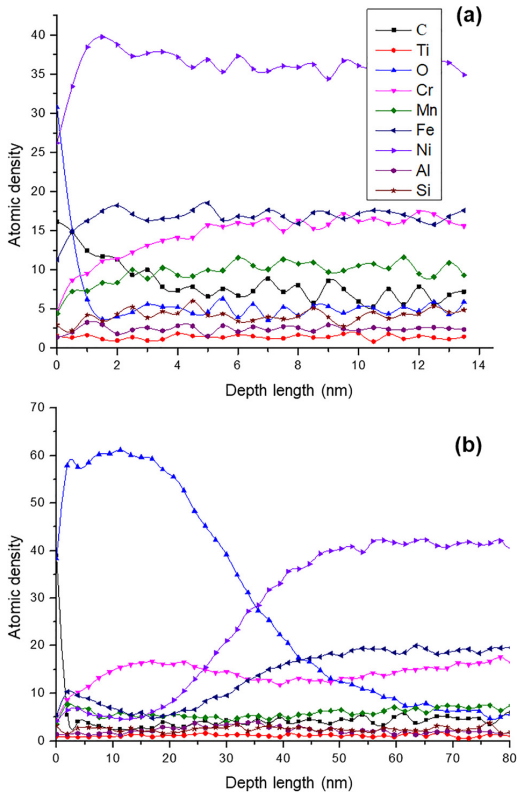

Fig. 2. Auger sputtering depth profiles of polished Inconel 601 surface (a) before oxidization and (b) after oxidization under 10% steam in Ar at 540 °C for 6 h at 1 bar.

particles were observed associated with these carbon filaments. One is a thin conical shaped nanorod encapsulated at the tip of carbon filaments. The other type includes relatively large, elongated particles encapsulated along the middle of the carbon filaments.

The carbon formation trends after exposures to finite, low carbon activity simulated syngas (20 bar 25% H_2, 20% CO, 15% CO_2, 10% H_2O and 30%Ar; FL-a_c) for 1-20 h are illustrated in Fig. 4. There are no observable carbon filaments after 1 h exposure (Fig. 4(a and b)). After 2 h, short (~100 nm) carbon filaments with catalyst particles at the tip are found (Fig. 4(c and d)). In Fig. 4(e and f), after 5 h exposure, the carbon filaments are significantly longer with diameters ranging from 100 - 400 nm and exhibiting a twisted and entangled morphology. After 20 h FL-a_c exposure, most of the surface is covered by filamentous carbon (Fig. 4(g and h)). Some few and small areas are not fully covered by carbon, but these do display short emerging carbon filaments. An example can be seen from the inset in Fig. 4(h), which contains two filaments of ~200 nm diameter and ~400 nm length, each with a catalyst particle at the tip. This demonstrates that the complete sample surface is attacked by carbon formation phenomena leading to metal dusting corrosion.

Our pre-oxidized Inconel 601 alloy hence shows different performance regarding carbon deposition under the different conditions at 750 °C. First, the carbon filaments formed under FL-a_c at 20 bar were usually larger in diameter than those formed under I-a_c at 1 bar. This is in accordance with observations reported by Zeng and Natesan [42]. Then there appears to be less carbon within 2 h under finite low than under infinite carbon activity. However, as the exposure time is prolonged to more than 5 h, this is different; i.e. the carbon filaments formed under finite low carbon activity are longer and more abundant. This indicates that the mechanism is different, with a longer incubation period but more facile growth once it has been initiated under finite low carbon activity.

Raman spectroscopy was used to further investigate the formation of carbon on the surface. The spectra obtained are displayed in Fig. 5(a) for the I-a_c case and 5(b) for the corresponding FL-a_c exposures. All Raman shifts obtained in the range 1000-3000 cm^{-1} can be related to surface carbon, to which Raman is very sensitive. The main order *G band* in the range 1577-1608 cm^{-1} exists for all sp^2 carbon systems, such as amorphous carbon, carbon nanostructures and graphite. It relates to bond stretching of sp^2 pairs only [43]. The other important band is the *D band*, also called "disorder-induced", is found in the range 1326-1328 cm^{-1}. It requires a defect for momentum conservation, which can be anything that breaks the symmetry in the graphene lattice, such as sp^3-defects [44], vacancies [45], grain boundaries [46], or an edge [47]. The *D' band,* defined as a shoulder observed in the range 1600-1610 cm^{-1}, is also dependent on structural disorder. For some cases, the *2D band* (also called G') recorded in the region 2658 cm^{-1} may be very strong. It originates from a second order Raman process related to the in-plane breathing-like mode of the carbon ring, and is hence directly related to the graphitization of the carbon species [48] and especially sensitive to the number of graphene layers [49,50]. In addition to these common bands, one can add the *D + G band* at 2900 cm^{-1} which is defined as a combination scattering peak [51–53]. In terms of carbon structures deposited on a surface, the intensity of G and 2D bands are both related to the number as well as the order of graphene layers [45,46]. As the extent of disorder in the carbon species increases, the Raman intensity increases for the peaks *D, D´,* and *D + G* [53,54].

The Raman spectra show that the I- a_c carbon structures have many defects due to the presence of D (1327 cm^{-1}), D' (1607 cm^{-1}), and D + G (2900 cm^{-1}) bands (Fig. 5(a)). These bands are relatively prominent after 1 h as compared to G (1577 cm^{-1}) and 2D (2658 cm^{-1}). However, a G and 2D band intensity increase is predominant during prolonged exposure to 10% CO in Ar (1 bar, I-a_c), from 1 h to 20 h at 750 °C, while the full width at half maximum (FWHM) of both peaks clearly decreases. The D band slightly narrows with longer exposures, while - notably - the D´ band increase ceases when the exposure time reaches 20 h. The D + G band does not increase significantly after 1 h. Both the D and G bands are slightly shifted to lower wave numbers. I_{2D} after 5 h is much stronger than after 1 h and 2 h and extended exposure to 20 h yields another large increase. The I_D/I_G intensity ratios are plotted in Fig. 6, and the ratio for I-a_c is decreasing with exposure time. The overall crystallinity of the carbon formed on the pre-oxidized alloy samples is hence improved by prolonged exposure [22,48]. This implies that, during exposure to CO only, some disordered and amorphous carbon synthesizes first, and more ordered carbon is thereafter formed on top [55].

When it comes to the samples exposed to the simulated syngas (FL-a_c) at 20 bar, the D (1327 cm^{-1}), D' (1607 cm^{-1}), and D + G (2900 cm^{-1}) bands display higher intensity in the case of FL-a_c samples than observed for I- a_c (Fig. 5(b)). Furthermore, the D band narrows with exposure time, and the (relatively small) D´ band also seems to increase slightly. Amorphous carbon is dominated by sp^3 even if some sp^2 bonding co-exists (G band) [56]. The abovementioned I_D/I_G ratio (Fig. 6) initially increases strongly, followed by a gradual increase from 5 to 20 h, but always a faster increase in sp^3 hybridization than in sp^2 configuration. The 2D band is not visible for the 1 h exposure but a small, broad peak can be seen after 2 h exposure that only slightly grows until 20 h. This implies that there is no improved crystallinity of the growing carbonaceous deposits. Amorphous carbon is also synthesized first on the pre-oxidized alloy surface during the syngas (FL- a_c) exposure, but what is different compared to the CO (I- a_c) exposure is that disordered carbon maintains predominant.

The differences in carbon growth mean that apart from

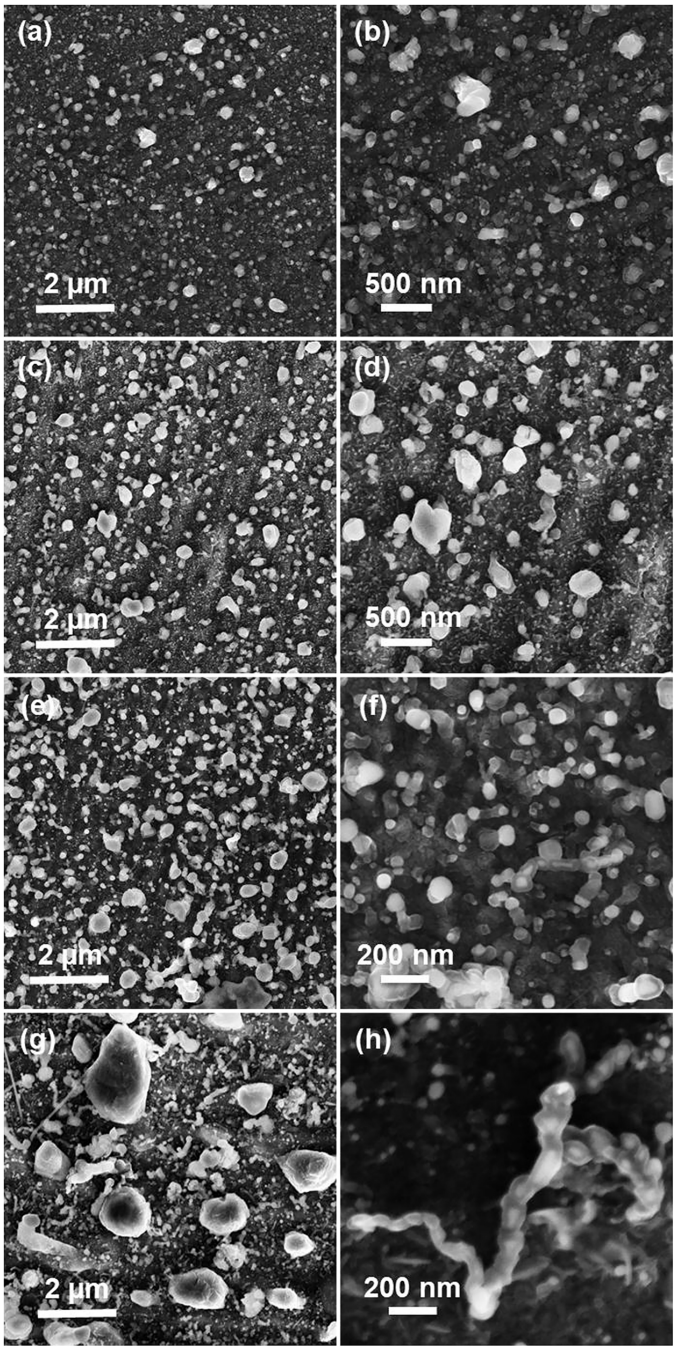

Fig. 3. SEM micrographs at small and large magnification of oxidized Inconel 601 surface after exposure to infinite carbon activity (I- a_c) at 750 °C for (a, b) 1 h; (c, d) 2 h; (e, f) 5 h; (g, h) 20 h. Total pressure 1 bar, 10% CO in Ar.

thermodynamic control in the reaction (a_c), the kinetic dependence on temperature and partial pressures of the gaseous reactants also strongly affects the surface carbon deposition. This is in accordance with observations reported by Zhang and Young showing that for a fixed carbon activity ($a_c = 19$) but varying gas composition, both the Boudouard and the CO reduction reactions contributed to carbon deposition. The gasification of carbon by hydrogen was important at high hydrogen partial pressures [57]. Zhang et al. also compared exposure to

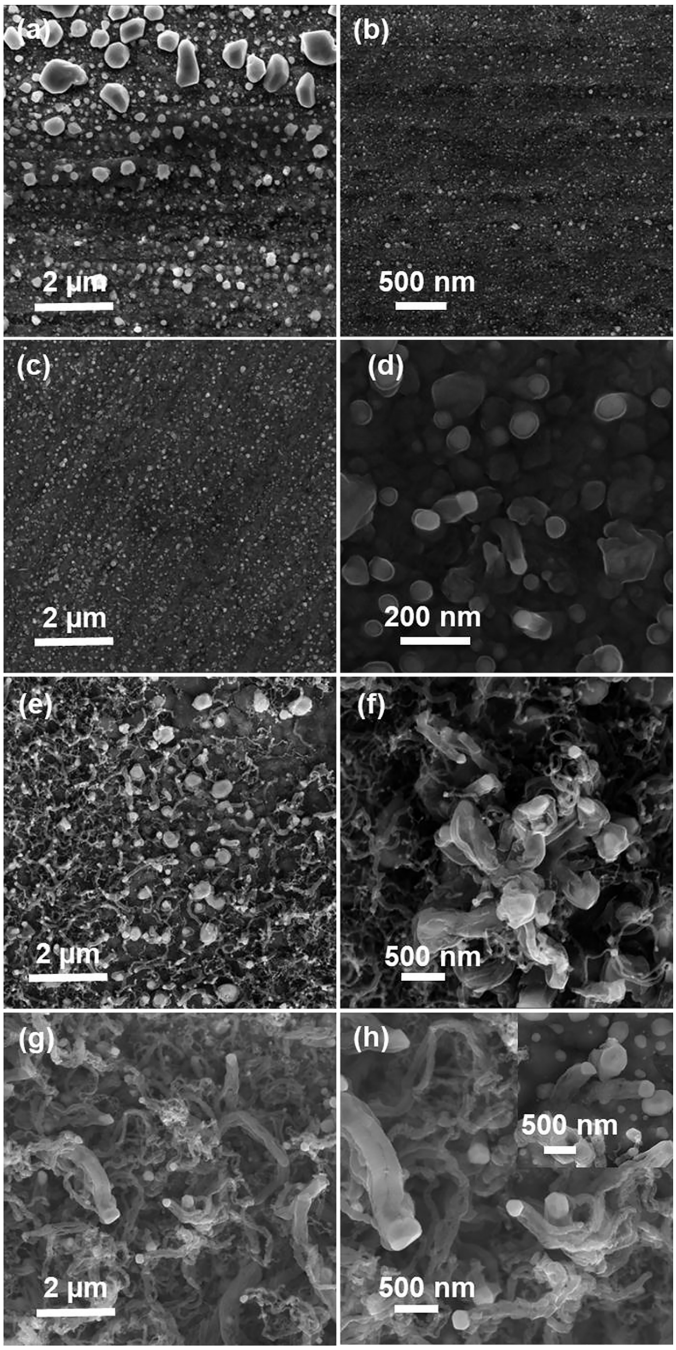

Fig. 4. SEM micrographs at small and large magnification of oxidized Inconel 601 surface after exposure to simulated synthesis gas of finite low carbon activity (FL-a_C), at 750 °C for (a, b) 1 h; (c, d) 2 h; (e, f) 5 h; (g, h) 20 h. Total pressure 20 bar, H_2 (25%), CO (20%), CO_2 (15%), H_2O (10%), Ar (30%).

CO/CO_2 (Boudouard) and $H_2/CO/CO_2$ (CO reduction) mixtures for model Fe-Ni alloys as well as 304 steel, and suggest that the faster rate of the latter reaction can lead to higher degrees of carbon supersaturation in the steel [25,58]. CO reduction being kinetically favored over the Boudouard reaction under metal dusting relevant atmospheres is well established [25,58]. However, it remains to be substantiated if H_2-assisted activation of the CO as known from CO hydrogenation catalysis is important to the nature as well as the rate of the carbon

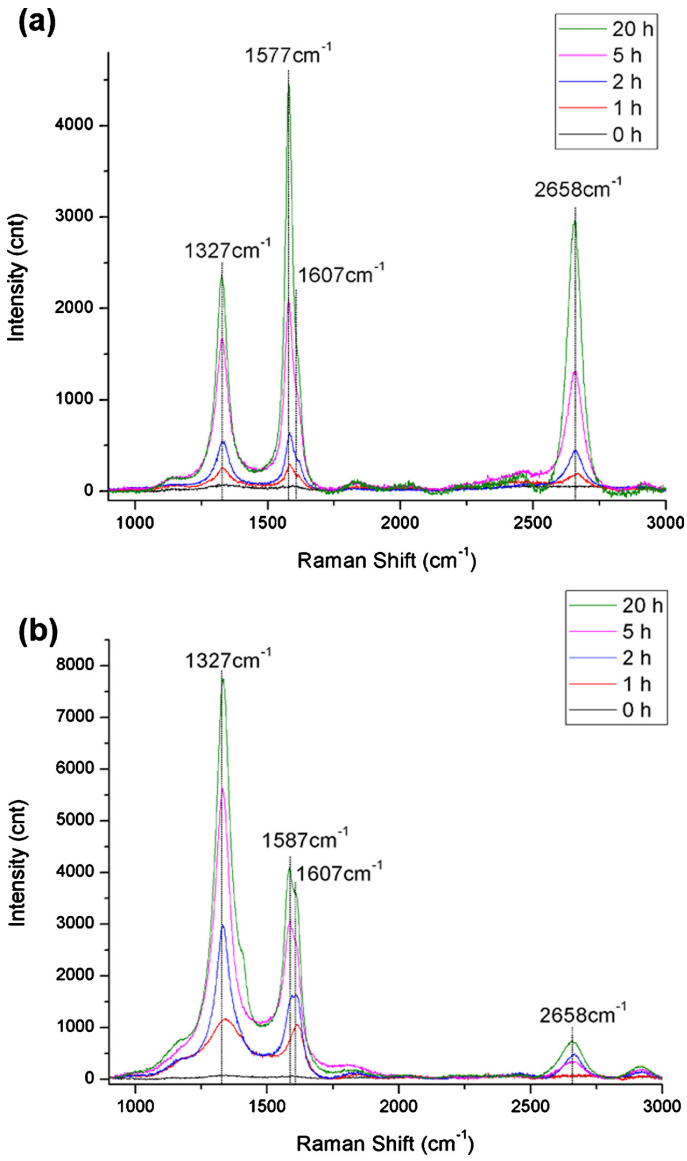

Fig. 5. 1000-3000 cm^{-1} region Raman spectra of oxidized Inconel 601 after exposure to (a) infinite carbon activity (I- a_c) at 750 °C for 0 h, 1 h, 2 h, 5 h and 20 h Total pressure 1 bar, 10% CO in Ar; or (b) simulated synthesis gas of finite low carbon activity (FL- a_c), at 750 °C for 0 h, 1 h, 2 h, 5 h and 20 h. Total pressure 20 bar, H_2 (25%), CO (20%), CO_2 (15%), H_2O (10%), Ar (30%).

formed in this respect [59,60]. Since the samples qualitatively exhibit contradictory behaviors with respect to the initial carbon formation and the progress with longer exposure, this cannot be concluded from the present work. But the kinetics of carbon deposition is here affected by a gradual structure and composition development of the alloy surface. It is thus worth to investigate the composition and structure of the alloy, as well as changes resulting from the exposures.

3.3. Surface oxide layer development

Fig. 7 compares the XRD patterns of the pre-oxidized Inconel 601 samples after 20 h under the two different metal dusting conditions to the sample oxidized in steam only (also shown in Fig. 1 and discussed above). After exposure under infinite carbon activity, Cr_2O_3 emerges as a new phase in addition to the bulk fcc alloy matrix. In contrast, the major additional phase observed by XRD after exposure to finite low carbon activity is (Ni, Fe, Cr)$_3O_4$ spinel [5]. Neither of these could be confirmed by XRD of the pre-oxidized sample only, but both were present in the thin (40-50 nm) surface layer according to Raman. There has clearly been a development in the oxide structure alongside the carbon formation for both exposures. As mentioned before, an adherent Cr_2O_3 scale can protect an alloy from carbon attack. (Ni, Fe, Cr)$_3O_4$ spinel varieties, on the other hand, are not preferred since they are thermodynamically less stable than Cr_2O_3 and can be spalled more

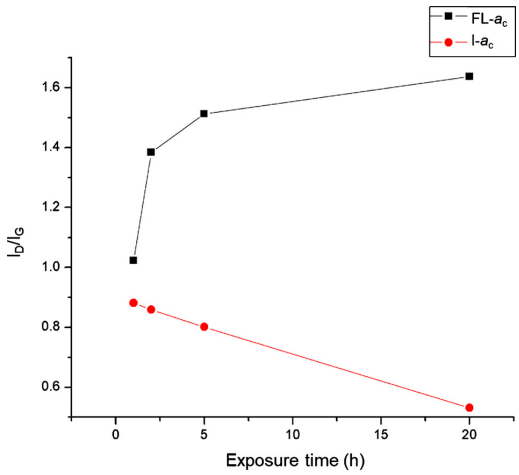

Fig. 6. I_D/I_G intensity ratios of the Raman spectra for oxidized Inconel 601 after exposure to infinite carbon activity (I-a_c) or simulated synthesis gas of finite low carbon activity (FL- a_c) plotted as a function of exposure time.

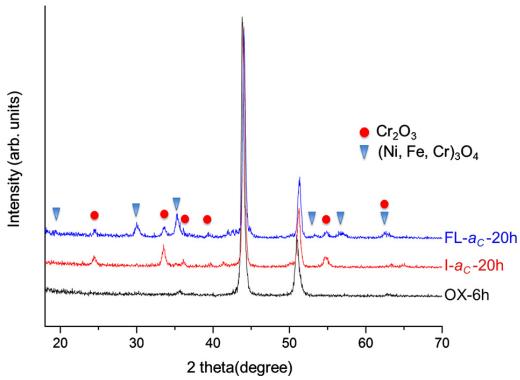

Fig. 7. X-ray diffraction patterns from oxidized Inconel 601 before and after 20 h of exposure to infinite carbon activity (I-a_c) or simulated synthesis gas of finite low carbon activity (FL- a_c).

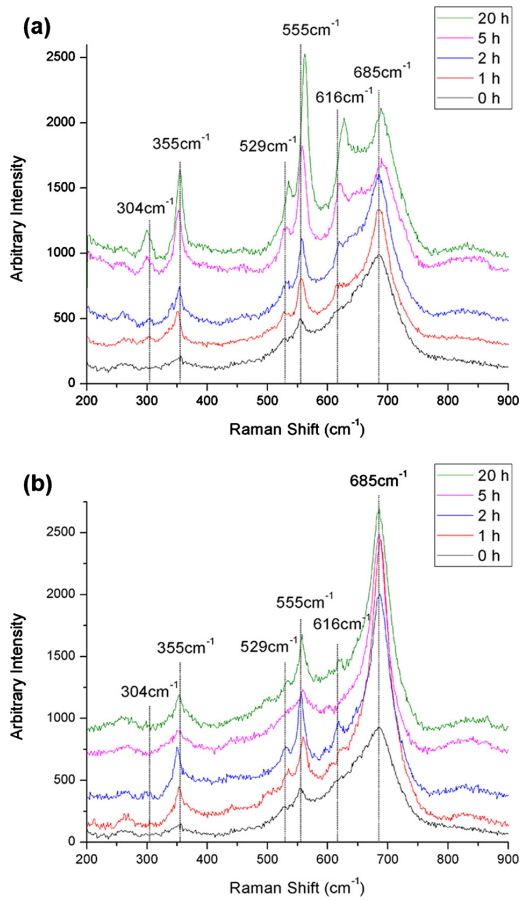

Fig. 8. 200-900 cm^{-1} region Raman spectra of oxidized Inconel 601 after exposure to (a) infinite carbon activity (I- a_c) at 750 °C for 0 h, 1 h, 2 h, 5 h and 20 h Total pressure 1 bar, 10% CO in Ar; or (b) simulated synthesis gas of finite low carbon activity (FL- a_c), at 750 °C for 0 h, 1 h, 2 h, 5 h and 20 h. Total pressure 20 bar, H_2 (25%), CO (20%), CO_2 (15%), H_2O (10%), Ar (30%).

easily as a result of stress [61]. Under metal dusting conditions (Ni, Fe, $Cr)_3O_4$ spinel can be partly reduced upon application in low P_{O2} environments containing CO and/or H_2. Carbon can deposit at the surface of Ni and/or Fe metal particles formed upon reduction [24,62,63]. If the higher content of spinel phase after syngas exposure is a signature of continuous formation and decomposition of spinel, it is a possible reason as to why more carbon is formed than under CO in Ar exposure after the initial incubation.

The Raman spectra from the 200-900 cm^{-1} region shown in Fig. 8(a) and (b) present results complementary to the information from XRD. Fig. 8(a) shows that with extended exposure time under I-a_c, the five peaks of Cr_2O_3 (304, 355, 529, 553 and 616 cm^{-1}) [41] increase in intensity while becoming narrower and more symmetric. The spinel peak at 685 cm^{-1} [35], however, does not change much as the exposure time extends from 1 h to 20 h. The Cr_2O_3/spinel peak ratio is hence clearly increasing in parallel with the formation of solid carbon during exposure to CO. Formation of Cr_2O_3 from the alloy is also governed by the temperature and the diffusion rate of the Cr cation towards the surface [61], in addition to an effective P_{O2}. In principle, the only sources of oxygen are the oxide phases existing in the surface layer and the oxygen from the CO. The development in the Cr_2O_3 may thus be due to either parallel reduction and oxidation occurring within the oxide or transfer of oxygen to the layer due to CO dissociation at elevated temperature. The latter implies that the Boudouard reaction is not the only reaction proceeding, and that the low effective oxygen partial pressure is sufficient to oxidize Cr [58]. The Raman peaks of both Cr_2O_3 and spinel also show slight shifts towards higher wavenumbers relative to the bands recorded for pure chemicals. This is likely caused by a decrease in interatomic distances [64], i.e. mechanical stress may be present within the oxide [65,66]. Such a stress may explain why carbon formation proceeds with continued exposure. Even if the amount of Cr_2O_3 increases, the stress causes defects that allow continuously renewed access to Ni, Fe and/or reducible phases thereof.

For the oxidized alloy samples exposed to FL- a_c, peaks from (Ni, Fe, $Cr)_3O_4$ spinel remains dominant throughout the exposure time compared to Cr_2O_3 as can be seen in Fig. 8(b). The Cr_2O_3/spinel peak ratio remains practically constant, and the abovementioned peak shifts were found for neither the Cr_2O_3 nor the spinel. The slight increase in all peaks parallel to the appearance of the spinel in the XRD pattern after 20 h nevertheless implies development of the oxide. Gunawardana et al. also previously showed by Auger spectrometry an increase in the oxide thickness (~ 500 nm) under same carburizing condition [20]. This

implies reduction as well as oxidation schemes different from the infinite carbon activity, CO only, case. The main difference lies in the presence of H_2, H_2O and CO_2, and the overall higher total pressure. Both H_2O and CO_2 can oxidize Cr and Fe and facilitate the formation of (Ni, Fe, Cr)$_3O_4$ spinel on the surface of the alloy [67], while H_2 may play a role in the reduction of both oxides in addition to CO. Higher total pressure of synthesis gas mixtures has in several contributions, accounting for a wide range of alloy compositions, exposure times and progress of the carburization, been found to lead to more severe metal dusting [68–71]. Nishiyama et al. found, that upon exposure of alloy 800H to carbonaceous environments (100 h, CO, H_2, CO_2 and H_2O), the ratio of Cr_2O_3 to spinel type oxides such as $FeCr_2O_4$ decreases with increasing pressure [69]. Also, Madloch et al. reported that both alloy 600 and alloy 800H could form protective chromium oxide on the metal surface under ambient total system pressure (H_2, CO, CO_2, CH_4, H_2O), while high total pressures lead to the formation of spinels such as $MnCr_2O_4$ and/or $FeCr_2O_4$ [68]. A higher rate of formation for these spinels were proposed to induce stress that in turn can deteriorate the protective behavior. Put et al. ran experiments at different total pressures and gas velocities, but similar a_c (H_2, CO, CO_2, CH_4, H_2O/H_2, CO, H_2O), and found that the metal dusting mass loss increases and the average incubation time decreases with pressure for both the HR120 and 800H alloys [70]. Natesan and Zeng also reported that for similar a_c (H_2, CO, CO_2, H_2O/H_2, CO, H_2O), all the 6 different alloys tested showed a decrease in initiation time for metal dusting degradation at higher total pressure [71].

3.4. Cross-section analysis

Three TEM lamellae were prepared by FIB milling from the sample surface after metal dusting corrosion testing, one after 20 h exposure to I-a_c (Figs. 9 and 10) and another two from 2 h (Fig. 11) and 20 h (Fig. 12) exposure to FL-a_c conditions. The red line in the SEM image of Fig. 9(a) shows the location of the cross-section I-a_c TEM lamella. It extends through a region in the center with less carbon, seemingly a surface of different characteristics than the surroundings. The cross-section SEM image of the lamella with carbon protection layer after milling is shown in Fig. 9(b), and this is a good example of a TEM lamella where ion-beam damage has been avoided. The carbon filaments on the surface and the grain boundaries underneath are not very clear due to the low magnification. Low-angle annular dark-field scanning transmission electron microscopy (LAADF STEM) was therefore employed to obtain more details of the region within the red square in Fig. 9(b), as shown in Fig. 9(c). Carbon filaments with metal particles at the tip can be observed on the top of the lamella within the carbon protection layer. The diameter of these carbon filaments varies over a broad range. Grain boundaries are indicated by blue lines in the figure. It can be seen that the mid-section grain is resulting from a straight grain boundary that goes from the bulk towards the surface, an then bends to continue relatively parallel to the surface (blue solid line in figure) before extending to the surface on the right. Thus, the center area with less carbon is associated with a relatively small and shallow part of a larger grain.

Chemical composition mapping by simultaneous EDS and EELS was performed from the two regions indicated by red rectangles in Fig. 9(c). The element maps are displayed in Fig. 10(a) and (b) for the right and left of these two regions, respectively. The elementary maps for O, Cr and Mn in Fig. 10(a) confirm that a thin Cr-rich oxide covers the alloy surface. As to be expected, the bulk matrix under the surface oxide layer is rich in Ni and Fe. The shallow grain boundary is located in the middle of Fig. 10(a) and striking differences can be observed between each side of this grain boundary. Firstly, while the shallow part of the grain to the left appears depleted in Cr, Cr-rich oxide precipitates can be observed inside the grain on the right. Mn generally tends to be accompanied with the Cr. Small Ni and Fe rich particles are clearly also present on top of the oxide, and seemingly more abundant to the right than to the left. Al and Ti were found as oxides mainly at the interface between the bulk alloy and the Cr-rich scale, and it is worth to note that the Al and Ti EDS signal is stronger on the left side than on the right side of the grain boundary (See Fig. S2 in the Supporting Information). Slight Si enrichment can also be observed at the interface between the alloy and the oxide scale.

Due to insufficient EDS signal from carbon, EELS was applied for the C-mapping. The carbon protection layer deposited during FIB preparation dominates the C element map. However, the carbon located in the filaments can still be distinguished from the amorphous carbon protection layer. The carbon deposits consist of filaments of various length and thickness, and the observation that there is less carbon at the surface of the shallow grain is apparent also in the cross-section TEM lamella. The Ni and Fe rich metal nanoparticles are clearly associated with the tip of the carbon filaments. It should also be noted that significant O, Cr, Mn and a little bit of Fe can be observed inside the carbon filaments. The carbon growth could hence be related to a partial decomposition of (Ni, Fe, Cr)$_3O_4$ spinel phases present after steam

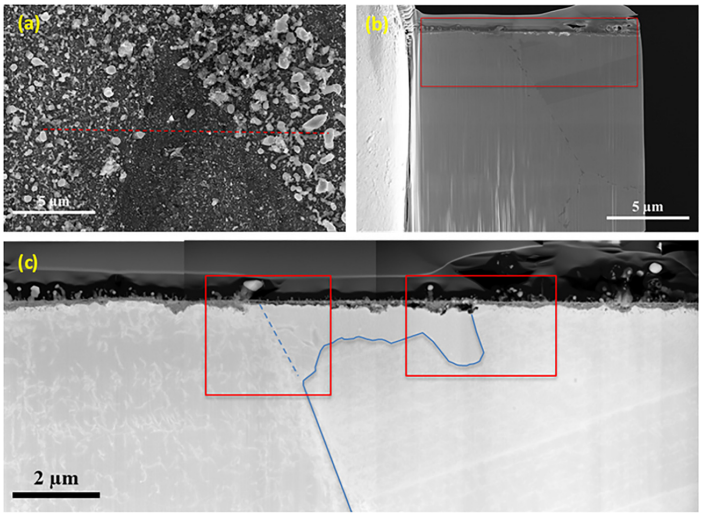

Fig. 9. Preparation of TEM lamella by FIB milling from oxidized Inconel 601 after exposure to infinite carbon activity (I-a_c) at 750 °C for 20 h. (a) SEM surface view of the region from where the FIB sample was selected. (b) SEM image of the cross-section TEM lamella, region indicated in red square is further analyzed by LAADF STEM. A thin protection layer of C was deposited on the alloy surface before ion milling, and can be observed in upper part of the images. (c) LAADF STEM image of the TEM lamella with solid line indicating grain boundary and dashed line indicating the extension line of this grain boundary into the grain matrix and towards the surface. The two red squares indicate regions further analyzed by EDS and EELS (Fig. 10).

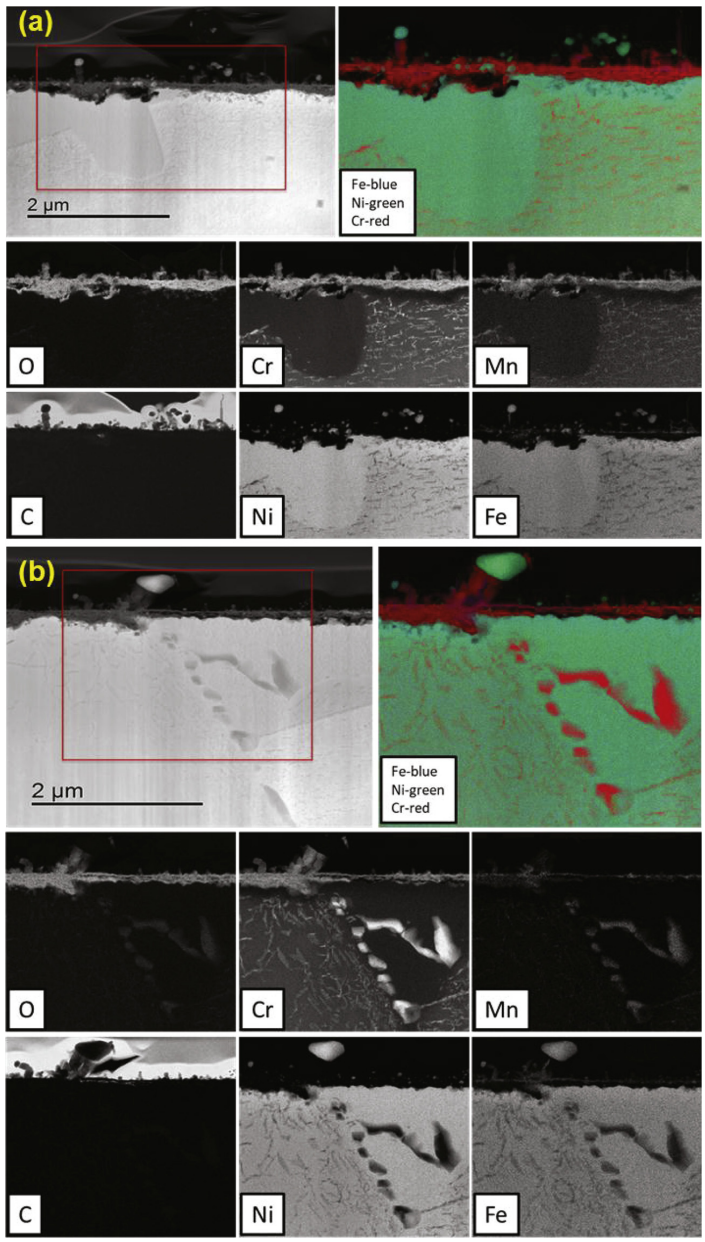

Fig. 10. STEM images, EELS (C signal) and EDS (other signals) element mapping, and RGB element merge of selected regions of TEM lamella milled by FIB from oxidized Inconel 601 sample after exposure to infinite carbon activity (I- a_c) at 750 °C for 20 h; (a) right region and (b) left region indicated by the red squares in Fig. 9.

oxidation pre-treatment, which then serve as "impure" catalyst particles for the first carbon deposition. Further CO exposure makes the filaments grow and lifts the catalyst particles up while simultaneously leaving behind "impurities" along the core of the filaments to render the particle at the tip as an increasingly pure Ni-Fe alloy. This suggests that (Ni, Fe, Cr)$_3$O$_4$ spinel is not formed in reaction with CO only and may explain why the overall crystallinity of the carbon formed under prolonged exposures to I-a_c is improved as discussed above.

Fig. 10(b) only covers a short part of the grain boundary, in the lower right corner of this region. However, it is interesting to see that some Cr-rich oxide precipitates form a line (indicated as dash line in Fig. 9(c)) exactly at the extension of the straight grain boundary underneath. On the left side of this "precipitate boundary" the surface Cr-oxide layer is relatively thick (100-290 nm) and underneath Cr-rich oxide precipitates are found homogeneously dispersed within the Ni-Fe matrix. On the right side, on the other hand, the surface oxide layer is

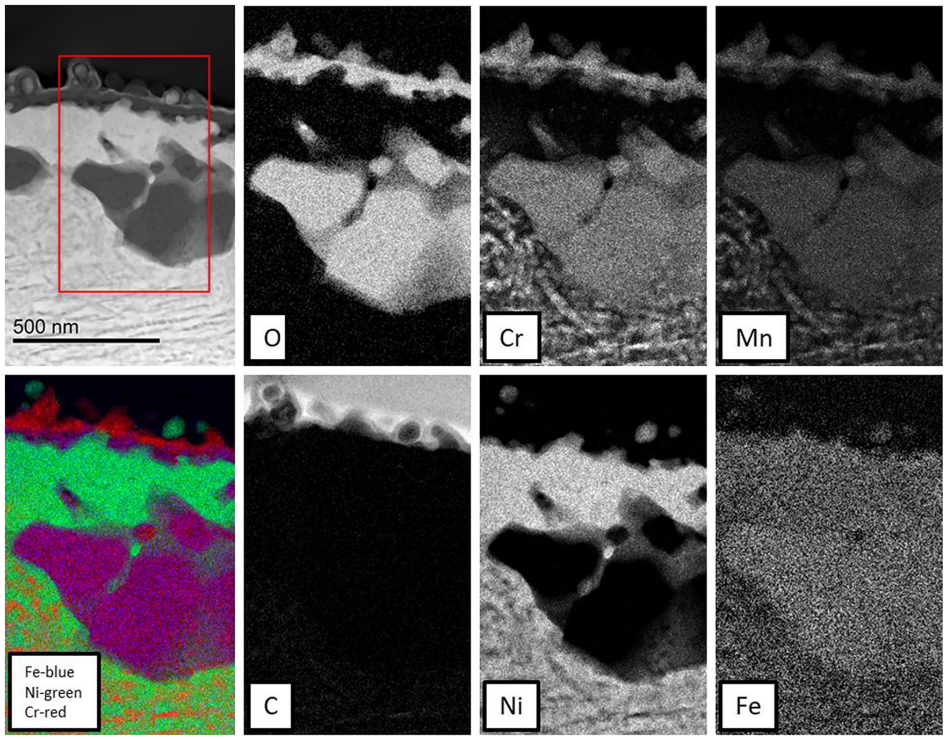

Fig. 11. STEM images, EELS (C and Fe signals) and EDS (other signals) element mapping, and RGB element merge of selected regions of TEM lamella milled by FIB from oxidized Inconel 601 sample after exposure to finite low carbon activity (FL- a_c), at 750 °C for 2 h. A thin protection layer of C was deposited on the alloy surface before ion milling, and can be observed as background in the C map.

thinner (70-100 nm) and underneath the internal Cr-rich oxide precipitates are fewer, larger and form a long meandering strip. Surrounding the Cr-rich precipitates, the shallow part of the grain has become depleted in Cr. All of this indicates that the grain boundary has played a role in the transport of Cr towards the surface, supporting the notion that grain boundaries are channels for Cr [72].

As could be inferred from the SEM images in Fig. 4, the amount of carbonaceous deposits after exposure to the finite carbon activity, simulated syngas (FL-a_c) was much higher after 20 h than for the corresponding CO only exposure. However, the 2 h FL-a_c exposure presented a surface with similar appearance (Fig. 4(c) and (d)) as the 20 h I-a_c. Thus, a TEM lamella was prepared from the former by FIB milling. Fig. 11 shows chemical composition mapping by EDS and EELS. The element maps of O, Cr, and Mn confirm that a Cr-rich oxide covers the alloy surface also here; ~40-96 nm thick as observed from the dark field STEM and including Mn. Metal particles with only a few layers of carbon are observed on top of the oxide. These catalyst particles are rich in Ni but contain also some Fe. Close inspection reveals that they are also actually wrapped by a thin layer of Cr-rich oxide, and this could be the signature of a decomposed spinel phase (See Fig. S3 in the Supporting Information). Below the surface oxide layer, large oxide precipitates can be observed, reaching ~550 nm into the matrix, which are rich in Cr and may contain some Fe. More dispersed Cr-rich oxide precipitates are found below the large precipitates, but not above them. Similar to the sample in Fig. 10, slight Si, Al and Ti enrichment can be observed at the alloy and oxide scale interface (See Fig. S4 in the Supporting Information).

To reach the oxide layer of the alloy and enable further sample preparation, the carbon and corrosion products after 20 h exposure to the finite carbon activity, simulated syngas (FL-a_c) were removed by ultrasonic agitation in acetone. Pt deposition to protect the surface layer during ion milling was applied before TEM lamella preparation. Fig. 12 shows a TEM lamella on which a corrosion pit has developed. EDS based element maps from the region labelled by the red frame in the dark field STEM image are also shown. These element maps show that oxygen has penetrated much deeper into the alloy matrix compared to the alloy samples exposed to I-a_c, yielding a 430-830 nm thick oxide layer. It can be observed from the dark field STEM image that the surface oxide consists of two layers: A seemingly porous, ~ 170 nm dark STEM contrast layer on the top with a thicker ~260 - 660 nm discontinuous layer below. This thick layer probably results from continued formation of Cr-rich oxide precipitates such as those observed from Fig. 11. O, Cr and Mn are overlapped within the entire oxide layer. Filamentous carbon within the pit indicates that strongly attached carbon filaments were not removed by the ultrasonic agitation and preserved during FIB milling. Carbon is also found progressed into the topmost oxide, and this has previously also been substantiated from Auger depth profiles from same exposures [20]. The Ni and Fe maps show that metallic Ni-Fe phases occupy the interstice within the discontinuous oxide. Ni and Fe rich nanoparticles are also observed in the pit, which indicate that these particles serve as catalysts for carbon deposition. The original oxide scale must have been destroyed in the pitting area; however, a new, thin less protective oxide has formed at the bottom of the pit with similar composition outside of the pit. A similar observation was also made by Zhang et al [58]. When the protective chromia was lost, inward diffusion of O resulted in the formation of less protective internal precipitates such as $FeCr_2O_4$ or other spinel types. It should be noted that the Pt protection layer gives an enhanced bremsstrahlung background signal compared to the rest of the mapped region that shows up as an artefact in the Al, Ti and Si maps

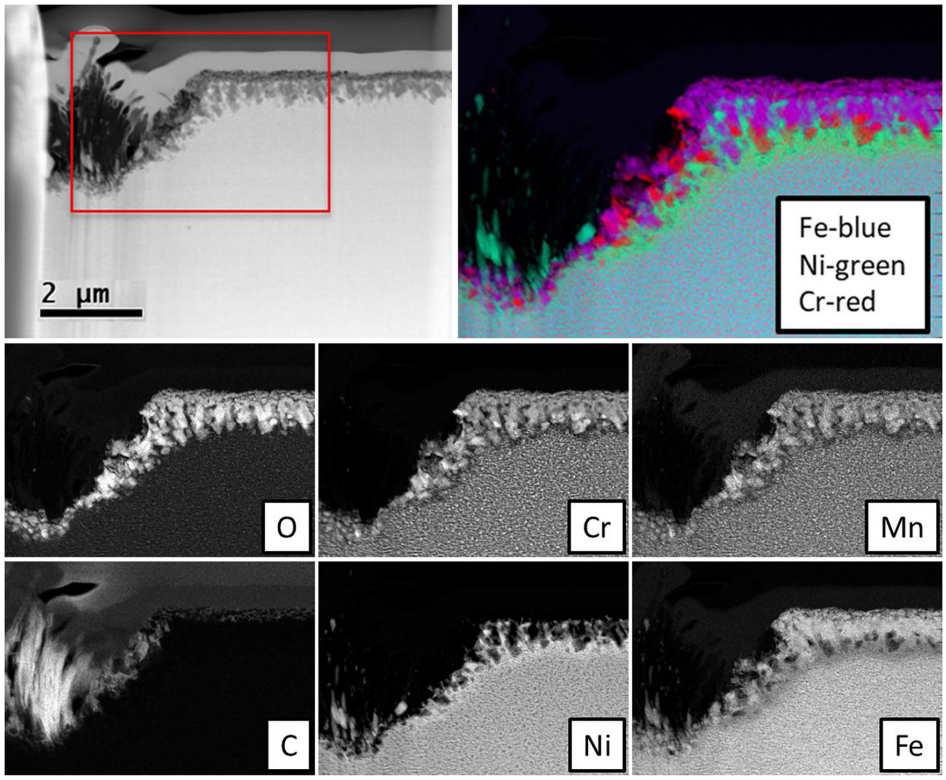

Fig. 12. STEM image, EDS element mapping and RGB element merge of region selected from TEM lamella milled by FIB from oxidized Inconel 601 after exposure to simulated synthesis gas of finite low carbon activity (FL- a_c), at 750 °C for 20 h and subsequently subjects to ultrasonic cleaning. A thin protection layer of Pt was deposited on the alloy surface before ion milling that can be observed in the upper left image.

(See Fig. S5 in the Supporting Information). Nevertheless, Al, and possibly also Ti and Si signals are distinguishable at the interface between the bulk alloy and the oxide scale, but part of the Al is also dispersed within the oxide layer, more dispersed than for the sample exposed to I- a_c.

By comparing Figs. 10 and 12, we can see that oxide scale developed under I-a_c is significantly thinner (~70-290 nm) than that developed under FL-a_c (~430-830 nm). The central part of the TEM lamella where the oxide is thinnest produced the least amount of carbon filaments. This indicates that a protective oxide scale against metal dusting corrosion is not necessarily thick. Presumably, a dense, defect free and chemical stable oxide is desired. The central area showed in Fig. 9(c), located between a grain boundary and a dashed line which function similar to a grain boundary, represents a local fine-grained structure. The impact of a fine grain-structure thus appears to have been rapid formation of a thin, but comparatively resistant surface oxide. A fine-grained structure is found to provide diffusion paths along grain boundaries, sub-boundaries and dislocations, resulting in an enhanced Cr diffusivity that enables a faster formation of a protective, Cr-rich oxide in the surface region [6,73]. Grain boundaries are also associated with interphase energy, hence yielding an overall more reactive phase [74–76]. The relatively dense Al oxide scale beneath may also play an important role in mitigating metal dusting attack [5].

Finally, the kinetics and thermodynamics of the oxide formation under FL-a_c produces a different oxide than under I-a_c. The presence of steam and CO_2 and significantly higher partial pressures of the oxygen species ($CO/H_2O/CO_2$) yields deeper oxidation in parallel with the carbon formation but seems to favor spinel over Cr oxide. This (Ni, Fe, $Cr)_3O_4$ spinel is subsequently reduced and thereby more prone to participate in continued formation of highly defected carbon. It remains to fully explain the formation of Cr_2O_3 under CO exposure only (I-a_c) and to which extent it eventually can inhibit further progress of the carbon formation. It could be that a low efficient oxygen partial pressure is beneficial in terms of allowing sufficient transport of Cr for the reaction. Likewise, the key mechanism for spinel formation should be established, but interplay between Cr transport and the kinetics of reducing (H_2/CO) and oxidizing reactions (H_2O/CO_2) likely is important.

4. Conclusion

Nickel-based alloy (Inconel 601) samples have been pre-oxidized in 10% steam in Ar at 540 for 6 h before exposure to two different metal dusting conditions at 750 °C. We have shown that by varying the exposure times over relatively short exposures, we may capture the initiation and progress of carbon formation on alloy surfaces that eventually leads to metal dusting. The carbon deposition is clearly a function of the gas composition during exposure. After 20 h, less carbon has formed under 10% CO in Ar (1 bar), i.e infinite carbon activity (I-a_c), than under synthesis gas with finite low carbon activity (FL-a_c; 25% H_2, 20% CO, 15% CO_2, 10% H_2O, and 30%Ar, 20 bar). However, the formation of carbon under FL-a_c exhibits a longer incubation period than under I-a_c, but more facile growth after the first 1-2 h. SEM confirms the formation of filamentous carbon for both exposures, albeit overall larger diameters with H, CO_2 and H_2O present in the mixture. Moreover, Raman spectroscopy reveals significant differences in the nature of the carbon formed. With only CO reacting (I-a_c), more ordered

carbon develops as the exposure time increases, while this is not case under synthesis gas. Combined, this points to a difference the catalytic reaction mechanism and kinetics on the surface.

In addition, XRD, Raman and TEM characterization reveal that the surface oxide layer formed on Inconel 601 develops very differently under the two metal dusting conditions applied. Cr_2O_3 develops as a thin surface oxide scale layer under exposure to CO in Ar. A more fine-grain structure present near the surface in certain regions on this sample is found important in terms of rapidly supplying Cr, Mn and Al to the surface under elevated temperature to form a better protective layer and thereby slowing the metal dusting corrosion. TEM analysis captured another interesting evolution under I-a_c, which suggests "purification" of the catalyst particles along with carbon filaments growth as a possible reason for the improved overall crystallinity of the carbon formed during prolonged exposure. In presence of synthesis gas (FL-a_c), oxidation proceeds within a larger part of the near-surface region, but results to a higher extent in (Ni, Fe, Cr)$_3O_4$ spinel formation. We suggest that this phase continuously forms and reduces to new carbon formation catalyst (Ni, Fe) particles that nucleate the formation of more, less ordered carbon.

CRediT authorship contribution statement

Xiaoyang Guo: Conceptualization, Validation, Formal analysis, Investigation, Data curation, Writing - original draft, Writing - review & editing, Visualization. **Estelle Vanhaecke:** Methodology, Validation, Formal analysis, Investigation, Data curation, Writing - original draft, Visualization. **Per Erik Vullum:** Methodology, Validation, Formal analysis, Investigation, Data curation, Writing - original draft, Visualization. **Jianyu Ma:** Validation, Investigation. **P.V. Daham S. Gunawardana:** Methodology, Investigation. **John C. Walmsley:** Conceptualization, Methodology, Formal analysis, Investigation. **De Chen:** Conceptualization, Project administration, Funding acquisition. **Hilde J. Venvik:** Conceptualization, Methodology, Writing - original draft, Writing - review & editing, Supervision, Funding acquisition.

Declaration of Competing Interest

The authors declare that they have no known competing financial interests or personal relationships that could have appeared to influence the work reported in this paper.

Acknowledgements

The financial support of Research Council of Norway under the GASSMAKS research program (Contract No. 233869/E30) is gratefully acknowledged. The TEM work was carried out on NORTEM infrastructure, Grant 197405, TEM Gemini Centre, Norwegian University of Science and Technology (NTNU), Norway. The Research Council of Norway is acknowledged for the support to the Norwegian Micro- and Nano-Fabrication Facility, NorFab, project number 245963/F50.

Appendix A. Supplementary data

Supplementary material related to this article can be found, in the online version, at doi:https://doi.org/10.1016/j.cattod.2020.04.029.

References

[1] M. Holland, H. De Bruyn, Metal dusting failures in methane reforming plant, International journal of pressure vessels and piping 66 (1–3) (1996) 125–133.
[2] A.B. Tomkings, T. Lant, Operating Experience of Metal Dusting Failures, CORROSION 2001 (2001).
[3] S. Kaewkumsai, W. Khonraeng, N. Sathirachinda, High temperature failure of natural gas feed burner pipe, Engineering Failure Analysis 27 (2013) 74–83, https://doi.org/10.1016/j.engfailanal.2012.08.004.
[4] J. Orlikowski, A. Jazdzewska, K. Darowicki, J. Karczewski, J. Dampc, R. Gospos, Metal dusting phenomena of 501 AISI furnace tubes in refinery fractional distillation unit, Engineering Failure Analysis 91 (2018) 108–114.
[5] Z. Zeng, K. Natesan, M. Grimsditch, Effect of oxide scale compositions on metal dusting corrosion of Fe-based alloys, Corrosion 60 (7) (2004) 632–642.
[6] H. Grabke, E. Muller-Lorenz, S. Strauss, E. Pippel, J. Woltersdorf, Effects of grain size, cold working, and surface finish on the metal-dusting resistance of steels, Oxid. Met. 50 (3) (1998) 241–254.
[7] C. Toh, P. Munroe, D. Young, Metal dusting of Fe–Cr and Fe–Ni–Cr alloys under cyclic conditions, Oxid. Met. 58 (1–2) (2002) 1–21.
[8] R. Lobnig, H. Schmidt, K. Hennesen, H. Grabke, Diffusion of cations in chromia layers grown on iron-base alloys, Oxid. Met. 37 (1–2) (1992) 81–93.
[9] H. Li, W. Chen, High temperature carburization behaviour of Mn–Cr–O spinel oxides with varied concentrations of manganese, Corros. Sci. 53 (6) (2011) 2097–2105.
[10] H. Li, W. Chen, Stability of MnCr2O4 spinel and Cr2O3 in high temperature carbonaceous environments with varied oxygen partial pressures, Corros. Sci. 52 (7) (2010) 2481–2488.
[11] H. Li, Y. Zheng, L.W. Benum, M. Oballa, W. Chen, Carburization behaviour of Mn–Cr–O spinel in high temperature hydrocarbon cracking environment, Corros. Sci. 51 (10) (2009) 2336–2341.
[12] T.A. Ramanarayanan, C. Chun, Metal dusting resistant alloys, ed: Google Patents (2004).
[13] B. Bao, J. Liu, H. Xu, B. Liu, W. Zhang, Inhibitory effect of MnCr 2 O 4 spinel coating on coke formation during light naphtha thermal cracking, RSC Advances 6 (73) (2016) 68934–68941.
[14] R. Hochman, The fundamentals of metal dusting, API Division of Refining Proc 46 (1966), p. 331.
[15] H. Grabke, R. Krajak, E. Müller-Lorenz, Metal dusting of high temperature alloys, Mater. Corros. 44 (3) (1993) 89–97.
[16] H. Grabke, R. Krajak, E. Müller-Lorenz, S. Strauß, Metal dusting of nickel-base alloys, Mater. Corros. 47 (9) (1996) 495–504.
[17] C. Chun, T. Ramanarayanan, J. Mumford, Relationship between coking and metal dusting, Mater. Corros. 50 (11) (1999) 634–639.
[18] H. Grabke, R. Krajak, J.N. Paz, On the mechanism of catastrophic carburization: 'metal dusting', Corros. Sci. 35 (5–8) (1993) 1141–1150.
[19] P. Szakalos, R. Pettersson, S. Hertzman, An active corrosion mechanism for metal dusting on 304L stainless steel, Corros. Sci. 44 (10) (2002) 2253–2270.
[20] P.D.S. Gunawardana, T.T.M. Nguyen, J.C. Walmsley, H.J. Venvik, Initiation of metal dusting corrosion in conversion of natural gas to syngas studied under industrially relevant conditions, Industrial & Engineering Chemistry Research 53 (5) (2013) 1794–1803.
[21] H. Grabke, Thermodynamics, mechanisms and kinetics of metal dusting, Mater. Corros. 49 (5) (1998) 303–308.
[22] Z. Zeng, K. Natesan, V.A. Maroni, Investigation of Metal-Dusting Mechanism in Fe-Base Alloys Using Raman Spectroscopy, X-Ray Diffraction, and Electron Microscopy, Oxid. Met. 58 (1/2) (2002) 24.
[23] H. Grabke, M. Schütze, Corrosion by Carbon and Nitrogen: Metal Dusting, Carburisation and Nitridation, Elsevier, 2014.
[24] D.J. Young, J. Zhang, C. Geers, M. Schütze, Recent advances in understanding metal dusting: A review, Mater. Corros. 62 (1) (2011) 7–28, https://doi.org/10.1002/maco.201005675.
[25] J. Zhang, D.J. Young, Coking and dusting of Fe–Ni alloys in CO–H2–H2O gas mixtures, Oxid. Met. 70 (3–4) (2008) 189–211.
[26] H.J. Grabke, E.M. Müller-Lorenz, B. Eltester, M. Lucas, D. Monceau, Resistance of 9–20% Cr-steels against metal dusting, steel research international 68 (4) (1997) 179–185.
[27] S. Strauß, R. Krajak, H. Grabke, Coking by metal dusting of nickel-base alloys, Mater. Corros. 50 (11) (1999) 622–627.
[28] D.L. Klarstom, L.D. Paul, H.J. Grabke, The metal dusting behavior of several high temperature nickel based alloys, CORROSION 2001, NACE International, 2001.
[29] Y. NISHIYAMA, K. MORIGUCHI, H. OKADA, T. OSUKI, S. KURIHARA, Development of Metal Dusting Resistant Alloy for Synthesis Gas Production Plants, NIPPON STEEL & SUMITOMO METAL TECHNICAL REPORT, (2015).
[30] A.R.-V. Put, K.A. Unocic, M.P. Brady, B.A. Pint, Performance of chromia-and alumina-forming Fe-and Ni-base alloys exposed to metal dusting environments: The effect of water vapor and temperature, Corros. Sci. 92 (2015) 58–68.
[31] H. Stahl, G. Smith, S. Wastiaux, Strain-age cracking of alloy 601 tubes at 600° C, Practical failure analysis 1 (1) (2001) 51–54.
[32] C.H. Toh, P.R. Munroe, D.J. Young, K. Foger, High temperature carbon corrosion in solid oxide fuel cells, Mater. High Temp. 20 (2) (2003) 129–136, https://doi.org/10.1179/mht.2003.016.
[33] F. Mulaudzi, L. Cornish, G. Slabbert, M. Papo, J. Zhang, A study of metal dusting corrosion on Fe-and Ni-based alloys, Journal of the Southern African Institute of Mining and Metallurgy 113 (2) (2013) 121–128.
[34] C.M. Chun, T.A. Ramanarayanan, Metal dusting resistant alumina forming coatings for syngas production, Corros. Sci. 51 (11) (2009) 2770–2776, https://doi.org/10.1016/j.corsci.2009.08.011.
[35] Z. Zeng, K. Natesan, Relationship of carbon crystallization to the metal-dusting mechanism of nickel, Chem. Mater. 15 (4) (2003) 872–878.
[36] Y. Nishiyama, H. Okada, T. Osuki, S. Kurihara, H. Ogawa, Improved metal dusting resistance of new sumitomo 696 ni-base alloy for synthesis gas environments, Nitrogen+ Syngas 2011 International Conference (2011) 129–138.
[37] J.C. Walmsley, J.Z. Albertsen, J. Friis, R.H. Mathiesen, The evolution and oxidation of carbides in an Alloy 601 exposed to long term high temperature corrosion conditions, Corros. Sci. 52 (12) (2010) 4001–4010, https://doi.org/10.1016/j.corsci.2010.08.015.

[38] P. Gunawardana, H. Venvik, J. Walmsley, Investigation of the initial stage of metal dusting corrosion in the conversion of natural gas to synthesis gas, CORROSION 2013, NACE International, 2013.
[39] P. Gunawardana, J. Walmsley, A. Holmen, D. Chen, H.J. Venvik, Metal dusting corrosion initiation in conversion of natural gas to synthesis gas, Energy Procedia 26 (2012) 125–134.
[40] P. Gunawardana, Carbon formation phenomena and the initial stage of metal dusting corrosion–an experimental investigation, (2014).
[41] D. Thierry, et al., In-Situ Raman Spectroscopy Combined with X-Ray Photoelectron Spectroscopy and Nuclear Microanalysis for Studies of Anodic Corrosion Film Formation on Fe-Cr Single Crystals, J. Electrochem. Soc. 135 (2) (1988) 305–310.
[42] Z. Zeng, K. Natesan, Relationship between the growth of carbon nanofilaments and metal dusting corrosion, Chem. Mater. 17 (14) (2005) 3794–3801.
[43] M. Tamor, W. Vassell, "Raman "fingerprinting"of amorphous carbon films, J. Appl. Phys. 76 (6) (1994) 3823–3830.
[44] A. Eckmann, et al., Probing the nature of defects in graphene by Raman spectroscopy, Nano Lett. 12 (8) (2012) 3925–3930.
[45] M.M. Lucchese, et al., Quantifying ion-induced defects and Raman relaxation length in graphene, Carbon 48 (5) (2010) 1592–1597.
[46] L.G. Cançado, et al., Quantifying defects in graphene via Raman spectroscopy at different excitation energies, Nano Lett. 11 (8) (2011) 3190–3196.
[47] L. Cancado, M. Pimenta, B. Neves, M. Dantas, A. Jorio, Influence of the atomic structure on the Raman spectra of graphite edges, Phys. Rev. Lett. 93 (24) (2004) 247401.
[48] Y. Sato, M. Kamo, N. Setaka, Raman spectra of carbons at 2600–3300 cm − 1 region, Carbon 16 (4) (1978) 279–280.
[49] J. Park, A. Reina, R. Saito, J. Kong, G. Dresselhaus, M. Dresselhaus, G′ band Raman spectra of single, double and triple layer graphene, Carbon 47 (5) (2009) 1303–1310.
[50] Z. Luo, C. Cong, J. Zhang, Q. Xiong, T. Yu, The origin of sub-bands in the Raman D-band of graphene, Carbon 50 (11) (2012) 4252–4258.
[51] M. Pimenta, G. Dresselhaus, M.S. Dresselhaus, L. Cancado, A. Jorio, R. Saito, Studying disorder in graphite-based systems by Raman spectroscopy, PCCP 9 (11) (2007) 1276–1290.
[52] A.C. Ferrari, D.M. Basko, Raman spectroscopy as a versatile tool for studying the properties of graphene, Nat Nanotechnol 8 (April (4)) (2013) 235–246, https://doi.org/10.1038/nnano.2013.46.
[53] I. Childres, L.A. Jauregui, W. Park, H. Cao, Y.P. Chen, Raman spectroscopy of graphene and related materials, New developments in photon and materials research 1 (2013).
[54] R. Saito, M. Hofmann, G. Dresselhaus, A. Jorio, M. Dresselhaus, Raman spectroscopy of graphene and carbon nanotubes, Advances in Physics 60 (3) (2011) 413–550.
[55] X. Guo, P. Gunawardana, D. Chen, E. Vanhaecke, H. Venvik, J. Walmsley, Investigation of Metal Dusting Corrosion Process over UNS N08800 Alloy, CORROSION 2017, NACE International, 2017.
[56] P.K. Chu, L. Li, Characterization of amorphous and nanocrystalline carbon films, Materials Chemistry and Physics 96 (2–3) (2006) 253–277.
[57] J. Zhang, D.J. Young, Kinetics and mechanisms of nickel metal dusting I. Kinetics and morphology, Corros. Sci. 49 (3) (2007) 1496–1512.
[58] J. Zhang, K. Boddington, D.J. Young, Oxidation, carburisation and metal dusting of 304 stainless steel in CO/CO2 and CO/H2/H2O gas mixtures, Corros. Sci. 50 (11) (2008) 3107–3115, https://doi.org/10.1016/j.corsci.2008.08.017.
[59] M. Ojeda, R. Nabar, A.U. Nilekar, A. Ishikawa, M. Mavrikakis, E. Iglesia, CO activation pathways and the mechanism of Fischer–Tropsch synthesis, J. Catal. 272 (2) (2010) 287–297.
[60] M. Ojeda, A. Li, R. Nabar, A.U. Nilekar, M. Mavrikakis, E. Iglesia, Kinetically relevant steps and H2/D2 isotope effects in Fischer − Tropsch synthesis on Fe and Co catalysts, The Journal of Physical Chemistry C 114 (46) (2010) 19761–19770.
[61] M.W. Edwards, N.S. McIntyre, Gas Phase Initial Oxidation of Incoloy 800 Surfaces, Oxid. Met. 79 (1–2) (2013) 179–200.
[62] H. Grabke, I. Wolf, Carburization and oxidation, Materials Science and Engineering 87 (1987) 23–33.
[63] M. Harper, M. Ducasse, D. Young, Cyclic oxidation plus carburization of heat-resistant alloys, Corrosion 51 (3) (1995) 191–200.
[64] J. Mougin, T. Le Bihan, G. Lucazeau, High-pressure study of Cr 2 O 3 obtained by high-temperature oxidation by X-ray diffraction and Raman spectroscopy, J. Phys. Chem. Solids 62 (3) (2001) 553–563.
[65] K. Kitamura, Y. Nishiyama, N. Otsuka, T. Kudo, In Situ Growth-Stress Measurement of Cr2O3 Scale Formed on Stainless Steels by Raman Spectroscopy, Materials science forum 522 (2006) 489–496. Trans Tech Publ.
[66] J. Mougin, N. Rosman, G. Lucazeau, A. Galerie, In situ Raman monitoring of chromium oxide scale growth for stress determination, Journal of Raman Spectroscopy 32 (9) (2001) 739–744.
[67] L. Martinelli, C. Desgranges, F. Rouillard, K. Ginestar, M. Tabarant, K. Rousseau, Comparative oxidation behaviour of Fe-9Cr steel in CO2 and H2O at 550 C: Detailed analysis of the inner oxide layer, Corros. Sci. 100 (2015) 253–266.
[68] S. Madloch, A. Dorcheh, M. Galetz, Effect of Pressure on Metal Dusting Initiation on Alloy 800H and Alloy 600 in CO-rich Syngas, Oxid. Met. 89 (3–4) (2018) 483–498.
[69] Y. Nishiyama, K. Kitamura, N. Otsuka, Metal dusting behaviour of Alloy800H in laboratory carbonaceous environments under high pressure, Materials Science Forum 595 (2008) 649–660. Trans Tech Publ.
[70] A.R.-V. Put, A. Fabas, S. Doublet, D. Monceau, Relevance of other parameters than carbon activity in defining the severity of a metal dusting environment, Oxid. Met. 87 (5–6) (2017) 655–666.
[71] K. Natesan, Z. Zeng, Development of materials resistant to metal dusting degradation, Argonne National Lab.(ANL), Argonne, IL (United States), 2007.
[72] A. Paul, K. Kaimal, M. Naik, S. Dharwadkar, Lattice and grain boundary diffusion of chromium in superalloy Incoloy-800, J. Nucl. Mater. 217 (1–2) (1994) 75–81.
[73] N. Parimin, E. Hamzah, A. Amrin, Effect of grain size on the isothermal oxidation of superalloys, Advances in Environmental Biology 7 (12) (2013) 3720–3726.
[74] M.G. Fontana, Corrosion engineering, (1986).
[75] K. Ralston, N. Birbilis, Effect of grain size on corrosion: a review, Corrosion 66 (7) (2010) pp. 075005-075005-13.
[76] S. Splinter, R. Rofagha, N. McIntyre, U. Erb, XPS characterization of the corrosion films formed on nanocrystalline Ni–P alloys in sulphuric acid, Surface and Interface Analysis: An International Journal devoted to the development and application of techniques for the analysis of surfaces, interfaces and thin films 24 (3) (1996) 181–186.

Supporting information

Effects of metal dusting relevant exposures of alloy 601 surfaces on carbon formation and oxide development

Xiaoyang Guo[a], Estelle Vanhaecke[a], Per Erik Vullum[b], Jianyu Ma[a], P. V. Daham S. Gunawardana[a, †], John C. Walmsley[b, ‡], De Chen[a], Hilde J. Venvik[a, *]

[a] *Department of Chemical Engineering, NTNU - Norwegian University of Science and Technology, Trondheim, 7491, Norway*

[b] *SINTEF Industry, Trondheim, 7465, Norway*

[†] *present address: Yara International ASA, Hydrovegen 67, 3936 Porsgrunn, Norway*

[‡] *present address Department of Materials Science and Metallurgy, University of Cambridge, 27 Charles Babbage Road, Cambridge CB3 0FS, United Kingdom*

**Corresponding author: hilde.j.venvik@ntnu.no*

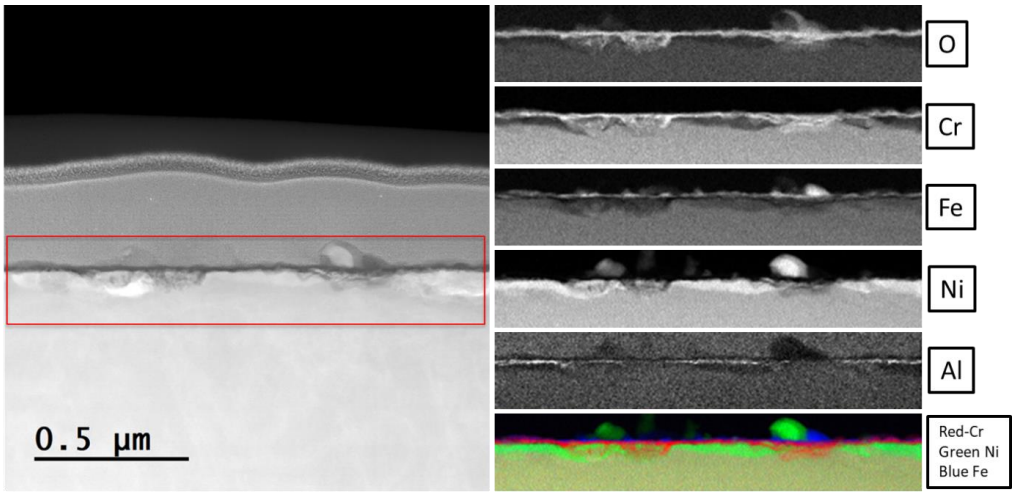

Figure S1, STEM image, EDS element mapping, and RGB element merge of the region selected from TEM lamella milled by FIB from Inconel 601 after exposure to 1 bar 10% steam in Ar at 540°C for 6 h. A thin protection layer of Pt was deposited on the alloy surface before ion milling that can be observed in the middle of the STEM image and as background in the Al map.

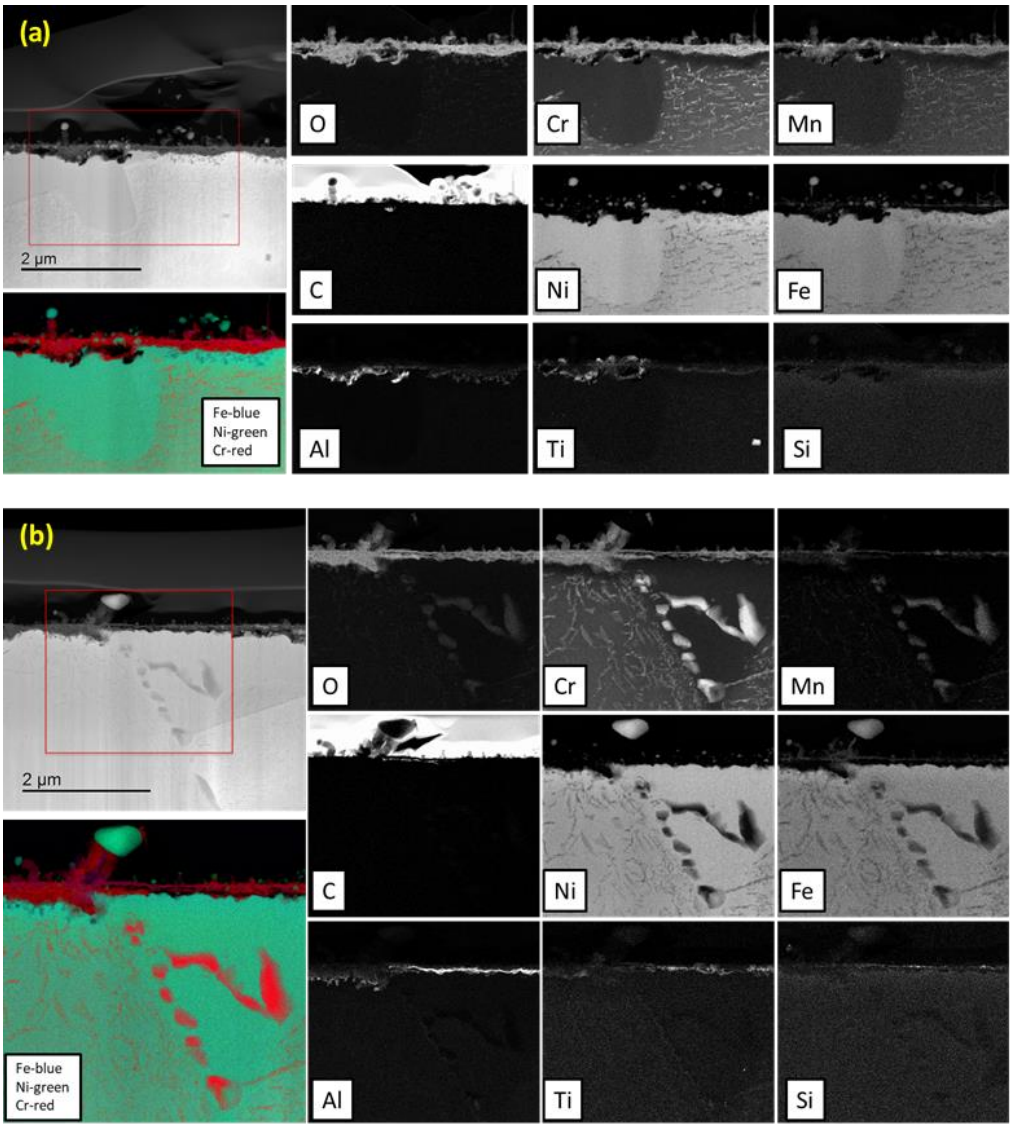

Figure S2, STEM images, EELS (C signal) and EDS (other signals) element mapping, and RGB element merge of selected regions of TEM lamella milled by FIB from oxidized Inconel 601 sample after exposure to infinite carbon activity (I- a_c) at 750˚C for 20h; (a) right region and (b) left region indicated by the red squares in Fig 9.

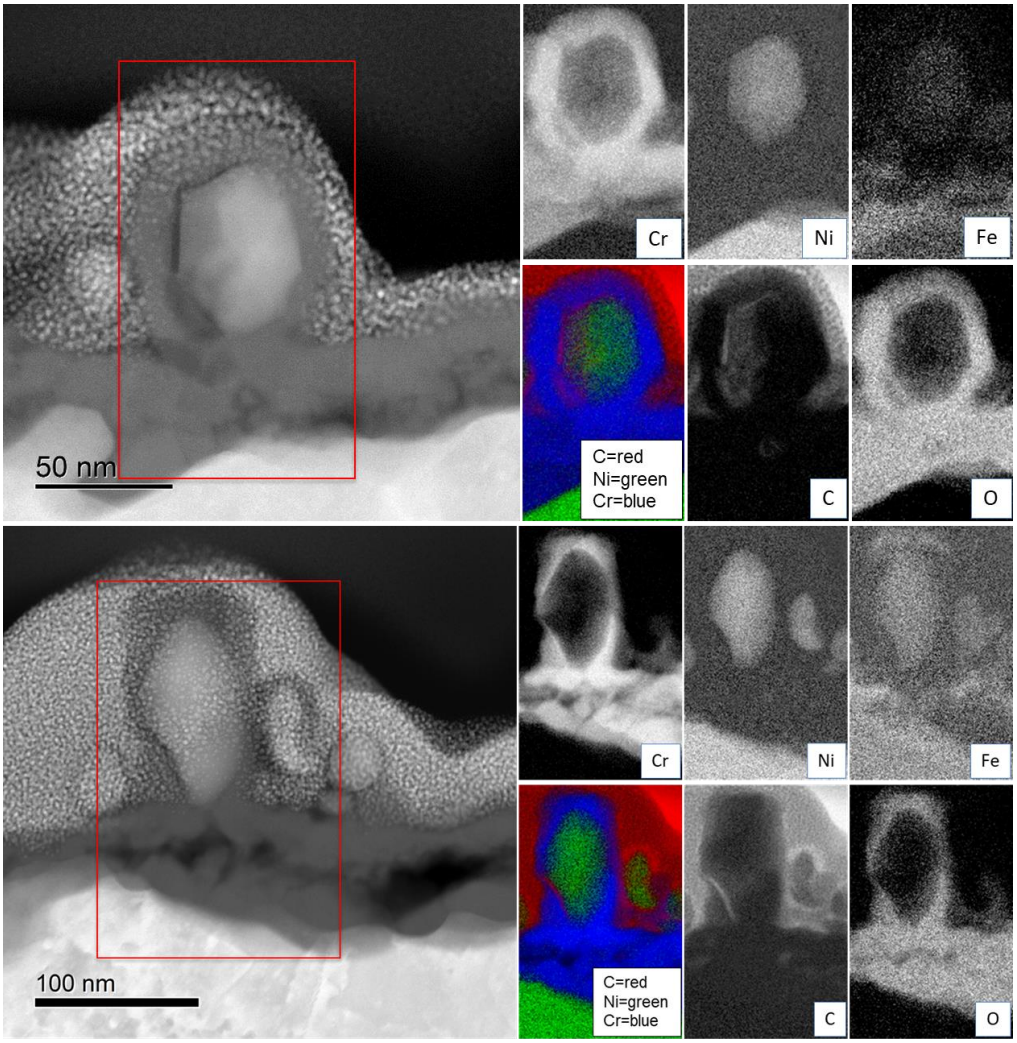

Figure S3, STEM images, EELS (C and O signals) and EDS (other signals) element mapping, and RGB element merge of selected regions of TEM lamella milled by FIB from oxidized Inconel 601 sample after exposure to finite low carbon activity (FL- a_c), at 750˚C for 2h. A thin protection layer of C was deposited on the alloy surface before ion milling and can be observed as background in the C map.

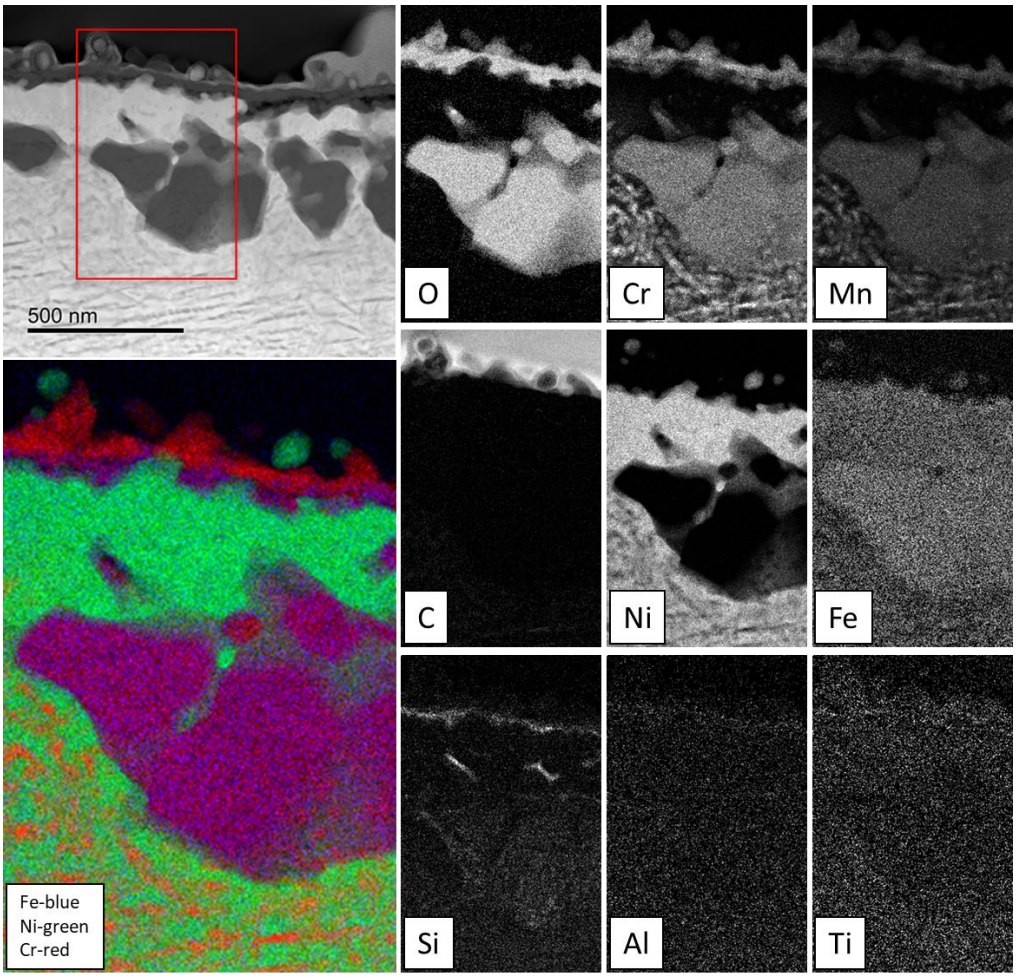

Figure S4, STEM images, EELS (C and Fe signals) and EDS (other signals) element mapping, and RGB element merge of selected regions of TEM lamella milled by FIB from oxidized Inconel 601 sample after exposure to finite low carbon activity (FL- a_c), at 750˚C for 2h. A thin protection layer of C was deposited on the alloy surface before ion milling and can be observed as background in the C map.

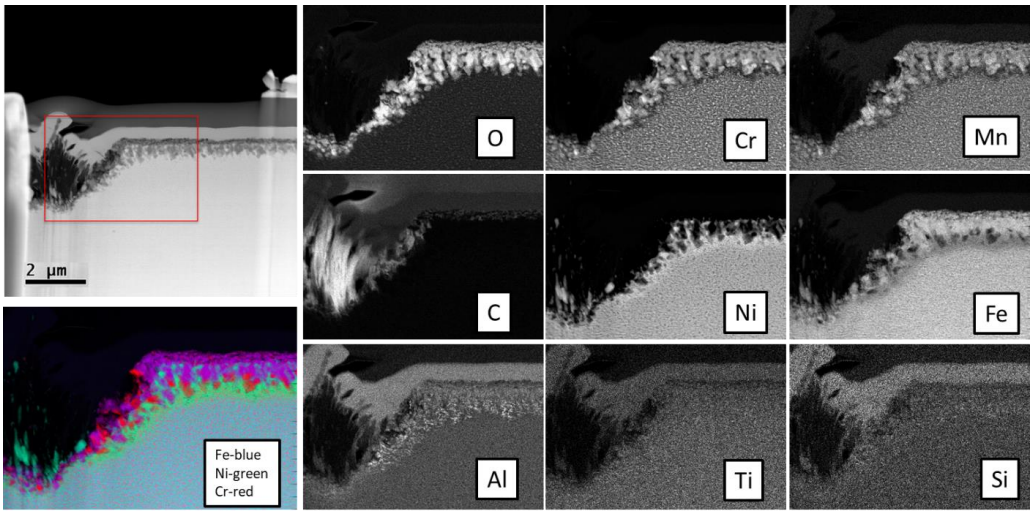

Figure S5, STEM image, EDS element mapping, and RGB element merge of the region selected from TEM lamella milled by FIB from oxidized Inconel 601 after exposure to simulated synthesis gas of finite low carbon activity (FL- a_c), at 750˚C for 20h and subsequently subjects to ultrasonic cleaning. A thin protection layer of Pt was deposited on the alloy surface before ion milling that can be observed in the upper left image and as background in the Al, Ti, and Si maps.

Paper II

Investigation of Metal Dusting Corrosion Process over UNS N08800 Alloy

Xiaoyang Guo, P. V. D. S. Gunawardana, De Chen, Estelle Vanhaecke, Hilde J. Venvik, John C. Walmsley

Paper III

Inhibition of Metal Dusting corrosion on Fe-based alloy by combined near surface severe plastic deformation and thermomechanical treatment

Xiaoyang Guo, Estelle Vanhaecke, Per Erik Vullum, John C. Walmsley,

De Chen and Hilde J. Venvik

Paper IV

Patent application: Method for reducing metal-dusting corrosion

Hilde J. Venvik and Xiaoyang Guo

ISBN 978-82-326-4772-9 (printed version)
ISBN 978-82-326-4773-6 (electronic version)
ISSN 1503-8181

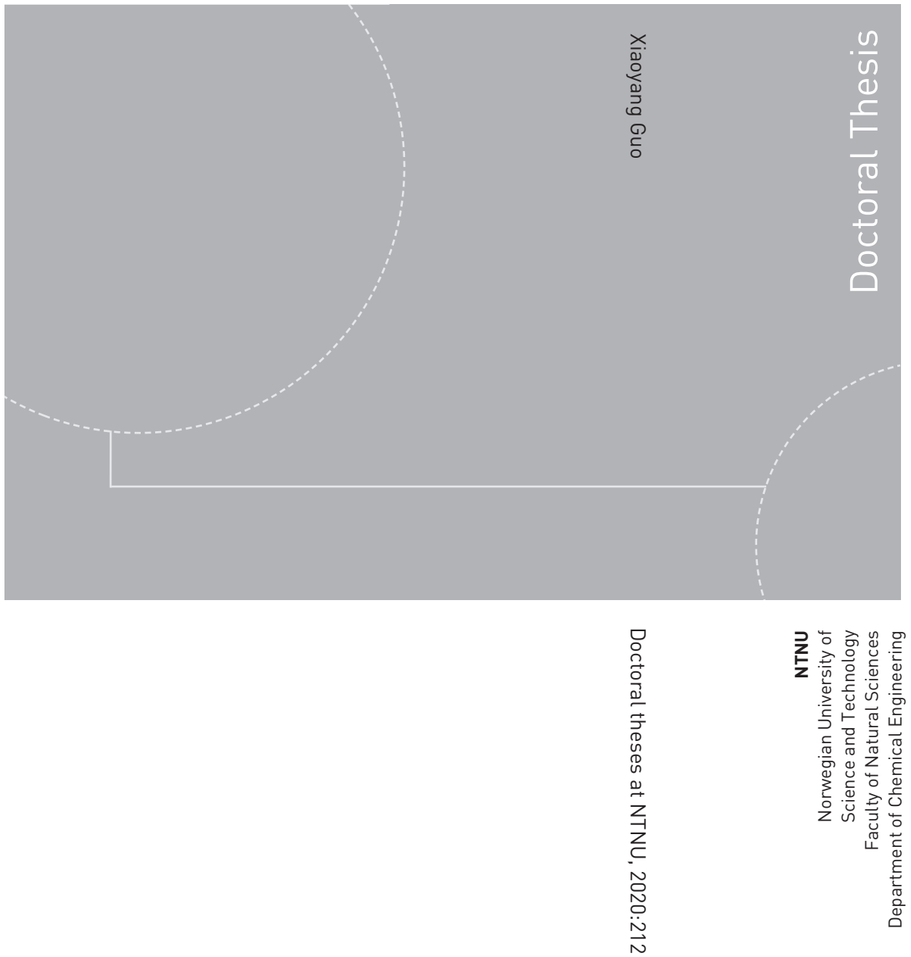

Doctoral theses at NTNU, 2020:212

Xiaoyang Guo

Inhibiting carbon growth at the initial stage of metal dusting corrosion of high temperature alloys

NTNU
Norwegian University of
Science and Technology
Faculty of Natural Sciences
Department of Chemical Engineering

NTNU
Norwegian University of
Science and Technology

Doctoral theses at NTNU, 2020:212

NTNU

NTNU
Norwegian University of
Science and Technology